



Title	Ethanol-Assisted Ironmaking using Mild-Dehydrated Goethite Ore
Author(s)	Kurniawan, Ade
Citation	北海道大学. 博士(工学) 甲第13637号
Issue Date	2019-03-25
DOI	10.14943/doctoral.k13637
Doc URL	http://hdl.handle.net/2115/76834
Type	theses (doctoral)
File Information	Ade_Kurniawan.pdf



[Instructions for use](#)

Ethanol-Assisted Ironmaking using Mild-Dehydrated Goethite Ore

(マイルドか焼したゲーサイト鉱石を用いるエタノール製鉄)

by Ade Kurniawan

A dissertation submitted as partial fulfillment of the requirement
for the degree of Doctor of Engineering (Graduate School of Engineering)

in Hokkaido University

2018

Doctoral Committee:

Professor Tomohiro Akiyama

Professor Naoyuki Hashimoto

Professor Seiichi Watanabe

Associate Professor Yoshiaki Kashiwaya

Associate Professor Takahiro Nomura

Abstract

The depletion of high-grade iron ore encourages us to utilize the low-grade ore (i.e., goethite) more effectively. On the other hand, the shortage of coal, as well as the mitigation of high CO_2 emission, need more intensive utilization of an alternative carbon source. Bioethanol as derived from biomass, regarded as a renewable and carbon-neutral resource, is a promising candidate as a reducing agent for ironmaking. Introducing ethanol to reduce iron ore through the chemical vapor infiltration (CVI) process is attractive as aiming for low-temperature reduction. This study describes the process intensification of the previous proposed CVI process. The new process has been proposed named as ethanol-assisted ironmaking.

Chapter two describes the several aspects to intensify in the previously-proposed CVI ironmaking. As reported in the study, there were three proposed processes involved in CVI ironmaking: (1) production of porous hematite ore, (2) production on carbon composite (CVI) ore through integrated pyrolysis-tar decomposition, and (3) reduction of the CVI ore. Vacuum dehydration successfully intensified the process 1 in reducing time on goethite dehydration to 1 h generating the similar porous hematite ore properties as in 24 h under atmospheric condition. On the other hand, the processes utilizing the inexpensive low-grade coal combined with renewable materials (i.e., biomass) or waste plastic (i.e., polyethylene) in process two are also investigated. It was concluded that the synergetic effect of combined coal-biomass or coal-PE improves the pyrolysis performance to increase decomposition reactivity of heavy tar. More heavy tar decomposed to light tar, gas, and deposited carbon in the ore. However, carbon contents from those methods were still not enough from the requirement for a perfect reduction process.

Chapter three describes the new ironmaking process called ethanol-assisted ironmaking. The porous hematite ore from mild-dehydrated goethite ore has been successfully reduced by charging ethanol (C_2H_5OH) under the heating conditions. In the experiments,

ethanol was dropwise added to the mild-dehydrated, porous iron ore beds at heating conditions using the temperature-program. As a result, the ethanol was soon decomposed to CO and H_2 , which then reduced the iron oxides. Porous iron ore acts as a suitable catalyst for ethanol decomposition as it simultaneously reduces to metallic iron. Interestingly, iron oxides were reduced at a lower temperature, compared to conventional coal-based ironmaking in the blast furnace. Metallic Fe was obtained at only 750 °C, showing a reduction degree of 81%, due to the contribution of hydrogen reduction. The longer charging time of ethanol promotes the higher reduction degree as well as sufficient compositions of reducing gas (H_2 - CO) for the reduction process. The results of experiments using different iron ores revealed the general rule that the higher CW content in ore makes the larger surface area of the iron ore by mild-dehydration, causing higher reactivity in the reduction process. The results appeared that mild-dehydrated iron ore is good raw materials of ethanol-assisted ironmaking, due to its nanopores. This process demonstrates an intensification of the previously-proposed CVI process from three-step become two-step processes by combining process 2 and 3.

Chapter four describes the kinetic analysis of simultaneous ethanol decomposition and iron reduction. The kinetic study is necessary for understanding the mechanism of the simultaneous ethanol decomposition – iron reduction process. There were 8 main reactions involved: (1) decomposition of ethanol, (2) decomposition of methane, (3) steam reforming of methane, (4) water gas shift, (5) Boudouard reaction, (6) direct reduction by C, (7) indirect reduction of iron oxide by CO, and (8) iron reduction by H_2 . Curve fitting methods were conducted with satisfying results (R_2 higher than 0.90) calculating 24 parameters consisting reaction rate constants, activation energies, and diffusion factors. Interpretation on the obtained parameters of the diffusion factors shows that the reaction of gases inside pore might be inhibited by carbon deposition on the pore surface of iron ore.

Chapter five describes the exergy analysis and presents a feasibility study on the proposed ethanol-assisted ironmaking process. Applying a high exergetic and renewable reducing agent like ethanol for ironmaking would be attractive in the thermodynamic point of view. There are four processes involved in the proposed ethanol-assisted ironmaking: (1) Porous ore production from goethite ore mild-dehydration, (2) Porous ore reduction by ethanol, (3) Hot metal – slag separation, and (4) Ethanol recovery. From the viewpoints above, ethanol-assisted ironmaking is an attractive method to solve problem-related resource, environment, and energy in future ironmaking industry.

Table of Contents

CHAPTER I GENERAL INTRODUCTION	7
1.1 Brief Overview of Modern Steelmaking	7
1.2 Ironmaking problems: resources, energy and environment.....	9
1.3 Recent innovative developments in ironmaking: CVI ironmaking	16
1.4 Toward the utilization of higher exergetic fuels for ironmaking: ethanol-assisted ironmaking	19
1.5 Scope of this study.....	24
References.....	25
CHAPTER II SEVERAL ASPECTS ON ENHANCING THE PREVIOUSLY PROPOSED CVI IRONMAKING PROCESS	29
2.1 Porous hematite ore production through vacuum dehydration.....	29
2.2 Integrated Pyrolysis–Tar Decomposition over Low-Grade Iron Ore for Ironmaking Applications: Effects of Coal–Biomass Fuel Blending.....	41
2.3 Integrated Pyrolysis-Tar Decomposition of Polyethylene-Coal Blends over Low-Grade Iron Ores	66
2.4 Conclusions	82
CHAPTER III REDUCTION BEHAVIOR OF POROUS HEMATITE ORE OVER ETHANOL DECOMPOSITION	85
3.1 Introduction	85
3.2 Materials and experimental methods.....	87
3.3 Result and discussions.....	92
3.4 Conclusions	106
References.....	107
CHAPTER IV KINETIC STUDY ON SIMULTANEOUS ETHANOL DECOMPOSITION AND IRON REDUCTION UNDER TEMPERATURE PROGRAMMED CONDITION.....	113
4.1 Introduction	113
4.2 Experimental Methods.....	115

4.3	Results and Discussions	122
4.4	Conclusions	130
	References.....	131

CHAPTER V SYSTEM EVALUATION OF ETHANOL-ASSISTED IRONMAKING:

EXERGY AND CO₂ EMISSION ANALYSIS..... 133

5.1	Introduction	133
5.2	Analysis method.....	137
5.3	Result and Discussions.....	141
5.4	Conclusions	154
	References.....	155

CHAPTER VI GENERAL CONCLUSIONS..... 159

APPENDIX..... 163

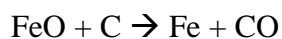
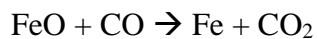
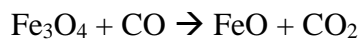
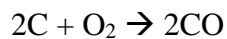
ACKNOWLEDGMENT..... 167

CHAPTER I

GENERAL INTRODUCTION

1.1. Brief Overview of Modern Steelmaking

Technological approaches in manufacturing steel have significantly evolved since industrial production began in the late 19th century [1]. In general, the modern steelmaking, are still based on the original Bessemer Process, involves six steps: Ironmaking, as the first step, involves the raw materials iron ore, coke, and lime being reacted and melted in a blast furnace. In the pretreatment step, the coke is prepared from coking coal by heating up the material in a limited oxygen atmosphere in the coke oven facility. Additionally, fine ore, limestone, and coke breeze are fed into the sinter plant or pelletizing facility to prepare sinter or pellet, respectively. Moreover, the coke, sinter/pellet, and limestone flux are sent to the top of a blast furnace to produce pig iron. By flowing heated air from the tuyere, several reactions occur inside as shown in Figure 1.1.1. The main ironmaking reaction of a blast furnace at a temperature about 500 - 1700 °C as mainly as follows:



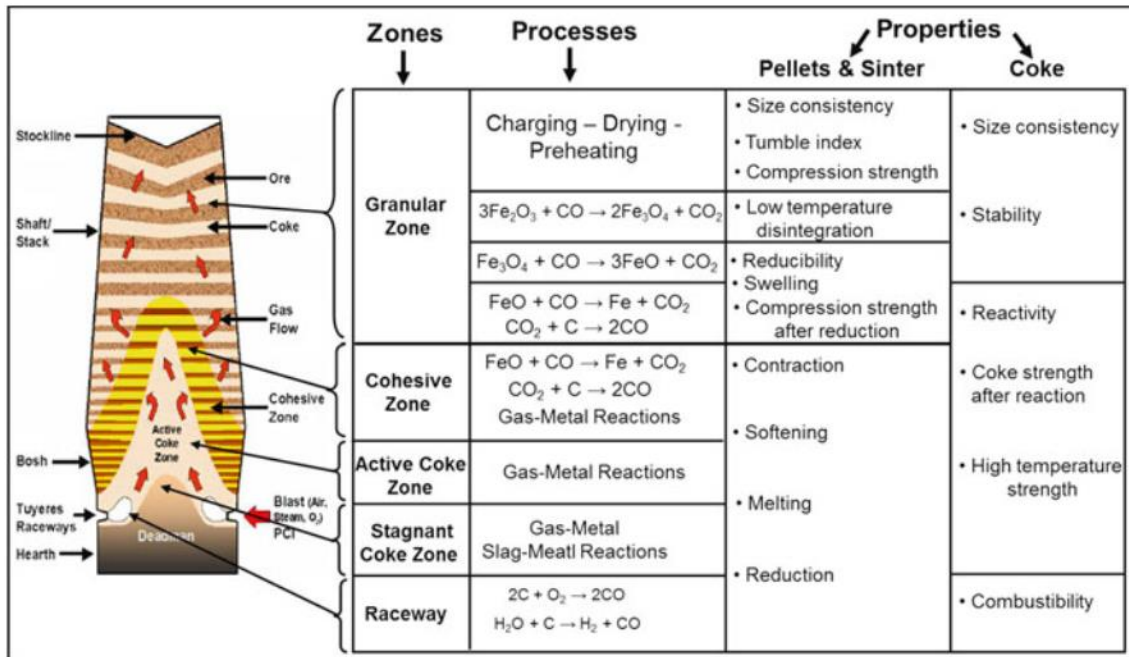


Figure 1.1.1 Reaction zone and inner state of a blast furnace as in [1].

During the iron reduction process, blast furnace emits the waste materials such as the blast furnace gas (BFG) containing mainly CO_2 and slag containing flux material. The resulting molten pig iron, also known as hot metal, still contains 4 - 4.5 mass% carbon and other impurities. The pig iron is then treated in the steelmaking process as a raw steel material.

The second step, primary steelmaking, is to convert pig iron to steel. However, the steel is produced not only from pig iron but also from recycled steel materials. All primary steelmaking, nowadays, are now divided into two primary methods: basic oxygen steelmaking (BOS) and the more modern one, EAF (Electric Arc Furnace). In BOS methods, pig iron and also additional recycled scrap steel are fed to the molten iron in a high-temperature converter. Oxygen is blown through the hot metal, which reduces the carbon content to 0 - 1.5 mass%. In contrast, in EAF methods, recycled steel scrap is fed through use high-power electric arcs with the temperatures up to 1650 °C to melt the

metal and convert it into high-quality steel. Recently, the production sharing of BOS and EAF routes are 70% and 30%, respectively [2].

The third step, secondary steelmaking involves treating the molten steel produced from both BOS and EAF routes to adjust the composition in steel product. This step is performed by adding or removing certain elements and/or manipulating the temperature and production environment. Next, the fourth step, continuous casting sees the molten steel cast into a cooled mold causing a thin steel shell to solidify, then withdrawn as the shell strand. The strand is then cut into desired lengths depending on application; slabs for flat products (plate and strip), blooms for sections (beams), billets for long products (wires), or thin strips. Continuing to the fifth step, the primary forming, the cast steel is then formed into various shapes, usually by hot rolling, a process that eliminates cast defects and achieves the required shape and surface quality. Hot rolled products are divided into flat products, long products, seamless tubes, and specialty products. The final step, the manufacturing, fabrication, and finishing, known as the secondary forming techniques, give the steel its final shape and properties, which are including shaping (cold rolling), machining (drilling), joining (welding), coating (galvanizing), heat treatment (tempering), surface treatment (carburizing).

1.2. Ironmaking problems: resources, energy, and environment

Steel consumption is one indicator of wealth and industrialization as depicted in Figure 1.2.1. Figure 1.2.2 shows a comparison of steel production and consumption between steel exporting country (i.e., Japan) and steel importing country (i.e., Indonesia). World crude steel production in 2017 reached 1,691 million tons. By 2050, steel consumption is projected to increase by 1.5 times that of present levels, to encounter the requirements of the growing population [3]. The iron and steel production are highly

reliant on the non-renewable raw material and fossil fuel as an energy source. By high worldwide demand for iron and steel material in the close future, the iron and steel industries face serious problems related to the resources, energy, and environment.

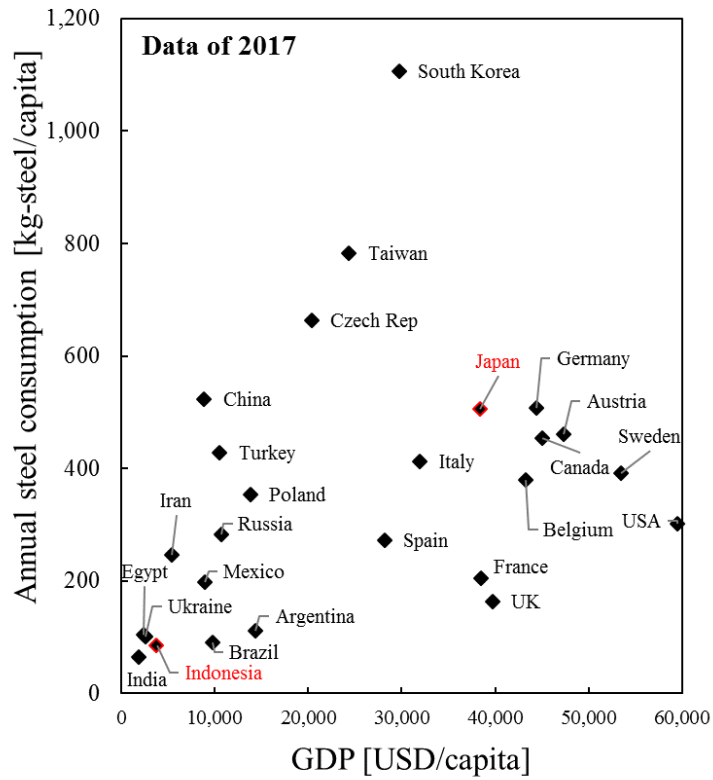


Figure 1.2.1 Steel consumption versus gross domestic product per capita of different countries [3].

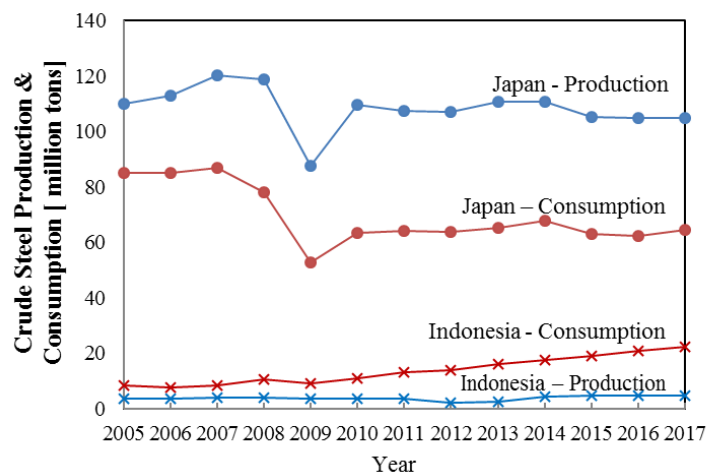


Figure 1.2.2 Crude steel production and consumption between steel exporting country (i.e., Japan) and steel importing country (i.e., Indonesia) [3]

1.2.1. Depletion of high-grade iron ore and coal

For producing 1 ton of pig iron, the typical ironmaking industry requires 350 kg of coking coal, 100 kg of pulverized coal, 1390 kg of high-grade ore and 120 kg of limestone [4]. The high amount of required iron ore makes the ironmaking process highly depends on the iron ore grade. By definition iron ore grade relies on its Fe-content which is usually found as magnetite (Fe_3O_4 , 72.4% mass-Fe), hematite (Fe_2O_3 , 69.9% mass-Fe), goethite ($\text{FeO}(\text{OH})$, 62.9% mass-Fe), limonite ($\text{FeO}(\text{OH}) \cdot n(\text{H}_2\text{O})$, 55% mass-Fe) or siderite (FeCO_3 , 48.2% mass- Fe) [5]. Figure 1.2.3 shows the transition of the average global produced iron ore grade is decreasing year by year [3]. The recent fall in world ore grade is due to the large consumption of low-grade Chinese ores [6]. This is mean that the high-grade ore resources are now becoming limited. This trend is then followed by the increasing price of high-grade ore containing total Fe more than 60% mass of from 15 USD/ton in 2003 to 70 USD/ton in 2018[3].

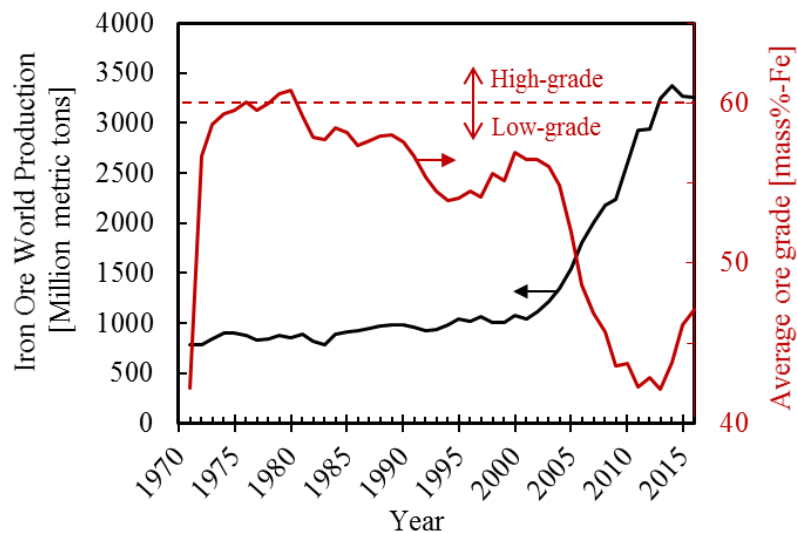


Figure 1.2.3 The trend of the iron ore world production and average iron ore grade [3]

Figure 1.2.4 shows the current reserves of iron ore in the global production that indicates most of the iron ore producing countries rely on lower Fe content ore. When

low-grade iron ores with the high content of combined water (CW) such as goethite ore are fed to a sinter machine or blast furnace, a large amount of energy is required to dehydrate the ore producing hematite or magnetite. Moreover, charging the goethite directly into a blast furnace is also not an option due to the removal of its CW forming the goethite become a porous-brittle ore, causing the permeability problem in the blast furnace [7]. Therefore, the innovative method should be considered to deal with goethite ore as ironmaking raw material.

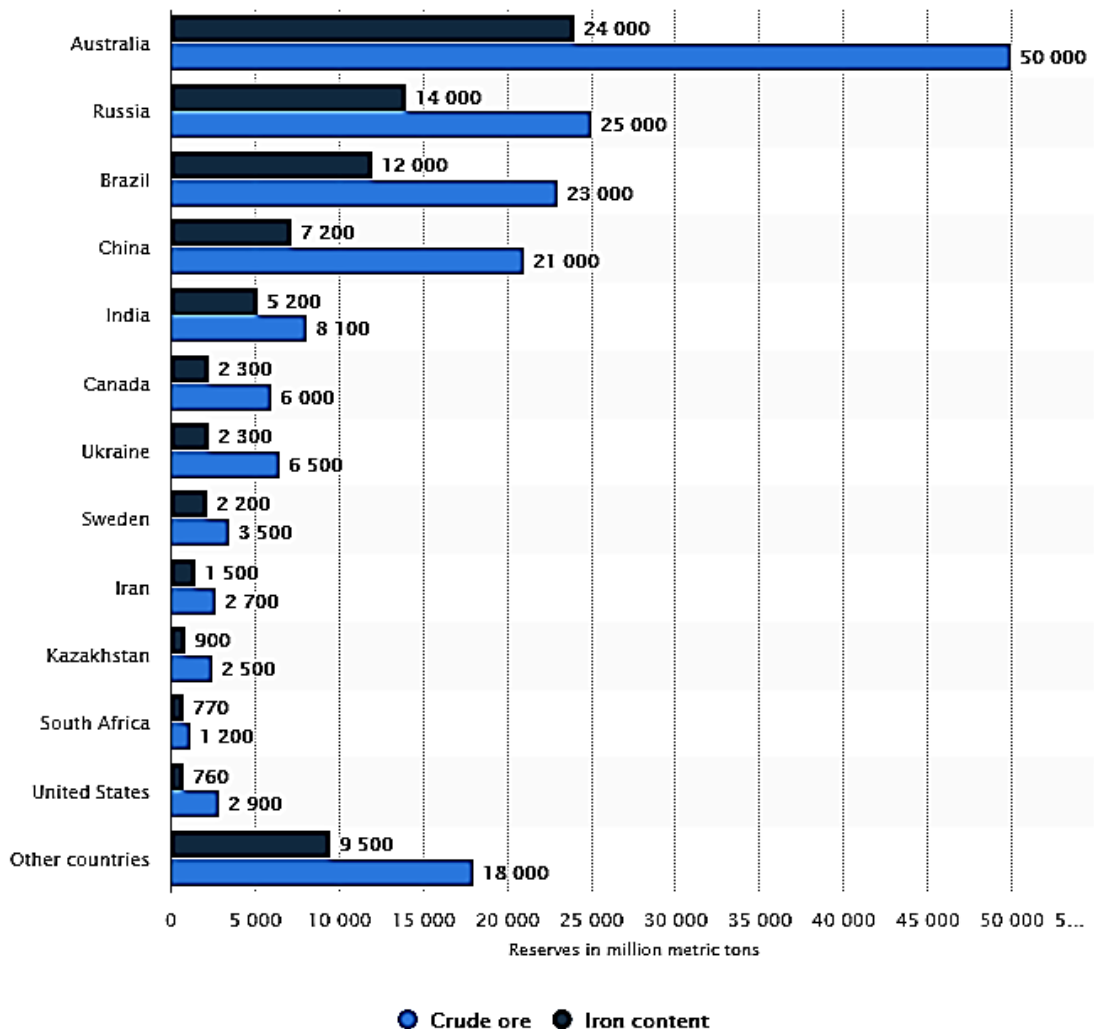


Figure 1.2.4 Global reserves of iron ore as of 2017, by country (in a million metric tons) [3]

Figure 1.2.5 shows reserves to the production of various coals in the world. The higher ratio meant a large amount of availability and is limited in utilization. Apparently, the high-grade coal (HGC) has a lower ratio compared to low-grade coal for both sub-bituminous and lignite. Therefore, the utilization of low-grade coal (LGC) should be more encouraged. However, the trend of coal reserves seems to decrease, in other words, in the future, coal both high-grade and low-grade will also be depleted. In addition, British Petroleum reported that as of 1035 billion tons of coal proven reserved divided by 7.7 billion ton/year of coal production, the coal-based industries would be only 133 year remains on relying on coal (assuming business as usual). Thus, the utilization of alternative fuel like biomass or waste materials for industry, especially ironmaking should be strongly considered.

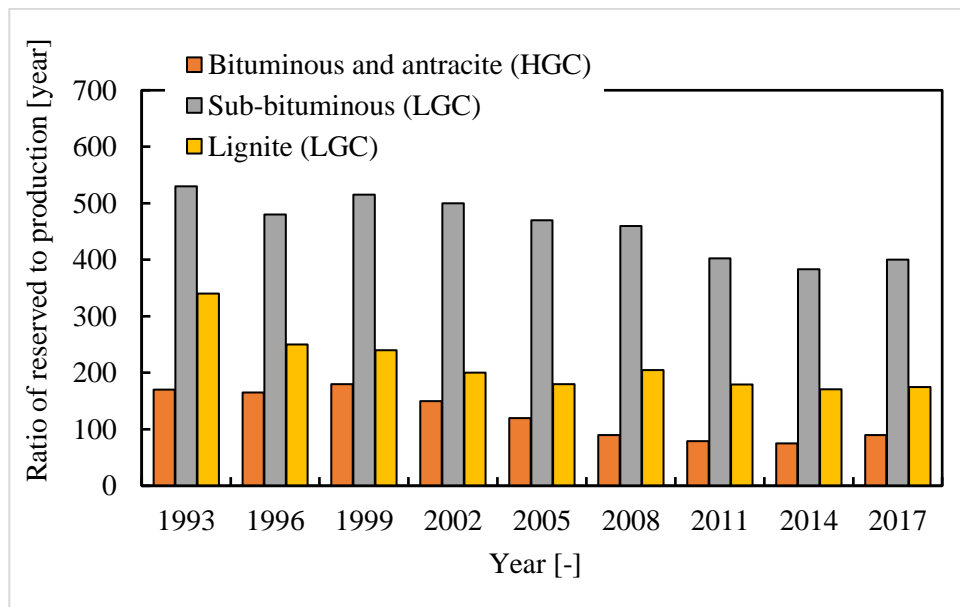


Figure 1.2.5 Ratio of reserves to the production of high-grade coal and low-grade coal[8]

Therefore, the effective utilization of low-grade ores such as goethite (FeOOH) and low-grade coal or even alternative fuel in the modern ironmaking industry is highly attractive to solve problems related to the depletion of high-grade iron ores and coal.

1.2.2. High CO₂ emission in ironmaking

Approximately 15% of total carbon dioxide emitted in Japan is accounted for the iron and steel industry, in which the emissions from ironmaking process take about 70% of that amount [9]. Consequently, the ironmaking process should be an essential role in CO₂ mitigation. Figure 1.2.6 shows the boundary conditions (boundary) differentiating the ironmaking process and the downstream processes and the material flow in the ironmaking process [10]. The ironmaking process centers on the blast furnace, which produces molten pig iron, and also includes the sintering machine, which produces sintered ore as a raw material for the blast furnace, coke ovens that produce coke, which is essential as a reducing agent, and hot stoves that generate the high temperature (approx. 1200°C) hot blast blown into the blast furnace. Large amounts of CO₂ are generated by the reduction reaction ($\text{Fe}_2\text{O}_3 + 3\text{CO} \rightarrow 2\text{Fe} + 3\text{CO}_2$) in the blast furnace and the combustion reaction ($\text{C} + \text{O}_2 \rightarrow \text{CO}_2$, $\text{C}_n\text{H}_m + (n+m/4)\text{O}_2 \rightarrow n\text{CO}_2 + (m/2)\text{H}_2\text{O}$) of carbonaceous materials (coke breeze, etc.) and carbon-containing gases (blast furnace gas (B gas) and coke oven gas (C gas)) in the sintering machine, coke ovens, and hot stoves.

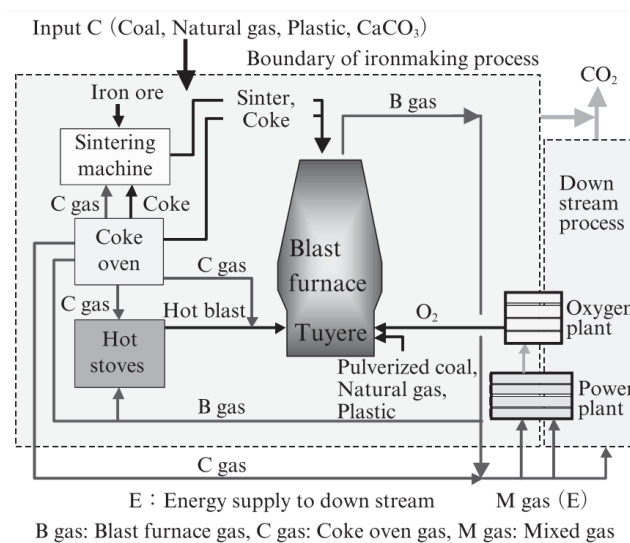


Figure 1.2.6 Schematic diagram of material flow in the ironmaking process and the boundary of ironmaking [10]

Because the conventional integrated iron and steel mill process uses a considerable amount of carbon in the form of coal as a reducing agent and is energy intensive, the CO₂ emissions are significant [11]. Figure 1.2.7 shows the CO₂ emission from ironmaking in which 27% of total CO₂ emission from industrial sector compared to others. The direct CO₂ emissions from the iron and steel industries represent about 7% of the global total of 32.5 gigatons-CO₂.

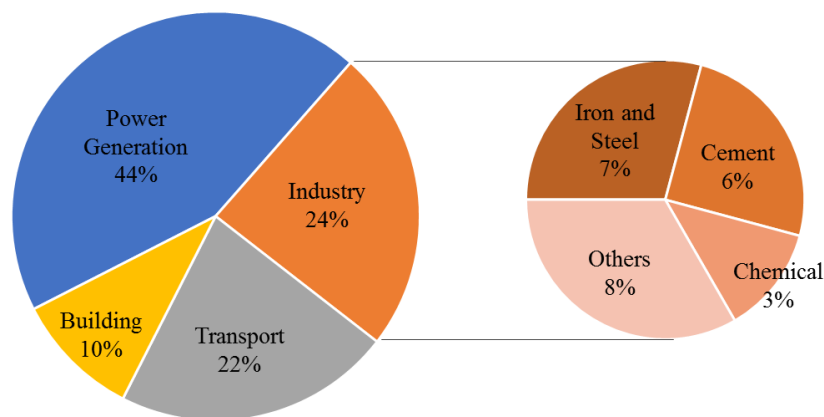


Figure 1.2.7 Total global CO₂ footprint of the different sector (data: direct CO₂ emissions sources 2014 (IEA)) showing iron and steel emits 7% of total global. [12]

1.2.3. High energy consumption

The iron and steelmaking industry is one of the most energy-intensive industries in the world and consumes 19.5 EJ/year, which constitutes around 5% of the total global energy consumption [12]. The energy required in the production of steel depends on the process used, and it constitutes from 20% to 40%, a significant portion, of the cost of steel production. Thus, improvements in energy efficiency are necessary to reduce production costs and thereby improve competitiveness [13].

1.3. Recent innovative developments in ironmaking: CVI ironmaking

The iron- and steelmaking is the most significant energy consuming in the industrial sectors. The high energy consumption is associated with the emission of CO₂ and other pollutants. The most common ironmaking process used in the world is the blast furnace which contributes around 70 % of the world's steel production. Recently, the blast furnace has undergone significant modifications and improvements to reduce energy consumption and CO₂ emissions. The modifications are being focused on two main approaches: (1) development of top charging materials and (2) injections of auxiliary fuels through blast furnace tuyeres. The enhancement of burden material quality and its charging mode into the blast furnace has resulted in a smooth and efficient operation. Recently, the usage of nut coke in the modern blast furnace is accompanied by higher production and lower reducing agent rates. Efficient recycling of in-plant fines by its conversion into briquettes with proper mechanical strength is applied in some blast furnaces to exploit the iron- and carbon-rich residues. Nowadays, novel composite agglomerates consist of iron ores and alternative carbonaceous materials represent a new trend for low-carbon blast furnace with lower dependence on the conventional burden materials. The recent investigations demonstrated that the novel composites could reduce the thermal reserve zone temperature in the blast furnace and consequently enhance the carbon utilization through its higher reactivity compared to fossil fuels. The top charging of bio-reducers and hydrogen-rich materials into the blast furnace is one of the remarkable innovations to mitigate the CO₂ emissions. Although some of the previous approaches are recently applied in the modern blast furnace, others are still under intensive discussions to enhance its implementations [14].

An innovative process in ironmaking namely chemical vapor infiltration (CVI) ironmaking was initially developed in 2009 by Hata et al. [15] and has begun to be sophisticated by Cahyono et al. [16]. Figure 2.1.1 present the current development in CVI ironmaking of goethite-based iron ore mentioning the proposed three-step process. The process one is the dehydration of goethite (FeOOH) based ore. Goethite has become attractive for its porous properties after its dehydration. The dehydration of goethite at 300-500 °C with a heating rate of 3°C/min under air atmosphere creates micro- and mesopores ranging from 2 to 4 nm in size and a BET specific surface area as high as 70-100 m² g⁻¹ [17]. Saito et al. optimized the dehydration temperature of goethite to control its pore morphology, suggesting that heating up to 300 °C with a heating rate of 3 °C/min and holding for 24 h are the optimum heating conditions for porous iron ore production [18].

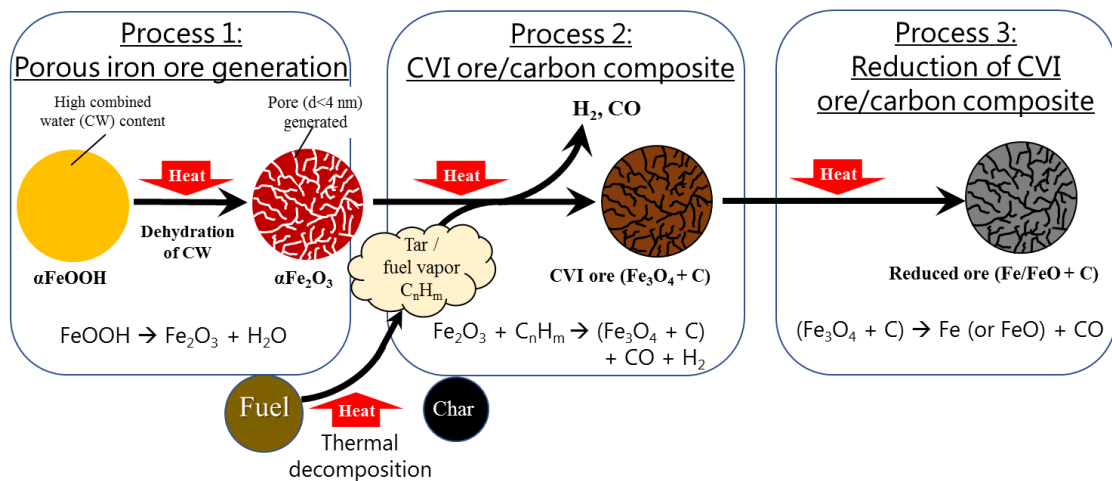


Figure 1.3.1 Process scheme of CVI ironmaking of goethite-based ore

Process two is called the integrated pyrolysis–tar decomposition process. This process aims to reduce tar generated from solid fuel by decomposing it as deposited carbon over porous iron ore, as well as using chemical vapor infiltration (CVI) to produce carbonized ore [15]. The carbon, from the decomposition of biomass tar, is deposited

within the iron ore pores. Carbon tar filled the nanocracks and increased carbon content, which could be used as a potential reduction agent. In addition, indirect iron ore reduction by CO and H₂ converting Fe₂O₃ to Fe₃O₄, simultaneously occur during tar decomposition. Therefore, the method offers benefits such as removal of tar and production of pre-reduced ores containing deposited carbon namely CVI ore. Several investigations have been performed on the carbon deposition of various solid fuels, including high-grade bituminous coal, low-grade lignite coal, and biomass palm kernel shells. However, a new challenge was introduced: to produce a CVI ore with a higher carbon content as reduction agent as well as increasing performance on the prereduction step.

Process 3 is the reduction of the carbonized (CVI) ore produced in process 2. CVI ore shows high reactivity during the reduction reaction that started at 750°C primarily and is a significantly lower temperature than the mixture of reagent magnetite and metallurgical coke [19]. It was confirmed that this high reactivity was due to the nanoscale contact between carbon and the ore and the less fused and less cross-linked nature of the biotar-derived carbon. Another interesting approach found for process 3 is by introducing the ironmaking through combustion synthesis [20]. A thick-layered-carbon-infiltrated goethite ore was obtained by the tar impregnation method, and it was partially reduced to metallic iron in an oxygen atmosphere regardless of short time (less than 1 min) process. The experiment revealed that high temperature was generated due to the carbon combustion at the ore surface under an oxygen atmosphere, which appears to have led to the direct reduction reaction ($\text{FeO}_x + \text{C} \rightarrow \text{FeO}_{x-1} + \text{CO}$) inside the ore. Moreover, the nanocontacts between iron ore and carbon successfully made the reduction faster.

1.4. Toward the utilization of higher exergetic fuels for ironmaking: ethanol-assisted ironmaking

1.4.1. The alternative reducing agent for ironmaking

One of the most important benefits that could be realized upon charging carbon composites into BF is the possibility and flexibility of top charging hydrogen-rich and bio-carbonaceous materials. The cost reduction, as well as GHG emission, is much affected by coke led to increased effort to reduce the coke consumption rate in the blast furnace operation. Around 1.5 tons of CO₂ is emitted on each ton of produced hot metal [21]. The total worldwide CO₂ emission associated with blast furnace ironmaking in 2014–2015 is about 1733 million tons which mainly comes from the use of fossil fuel [22].

An approach is to find an alternative reducing agent related to its chemical exergy density. In thermodynamics, the exergy, a property of all materials and energy flow, depends on its states such as chemical composition, temperature, and pressure relative to the external environment. The exergy defines the maximum of useful energy output of the system. Exergy of the material consists of two types: the physical (thermomechanical) and chemical exergy. The physical exergy is depending on its physical state: mixture compositions, temperature, and pressure. While the chemical exergy is obtained when the considered system is brought into reaction with reference substances present in the environment [23]. The higher contents of O and Cl would result in smaller chemical exergy, while higher contents of H and C would lead to larger chemical exergy. The higher chemical exergy content of material can be interpreted as having a higher reactivity on the reduction process.

Table 1.4.1 shows the standard chemical exergy of some materials as ironmaking fuel. The higher-exergetic fuel for ironmaking is more attractive to be utilized. H₂ is the best ironmaking fuel in this viewpoint of chemical exergy. Lower temperature reduction can be reached if we apply hydrogen in ironmaking. However, the strong endothermic reaction requiring the higher external heat source might not make this process become attractive.

Table 1.4.1 Standard Chemical Exergy, ϵ^0 (T = 298.15 K, p = 101.325 kPa), of some materials as ironmaking reducing agent.

Substance (phase)	Name	MW [kg/kmol]	H-density and {C-density}		Standard chemical exergy, ϵ^0	
			[mole%]	[mass%]	[MJ/kmol]	[MJ/kg]
H _{2(g)}	Hydrogen	2	100 {0}	100 {0}	236.1	118.1
CH _{4(g)}	Methane	16	80 {20}	25 {75}	831.2	52.0
C _(s) (graphite)	Coke, Graphite	12	0 {100}	0 {100}	409.9	34.2
C ₂ H ₅ OH _(l)	Ethanol	46	66.7 {22.2}	13 {52.2}	1356.9	29.5
NH _{3(g)}	Ammonia	17	75 {0}	17.6 {0}	337.9	19.9
C ₃ H ₈ O _{3(l)}	Glycerin	92	57.1 {21.4}	8.7 {39.1}	1762.6	19.2
C ₆ H ₁₂ O _{6(s)}	Sugar (Glucose)	180	50 {25}	6.7 {40}	3091.6	17.2
CO(NH ₂) _{2(s)}	Urea	60	80 {12.5}	6.7 {20}	688.6	11.5
CO _(g)	Carbon Monoxide	28	0 {50}	0 {42.8}	274.7	9.8

Recently, methane and coke are still feasible reducing agents in ironmaking. However, the limitation of its resources like natural gas and coal as non-renewable fossil fuels will be an obstacle of the future ironmaking. A simple way to resolve energy concerns is to use biomass resources in the ironmaking industry. Biomass is a recent term related to any organic materials that may contain useful fuel compounds. Examples of biomass materials are wood pulp waste associated with paper manufacture, agricultural waste such as grasses and crop byproducts like corn stalks, and known as municipal solid waste (MSW) in the industry. These biomass sources can be decomposed biologically by

various microbes to produce usable fuel, while at the same time offering new ways of using materials that were previously discarded into our environment, often with harmful effects.

In the viewpoint of exergy, biomass fuel selection need to consider its H/C ratio as well as its O content. For an instant, sugar ($C_6H_{12}O_6$), however, simply to be produced, its chemical exergy content is not so attractively high compared to other material for ironmaking fuel. When sugar then converted to ethanol (C_2H_5OH) through the fermentation process. In Table 1.4.1, ethanol was placed as among the high exergetic fuel for ironmaking. The ethanol then becomes attractive as ironmaking fuel [24]. Attribute to its decomposition producing H_2 , CO , and C , ethanol might be more superior to minimize the exergy loses within the ironmaking process. Therefore, as one of the hydrogen carrier, ethanol is a promising fuel candidate to initiate combined carbon-hydrogen-based ironmaking.

1.4.2. Possibility ethanol as ironmaking fuel candidate

Many research programs recently focus on the development of concepts such as renewable resources, sustainable development, green energy, as well as eco-friendly process, for energy supply. Increasing the use of biofuels for energy generation purposes is of particular interest nowadays because they allow mitigation of greenhouse gases, provide means of energy independence. Bio-ethanol is a fuel derived from biomass sources of feedstock; typically plants such as wheat, sugar beet, corn, straw, and wood. Bio-ethanol is currently made by large-scale yeast fermentation of sugars that are extracted or prepared from crops followed by separation of the bio-ethanol by distillation. One major problem with bio-ethanol production is the availability of raw materials for production. The availability of feedstocks for bio-ethanol can vary considerably from

season to season and depend on geographic locations. The price of the raw materials is also highly volatile, which can profoundly affect the production costs of the bioethanol [27]. Figure 1.4.1 shows yearly global ethanol production by country/region showing the global production of bio-ethanol increased from 40 million tons in 2007 to over 70 million tons in 2016. With all of the new government programs in America, Asia, and Europe in place, total global fuel bio-ethanol demand could grow to exceed 100 million tons by 2020. However, the current production of ethanol is only concerned to accommodate the transportation fuel in which ethanol is used primarily in the gasoline blending. There is no available ethanol for ironmaking fuel yet. Therefore, a new business should be considered in utilizing ethanol for ironmaking reducing agent.

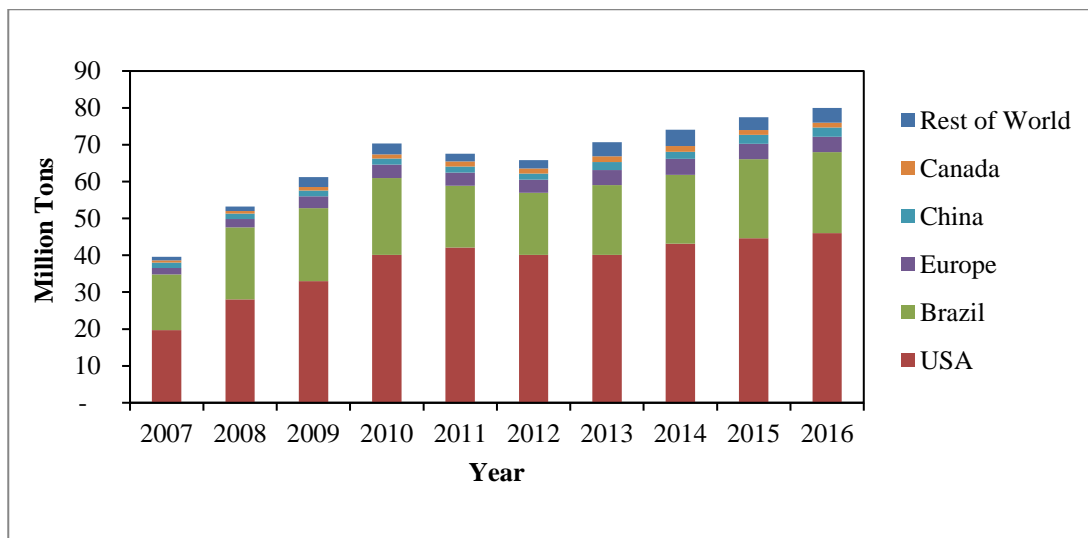


Figure 1.4.1 Global ethanol production by country/region dan year [25]

Recently, bioethanol production from lignocellulose holds excellent potential due to the widespread availability, abundance, and relatively low cost of cellulosic materials. There are still several hindrances on the way of developing an economically feasible technology, due to the complicated structure and inhomogeneous nature of the raw material. The economic and environmentally-friendly development of bioethanol from lignocellulose necessitates highly efficient process integration. Considerable successes

on pretreatment, enzymatic hydrolysis, fermentation, and distillation of ethanol have been achieved over the past few decades. Many new ideas, such as biorefinery and the concept of oriented conversion of classified composition, have been proposed and practiced in many ethanol plants using lignocellulose as raw materials. By an intelligent combination of pretreatment, hydrolysis, fermentation and product separation, the maximum efficacy and benefit of the process can be achieved due to the simultaneous production of many high-value co-products with ethanol from agricultural residues. Although the cost of ethanol from straw is still higher than ethanol from grains, further decrease in the cost of enzymes and efficient combination of other technologies will result in competitive bioethanol production from straw [26].

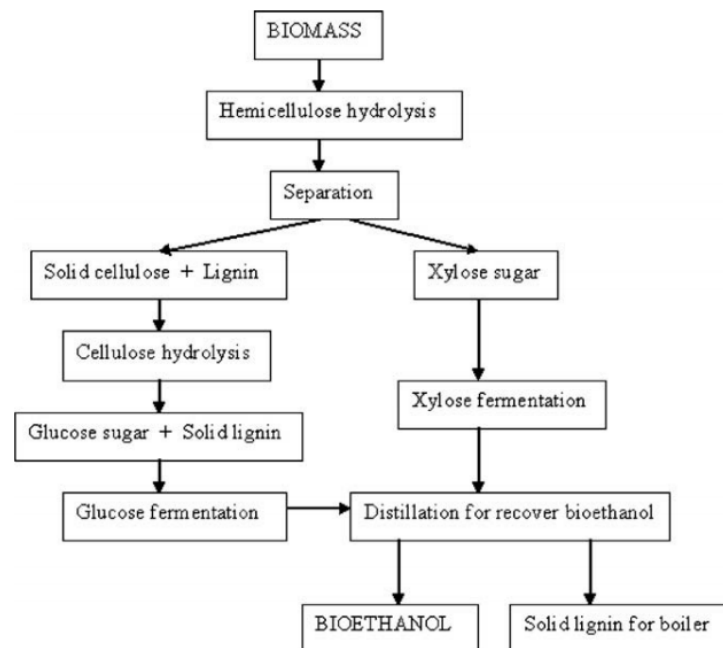


Figure 1.4.2 Bio-ethanol production scheme from lignocellulosic biomass material [27].

Figure 1.4.3 shows the current situation of ethanol production methods. The future ethanol production will be no longer depend on the conventional sugar fermentation only. A novel method: the syngas fermentation, that is developed by

Lanzatech [28], will be one of the possible solutions to ensure ethanol security for ironmaking purposes. Using gas fermentation, producing ethanol from waste gas is also possible to mitigate the carbon emissions from the steel industry and even other industries without adversely impacting food or land security. From this point of view, ethanol-assisted ironmaking becomes one attractive solution to be considered for future ironmaking.

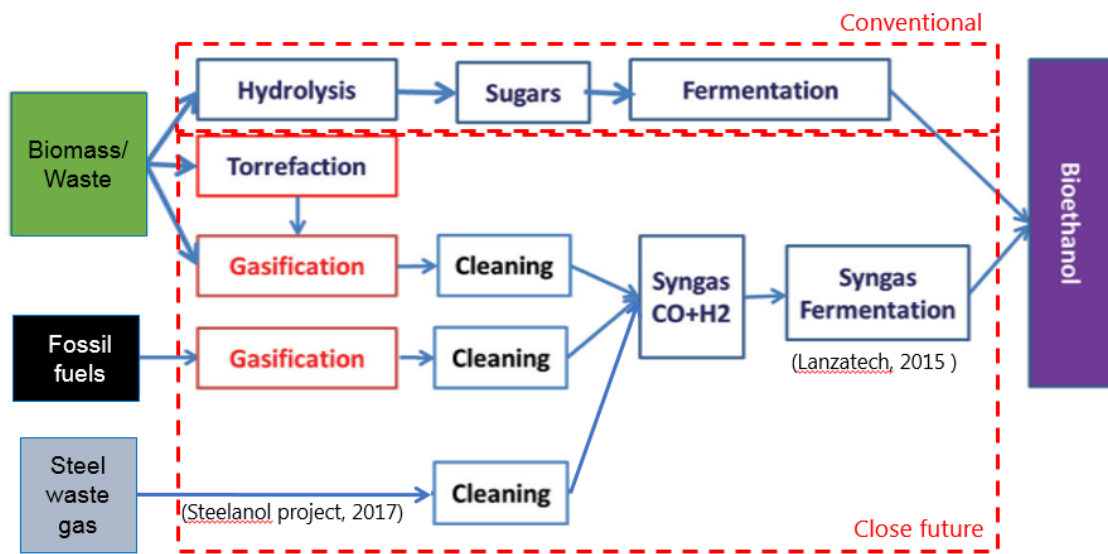


Figure 1.4.3 Current situation of ethanol production methods.

1.5. The scope of this study

Introducing ethanol-assisted ironmaking is one process intensification in CVI ironmaking. Therefore, this thesis would comprehensively examine the step and characterize the product. In addition, the total evaluation of the proposed system is studied by exergy analysis. The content of this thesis is divided into six chapters as follow:

Chapter 1 presents the general introduction of this study.

Chapter 2 describes several aspects related to ironmaking through simultaneous fuel decomposition- porous iron reduction, including an enhance in the dehydration

process of goethite ore through vacuum dehydration, as well as the effect of different fuels and its blending in CVI ironmaking process.

Chapter 3 describes the fundamental phenomena of ethanol-assisted ironmaking. The reduction behavior of a porous hematite ore (as mild-dehydrated goethite) during ethanol decomposition is the focus on this chapter.

Chapter 4 describes the kinetic study of simultaneous ethanol decomposition – iron reduction was evaluated for understanding the processing mechanism.

Chapter 5 describes the exergy analysis and CO₂ emission for the proposed process system of ethanol-assisted ironmaking, including the comparison with the conventional blast furnace.

Chapter 6 summarizes the results of this thesis as a general conclusion.

References

- [1] Ranade, M.G. and Chaubal, P.C., 2004. An intensive course—blast furnace ironmaking. McMaster University, Hamilton, pp.9-1.
- [2] Carpenter, A., 2012. CO₂ abatement in the iron and steel industry. IEA Clean Coal Centre, pp.67-70.
- [3] World Steel Association, 2018, Fact Sheet, https://www.worldsteel.org/en/dam/jcr:f07b864c-908e-4229-9f92-669f1c3abf4c/fact_energy_2018_.pdf. accessed on November 21st 2018.
- [4] Kurniawan, A., Abe, K., Nomura, T. and Akiyama, T., 2017. Integrated Pyrolysis–Tar Decomposition over Low-Grade Iron Ore for Ironmaking Applications: Effects of Coal–Biomass Fuel Blending. *Energy & Fuels*, 32(1), pp.396-405.
- [5] Taylor, W.E.G., 2005. SEDIMENTARY ROCKS. Ironstones.
- [6] Mudd, G.M., 2013. The limits to growth and ‘finite’ mineral resources: re-visiting the assumptions and drinking from that half-capacity glass. *International Journal of Sustainable Development* 4, 16(3-4), pp.204-220.

- [7] Magalhaes, M.S., Brandao, P.R.G. and Tavares, R.P., 2007. Types of goethite from Quadrilátero Ferrífero's iron ores and their implications in the sintering process. *Mineral Processing and Extractive Metallurgy*, 116(1), pp.54-64.
- [8] World energy council. *Survey of energy resources*. London (1993-2008)
- [9] Center for Global Environmental Research. National Institute for Environmental Studies, Japan. *National Greenhouse Gas Inventory Report of Japan*. 2012-04.
- [10] Sato, M., Yamamoto, T., and Sakurai, M., 2014. Recent progress in ironmaking technology for CO₂ mitigation at JFE Steel. *JFE Technical Report*, 19
- [11] Ho, M.T., Bustamante, A. and Wiley, D.E., 2013. Comparison of CO₂ capture economics for iron and steel mills. *International Journal of Greenhouse Gas Control*, 19, pp.145-159.
- [12] International Energy Agency, 2018, <https://www.iea.org/Sankey/index.html#?c=World&s=Final%20consumption>
- [13] He, K. and Wang, L., 2017. A review of energy use and energy-efficient technologies for the iron and steel industry. *Renewable and Sustainable Energy Reviews*, 70, pp.1022-1039.
- [14] Ahmed, H.M., Mousa, E.A., Larsson, M. and Viswanathan, N.N., 2016. Recent Trends in Ironmaking Blast Furnace Technology to Mitigate CO₂ Emissions: Top Charging Materials. In *Ironmaking and Steelmaking Processes* (pp. 101-124). Springer, Cham.
- [15] Hata, Y., Purwanto, H., Hosokai, S., Hayashi, J.I., Kashiwaya, Y. and Akiyama, T., 2009. Biotar ironmaking using wooden biomass and nanoporous iron ore. *Energy & Fuels*, 23(2), pp.1128-1131.
- [16] Cahyono, R.B., Yasuda, N., Nomura, T. and Akiyama, T., 2015. Utilization of low grade iron ore (FeOOH) and biomass through integrated pyrolysis-tar decomposition (CVI Process) in ironmaking industry: Exergy analysis and its application. *ISIJ International*, 55(2), pp.428-435.
- [17] Kashiwaya, Y. and Akiyama, T., 2010. Nanocrack formation in hematite through the dehydration of goethite and the carbon infiltration from biotar. *Journal of Nanomaterials*, 2010, p.18.

- [18] Saito, G., Nomura, T., Sakaguchi, N. and Akiyama, T., 2016. Optimization of the Dehydration Temperature of Goethite to Control Pore Morphology. *ISIJ International*, 56(9), pp.1598-1605.
- [19] Hosokai, S., Matsui, K., Okinaka, N., Ohno, K.I., Shimizu, M. and Akiyama, T., 2012. Kinetic study on the reduction reaction of biomass-tar-infiltrated iron ore. *Energy & Fuels*, 26(12), pp.7274-7279.
- [20] Abe, K., Kurniawan, A., Ohashi, K., Nomura, T. and Akiyama, T., 2018. Ultrafast Iron-Making Method: Carbon Combustion Synthesis from Carbon-Infiltrated Goethite Ore. *ACS Omega*, 3(6), pp.6151-6157.
- [21] Ng, K.W., Giroux, L., MacPhee, T. and Todoschuk, T., 2012. Combustibility of charcoal for direct injection in blast furnace ironmaking. *Iron and Steel Technology*, 9(3), p.70.
- [22] (www.worldsteel.org)
- [23] Müller, A., Kranzl, L., Tuominen, P., Boelman, E., Molinari, M. and Entrop, A.G., 2011. Estimating exergy prices for energy carriers in heating systems: Country analyses of exergy substitution with capital expenditures. *Energy and buildings*, 43(12), pp.3609-3617.
- [24] Kurniawan, A., Abe, K., Ohashi, K., Nomura, T. and Akiyama, T., 2018. Reduction of mild-dehydrated, low-grade iron ore by ethanol. *Fuel Processing Technology*, 178, pp.156-165.
- [25] <http://www.ethanolrfa.org/wp-content/uploads/2017/02/Ethanol-Industry-Outlook-2017.pdf>
- [26] Chen, H. and Qiu, W., 2010. Key technologies for bioethanol production from lignocellulose. *Biotechnology Advances*, 28(5), pp.556-562.
- [27] Balat, M. and Balat, H., 2009. Recent trends in global production and utilization of bio-ethanol fuel. *Applied energy*, 86(11), pp.2273-2282.
- [28] (www.lanzatech.com/worlds-first-commercial-waste-gas-ethanol-plant-starts/) accessed on 21 July 2018.

CHAPTER II

SEVERAL ASPECTS ON ENHANCING THE PREVIOUSLY PROPOSED CVI IRONMAKING PROCESS

This chapter discusses several aspects related to ironmaking through simultaneous fuel decomposition-iron reduction to enhance those three processes of Chemical Vapor Infiltration (CVI) ironmaking as describe in Sub-chapter 1.3. This chapter consists of three subchapters: subchapter 2.1 describes an intensification in the proposed dehydration process of goethite ore. Subchapter 2.2 and 2.3 describe the effect of different fuel and its blending in the CVI process such as coal-biomass, and coal-polyethylene, respectively.

2.1. Porous hematite ore production through vacuum dehydration

2.1.1. Introduction

Goethite (FeOOH)-based ore has become attractive to be utilized in ironmaking [1]. As mildly dehydrated to remove its high combined water (CW), it changes to a nanoporous hematite ore [2]. The nanopore is a crucial role in providing a nanocontact between iron oxide and reducing agents such as C, CO, or H₂, promoting a significant increase in its reduction reactivity[3,4,5]. When the goethite was dehydrated at 200–250 °C, slit-like pores with a width less than 2 nm were formed along the [010] direction. Slit-like pores changed to spherical micropores (300–500 °C) and eventually disappeared (600–800 °C). Compared to the synthetic goethite, natural goethite has a lower crystallinity and smaller primary particle size of under 100 nm. The natural goethite before dehydration contained 4 nm pores as cracks that remained even after heating to

800°C. In the case of natural goethite, the optimum dehydration temperature for higher surface area and pore volume was 350°C, which was higher than that of 250°C for the synthetic goethite [6].

However, the long dehydration time of goethite ore is still one problem⁴. This study investigated the effect of vacuum condition on the mild-dehydration of goethite-based ore reducing the dehydration time as one of the process intensifications for CVI ironmaking.

2.1.2. Experimental Methods

2.1.2.1. Materials

FeOOH reagent, Goethite A (GA) ore, and Goethite B (GB) ore with the CW contents of 10, 9, and 7 wt.%, respectively, were used in this study. The total Fe-content of those samples were 63, 59, and 57 wt.%, respectively. Table 2.2.1 shows the material used in this study. Vacuum dehydration was carried out using a degassing apparatus (Quantachrome). The sample of 0.3 g was put into a quartz bulb cell equipped with a rotary high vacuum pump (the ultimate system pressure of 1.7 Pa). It was then heated by a controlled electric heater to the temperature of 100, 200, and 300 °C; heating rate of 10 °C min⁻¹, and hold for 30 min – 3 h. BET surface areas, pore volumes, and pore size distributions of the samples were measured on the N₂ adsorption technique (Autosorb-6, Quantachrome).

Table 2.1.1 Iron oxides and iron ores used as raw materials in this study.

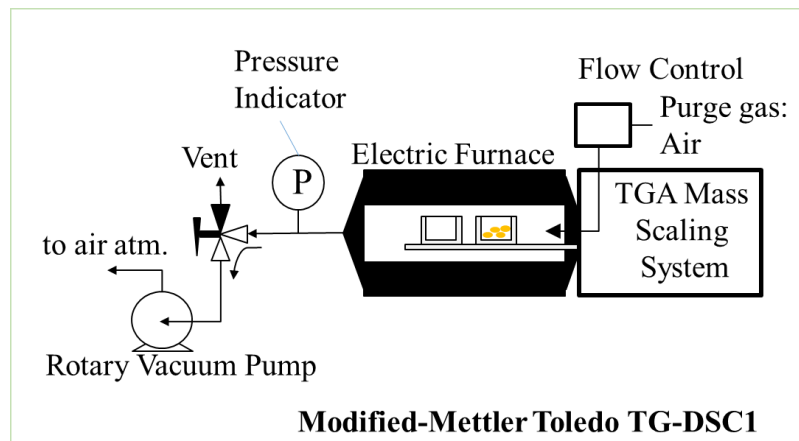
Ore name	Code	CW [wt%]	T.Fe [wt%]	FeO [wt%]	SiO ₂ [wt%]	Al ₂ O ₃ [wt%]
α -FeOOH reagent	FeOOH	10.1	62.9	-	-	-
Australian Ore A	GA	8.6	58.6	n/a	4.5	1.6
Australian Ore B	GB	7.2	57.4	0.1	5.4	2.6

2.1.2.2. Vacuum dehydration

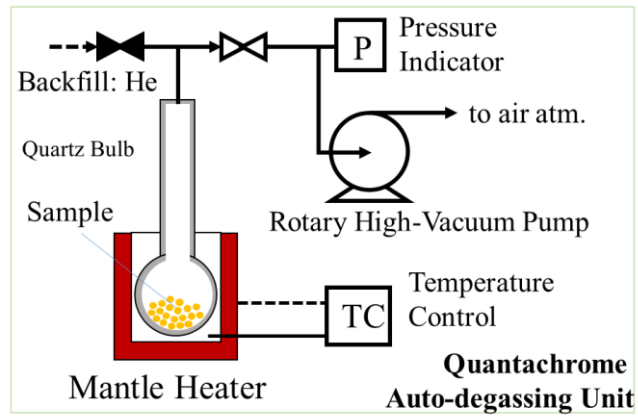
Figure 2.2.1(a) shows the mild vacuum condition was carried out in thermogravimetry (TG) apparatus modified by connecting it with a rotary vacuum pump at its heater chamber exhaust line. This configuration had the ultimate pressure of 3.7×10^3 Pa. The sample was placed in the 150ug alumina crucible heated with an electric furnace. Figure 2.2.1(b) shows the high vacuum dehydration using with the ultimate vacuum pressure of 1.7 Pa. The apparatus was set from a modification of the Quantachrome Auto-degassing apparatus. The sample was put into a quartz bulb cell, then heated with an electrically controlled mantle heater. The heating rate is set to 10 K min^{-1} up to $300 \text{ }^\circ\text{C}$. The cell was assembled with the pressure and temperature indicator allowing us to conduct an in-situ pressure-temperature during dehydration experiment. The samples after dehydration were soon analyzed using gas adsorption technique to obtain the BET surface area, total pore volume, and pore size distribution.

Ultra-high vacuum dehydration was also conducted in this study. The changes in the sample morphologies at elevated temperature from room temperature up to $500 \text{ }^\circ\text{C}$ were observed using in-situ transmission electron microscopy (TEM) JEM-ARM1300 (JEOL) during heating. The heating rate was manually set at $10 \text{ }^\circ\text{C min}^{-1}$ and then hold for 10 min at specific temperatures for observation.

The summary of the experimental conditions at three different vacuum pressures are shown in Table 2.2.2.



(a)



(b)

Figure 2.1.1 Apparatus setting for (a) mild-dehydration and (b) high-vacuum-dehydration experiments.

Table 2.1.2 Parameter of different experimental conditions in vacuum dehydration.

Parameter	Experiments		
	Mild-vacuum	High-vacuum	Ultra-high-vacuum
Dehydration conditions	Mild-vacuum	High-vacuum	Ultra-high-vacuum
Ultimate system pressure [Pa]	3.7×10^3	1.7	5.6×10^{-6}
Experiment types	Vacuum-TG	In-situ Pressure-Temperature Monitor	In-situ TEM under heating
Sample types	FeOOH reagent	FeOOH, GA & GB ores	FeOOH, GA ore
Sample mass [mg]	50	250	
Sample size	1 μm – FeOOH; 1-2 mm - ores	1 μm – FeOOH; 1-2 mm - ores	200 nm – FeOOH and GA ore
Temp [°C]	RT to 300	RT to 300	RT to 500
Heating rate [K/min]	1 μm – FeOOH; 1-2 mm - ores	1 μm – FeOOH; 1-2 mm - ores	200 nm – FeOOH and GA ore
Holding time	2 h	1 h	10 min
Obtained data	TG, DTG	In-situ P-T, Pore characterization	In-situ TEM images

2.1.3. Result & Discussions

2.1.3.1. Thermogravimetric behavior of FeOOH reagent under mild-vacuum dehydration

Figure 1 shows the comparison between the thermogravimetric profiles of FeOOH reagent during dehydration under atmospheric and mild-vacuum conditions. There are two peaks detected from FeOOH decomposition. Under different conditions, FeOOH dehydration temperature shift from 295.4 °C (at atmospheric - air 100 ml/min) to 281.1 °C (mild-vacuum – no air flow).

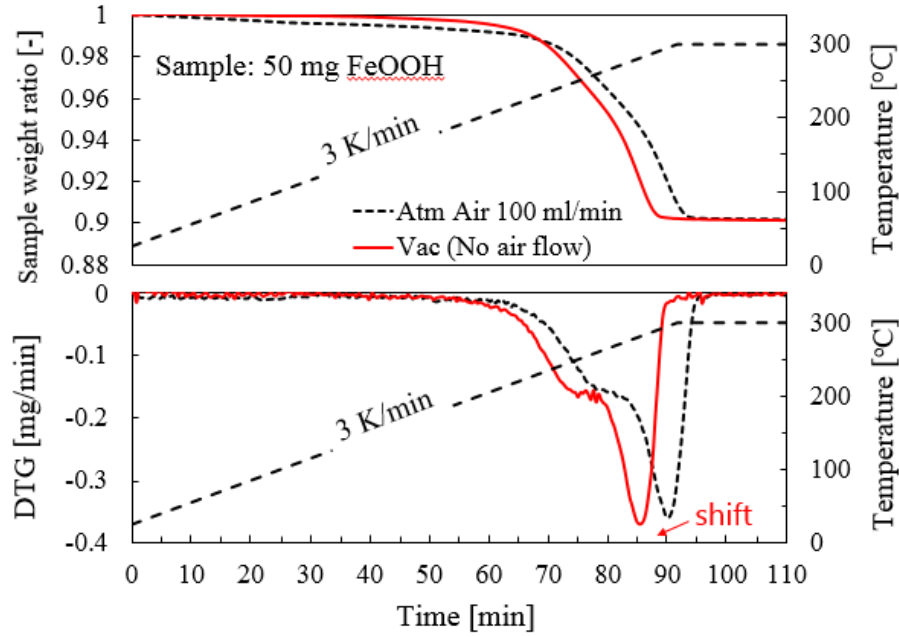


Figure 2.1.2 TG profiles of FeOOH reagent during dehydration under atmospheric and vacuum conditions (-72.5 kPag).

2.1.3.2. Dehydration behavior on high vacuum

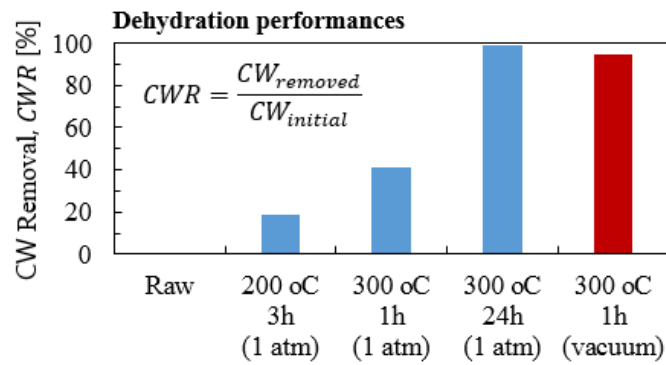
Figure 2.1.3 shows the comparison of the dehydration behavior between high-vacuum and atmospheric dehydration process of FeOOH reagent. The dehydration performance at Figure 2.1.3(a) means the removal of the combined water (CW) from the FeOOH sample after dehydration, which is calculated using the following equation

$$CWR = \frac{CW_{removed}}{CW_{initial}} \times 100\% \quad (2.1-1)$$

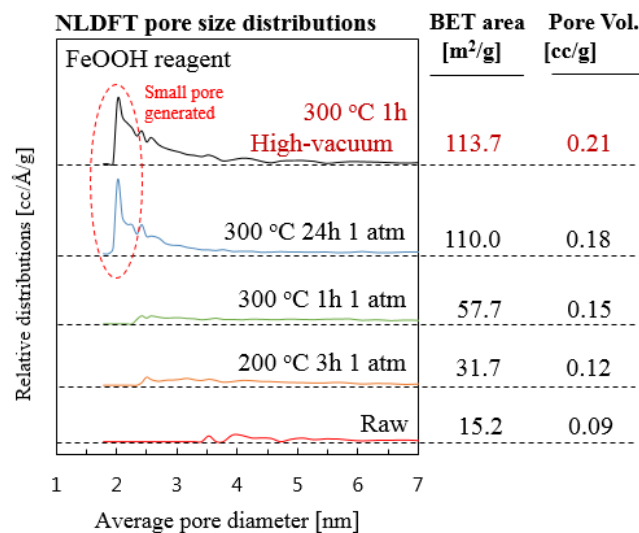
$$CWR = \frac{(W_{s0} - W_{s1})}{0.101 W_{s0} X_{FeOOH}} \times 100\% \quad (2.1-2)$$

Where W_{s0} denotes the mass of FeOOH sample before dehydration [g]. W_{s1} is the mass of FeOOH sample after dehydration [g]. The factor of 0.101 is the mass fraction of the combined water at raw FeOOH reagent [-]. X_{FeOOH} is the mass fraction of FeOOH content in the sample. In the case of goethite reagent, X_{FeOOH} is set to be 1. However, the data of FeOOH content in case of iron ore might be difficult to find. Therefore, this

equation is simply applicable for FeOOH reagent only. The results of different dehydration conditions were also compared with the previous study on FeOOH dehydration under an atmospheric condition in [6], in which the dehydration under air condition at the temperature of 300 °C, a heating rate of 10 °C min, and holding time of 24 h. Interestingly, the mild-dehydration of 1 h under high-vacuum condition (P = 1.7 Pa) removes 95 mass% of CW. It has a similar result with 24 h at atmospheric one. Under vacuum condition, porous hematite can be produce faster significantly.



(a)



(b)

Figure 2.1.3 Comparison of (a) dehydration performance and (b) pore properties between high-vacuum and atmospheric dehydration process of FeOOH reagent atmospheric conditions.

The BET surface area, pore volume, and pore size distribution of the FeOOH reagent samples after vacuum dehydration were observed (Figure 2.2.2(b)). The NLDFIT pore size distribution shows that the pore size of 2 - 4 nm is generated within 1 h at 300 °C, then shifted to a larger pore size after a more extended time. The high-vacuum condition might not affect the main dehydration temperature because the significant CW removal still occurs at 300 °C. Vacuum dehydration only promotes a faster CW removal from oxide structure which is proceeded within 30 min after 300 °C reached (in case of FeOOH reagent).

Figure 2.1.4 shows the *in-situ* pressure-temperature profiles of FeOOH reagent, GA ore, and GB ore during mild-dehydration at 300 °C under vacuum condition. All three samples show the pressure increase when the temperature increases from 100 to 300 °C, which is mean that the goethite dehydration, releasing water vapor, occurs rapidly in this range temperatures. The pressure increases due to water vapor generation during heating. When the temperature was held at 300 °C, the pressure drops back to its original state due to the dehydration start to finish. Interestingly, under the high-vacuum condition, within 1 h at 300 °C, the dehydration seems to be finished.

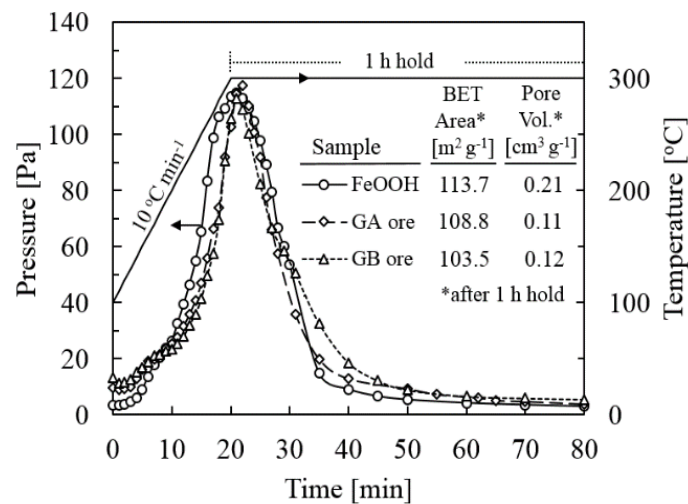


Figure 2.1.4 In-situ pressure-temperature profiles on high-vacuum dehydration of FeOOH reagent and ores.

Theoretically, 1 molecule of goethite decomposes to a molecule of hematite and a molecule of water ($\text{FeOOH} \rightarrow \text{Fe}_2\text{O}_3 + \text{H}_2\text{O}_{(\text{g})}$). This decomposition reaction is spontaneously started at 83 °C as its thermodynamic properties. The decomposition of goethite apparently consists of two steps process. The first is the solid decomposition of FeOOH to Fe₂O₃ and adsorbed water ($2\text{FeOOH} \rightarrow \text{Fe}_2\text{O}_3 + \text{H}_2\text{O}_{(\text{ads})}$). This reaction is very quick. Second, soon after adsorbed water was formed, it will diffuse out as water vapor ($\text{H}_2\text{O}_{(\text{ads})} \rightarrow \text{H}_2\text{O}_{(\text{g})}$) leaving the porous Fe₂O₃ structure. The second step is a kind of mass transport phenomena of the combined water which its properties generally increases with temperature. That is why it needs the higher temperature to increase the overall rate process in the actual goethite dehydration process. Furthermore, the diffusion, or in general, the overall mass transfer of combined water is driven by the difference between the concentration of water inside pore and in the bulk gas phase outside of pore. Vacuuming condition can increase the driving force (e.g., the water concentration), resulting in an enhance the overall performance of the goethite dehydration process.

Figure 2.1.5 shows the comparison between the pore properties of iron oxide and ores from high-vacuum dehydration at 300 °C. The NLDFT pore size distribution shows the nanopores of 2 nm-pore sized are generated in FeOOH reagents within 30 min under vacuum condition. It then shifted to a larger pore size after a more extended time. This is also related to The BET surface area and total pore volume of FeOOH reagent which is at 30 min higher than at 1 h. Meanwhile, in case of GA and GB ores, after vacuum dehydration, the BET surface area and total pore volume are less than the FeOOH reagent. This is related to CW content in the ores, which are less than the FeOOH reagent. However, it looks like longer time is needed to generate nanopore in ores.

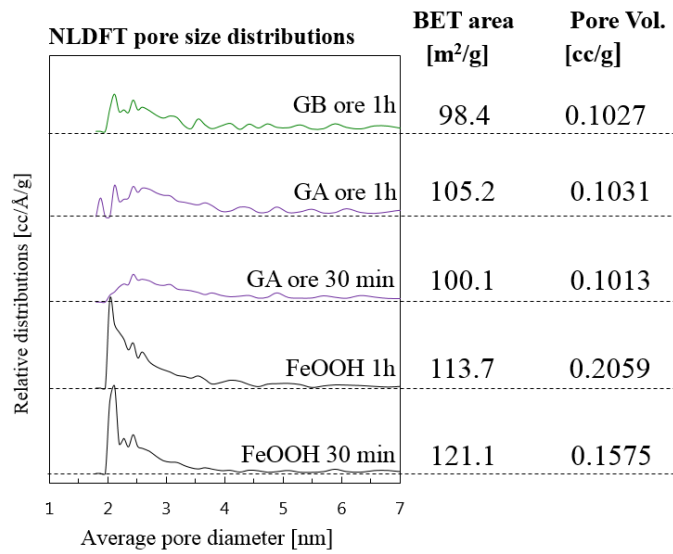
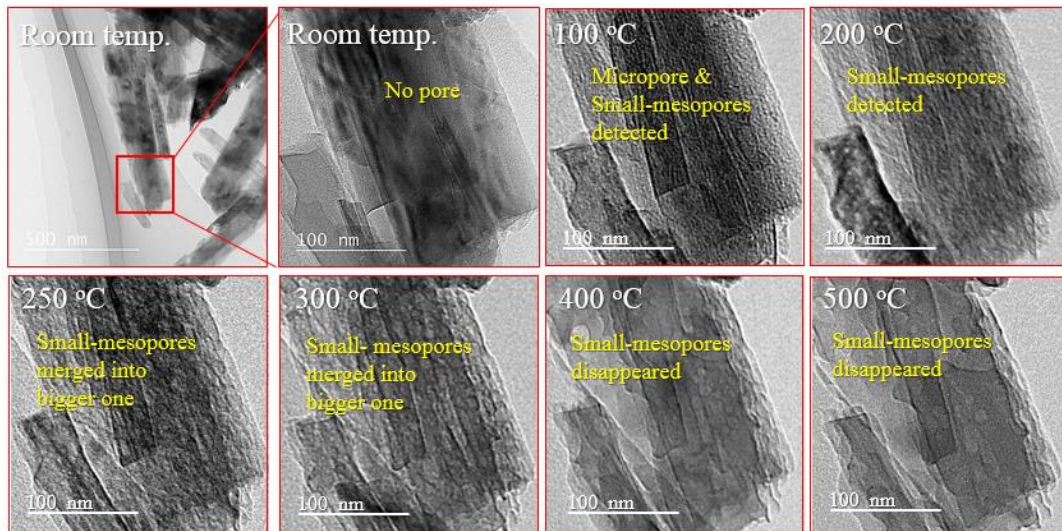


Figure 2.1.5 Pore properties of iron oxide and ores from high-vacuum dehydration at 300 °C.

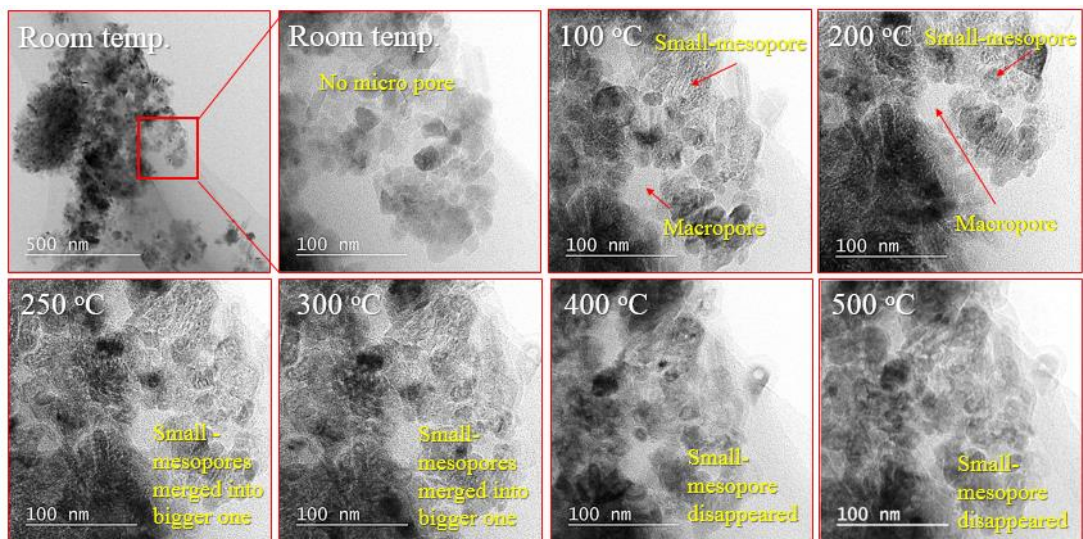
2.1.3.3. Dehydration behavior on ultra-high vacuum condition

The *in-situ* TEM result in Figure 2.1.6 and 2.1.7 show that both FeOOH reagent and GA ore having the nanocrack formation at elevated temperatures. Interestingly, under ultra-high-vacuum condition ($P= 5.6 \times 10^{-6}$ Pa), FeOOH dehydration generating nanopore starts to occur at 100 °C. The dehydration temperature seems closer to the theoretical FeOOH dehydration temperature of 83 °C. In the ultra-high vacuum condition, the removal of CW from iron oxide structure extremely faster. This is due to the driving force of CW removal under ultra-high vacuum condition become much higher than other conditions. Small-mesopores are generated at 100 – 300 °C then start to disappear significantly at 400 °C by merging into the bigger pore size. In the case of natural iron ore (GA ore), the small-mesopore starts to be generated at 100 °C. Most of the slit-shaped pores are generated at 200 - 300 °C. At higher than 300 °C, the slit-shaped pore starts to vanish, merging into a larger round-shaped (cylindrical) pore.



Remarks: White is pore

Figure 2.1.6 In-situ TEM images on ultra-high vacuum dehydration ($P = 5.6 \times 10^{-6}$ Pa) of FeOOH reagent.



Remarks: White is pore

Figure 2.1.7 In-situ TEM images on ultra-high vacuum dehydration ($P = 5.6 \times 10^{-6}$ Pa) of GA ore.

2.1.4. Resume

Porous ore utilization is a crucial point to apply high reactivity ore reduction. Vacuum condition significantly reduces the time for dehydration of goethite-based ore. However, it might not significantly reduce the dehydration temperature under mild- and high-vacuum pressure. Goethite ore high-vacuum-dehydration is finished within 1 h at 300 °C producing nanoporous hematite ore. Using in-situ TEM observation, under the ultra-high vacuum condition, the removal of CW from iron oxide structure extremely faster and decreasing temperature of goethite dehydration is possible. Small-mesopores are generated at 100 – 300 °C then start to disappear significantly at 400°C by merging into the bigger pore size.

References

- [1] Hata, Y., Purwanto, H., Hosokai, S., Hayashi, J.I., Kashiwaya, Y. and Akiyama, T., 2009. Biotar ironmaking using wooden biomass and nanoporous iron ore. *Energy & Fuels*, 23(2), pp.1128-1131.
- [2] Kashiwaya, Y. and Akiyama, T., 2010. Nanocrack formation in hematite through the dehydration of goethite and the carbon infiltration from biotar. *Journal of Nanomaterials*, 2010, p.18.
- [3] Miura, K., Miyabayashi, K., Kawanari, M. and Ashida, R., 2011. Enhancement of reduction rate of iron ore by utilizing low grade iron ore and brown coal derived carbonaceous materials. *ISIJ international*, 51(8), pp.1234-1239.
- [4] Cahyono, R.B., Saito, G., Yasuda, N., Nomura, T. and Akiyama, T., 2014. Porous ore structure and deposited carbon type during integrated pyrolysis–tar decomposition. *Energy & Fuels*, 28(3), pp.2129-2134.
- [5] Hosokai, S., Matsui, K., Okinaka, N., Ohno, K.I., Shimizu, M. and Akiyama, T., 2012. Kinetic study on the reduction reaction of biomass-tar-infiltrated iron ore. *Energy & Fuels*, 26(12), pp.7274-7279.
- [6] Saito, G., Nomura, T., Sakaguchi, N. and Akiyama, T., 2016. Optimization of the Dehydration Temperature of Goethite to Control Pore Morphology. *ISIJ International*, 56(9), pp.1598-1605.

2.2. Integrated Pyrolysis–Tar Decomposition over Low-Grade Iron Ore for Ironmaking Applications: Effects of Coal–Biomass Fuel Blending

(As presented in Kurniawan, A., Abe, K., Nomura, T. and Akiyama, T., 2017. Energy & Fuels, 32(1), pp.396-405.)

2.2.1. Introduction

In modern blast furnace operation (a typical case in Japan) 385 kg of coke per ton hot metal is needed, while 112 kg of pulverized coal per ton hot metal is injected [1]. For every ton of coke produced, around 1.6 ton of coking coal is used [2]. The coking coal (the high-grade coal) now become limited availability, and higher cost [3]. Instead of the low-grade coals (i.e., sub-bituminous or lignite coals), different fuel types are available for CVI ironmaking such as woody biomass have also gained much attention solving environmental concerns as well as reducing greenhouse gas emissions. Furthermore, utilization of any individual biomass material faces typically several problems, such as seasonal harvesting which limits year-round availability, higher transportation costs, and lower fuel-qualification properties [4].

The co-utilization of different fuels is an attractive way to solve these problems. Recently, tremendous experiments have been conducted to study the co-pyrolysis of biomass and coal and led to different conclusions. A number of studies have reported a synergetic effect in the co-processing of coal and biomass, in particular, during co-pyrolysis and co-gasification [5-7]. This co-processing synergy is likely due to the higher hydrogen/carbon molar ratio (H/C) of biomass compared with coal, which could facilitate coal decomposition [5,6,8]. In previous coal-biomass co-pyrolysis studies, however, reports of synergetic effects on the kinetics and product distributions vary when using coal-biomass blends [9-11]. This difference might depend on the experimental conditions

used, such as temperature, pressure, heating rate, type of reactor, type of coal, type of biomass, and biomass blending ratio (BBR) [12-14]. Many co-pyrolysis studies have been performed using thermogravimetric analysis (TGA). In fact, synergies have only been noted for very low-rank coal, where coal and biomass volatile evolution regimes overlap [15].

Thermochemical conversion of carbonaceous materials such as coal and biomass is a complex process involving numerous homogeneous and heterogeneous reactions [16]. Conversion begins with the pyrolysis or devolatilization reaction, a thermal decomposition process resulting in the release of various gases and tar from the feed while leaving a high carbon char [17].

Although co-pyrolysis has been already proposed and studied from so many viewpoints as described above, yet none has studied the effect of coal-biomass co-pyrolysis that to be applied in CVI process for ironmaking that was developed by previous researchers [1]. Herein, the effect of the BBR on coal-biomass integrated co-pyrolysis–tar decomposition over low-grade iron ore was studied, including changes in product distribution behavior influenced by the blending ratio. Furthermore, a kinetic study of the co-pyrolysis at different BBRs using 2-DAEM was also useful to be performed to improve understanding of the co-pyrolysis phenomena. The objective of this study is to find the synergetic effect of BBRs on coal-biomass during integrated co-pyrolysis–tar decomposition over low-grade iron ore.

This subsection investigates the effect of different fuels and its combination in the CVI process, dividing into solid-based fuel and fluid-based fuel.

2.2.2. Experimental Methods

2.2.2.1. Materials

Indonesian sub-bituminous coal, woody biomass, and polyethylene reagent were used as carbonaceous materials in this study. The proximate and ultimate analyses are shown in Table 2.2.1. Both materials were crushed and sieved to a granular size of 125–355 μm . To observe the co-pyrolysis effect, coal and biomass were hand-mixed at BBRs of 0%, 25%, 50%, 75%, and 100%.

Table 2.2.1 Proximate and ultimate analysis of Indonesian coal and woody biomass sample.

Sample	Proximate [mass%, air-dried basis]				Ultimate [mass%, dry ash free basis]				
	VM	Ash	FC	TM*	C	H	N	S	O**
Tanjung Enim sub-bituminous coal, coal	45.2	5.7	49.1	11.7	65.7	4.9	1.1	0.7	27.6
Calliandra calothyrsus wood, biomass	72.4	2.0	15.9	9.7	52.0	6.2	0.6	0.00	41.2

VM, Ash, FC, = Volatile matter, Ash content, Fixed carbon

TM* = Total moisture (% as received basis)

C, H, N, S = Carbon, Hydrogen, Nitrogen and Sulphur content

O** = Oxygen content was calculated by different

Two types of iron ores: Australian limonite and Indonesian laterite ores were utilized in this experiment with the properties shown in Table 2.2.2. The ore was crushed and sieved to obtain samples with similar particle sizes, ranging from 0.95–2 mm. In order to both increase surface area and form porous material, the ore was dehydrated at 723 K with a heating rate of 3 K min^{-1} and a holding time of 4 h in air atmosphere. Dehydration at 723 K should be enough for dehydration because it has been reported that combined water (CW) starts to decompose at 603 K and is completely removed at 723 K, changing goethite (FeOOH) to hematite (Fe_2O_3) [23]. In order to confirm this effect, the average pore volume, Brunauer–Emmett–Teller (BET) surface area, and pore distribution of the sample ore were measured using a gas adsorption measurements (Autosorb 6AG, Yuasa Ionics Co. Ltd., Osaka, Japan).

Table 2.2.2 Properties Sebuku (Indonesian) iron ore sample.

Parameter	Value
Particle size [mm]	0.95-2.00
Total Fe content [mass%]	51.41
SiO ₂ content [mass%]	3.04
Ni content [mass%]	0.48
Al ₂ O ₃ content [mass%]	7.21
Combined water content [mass%]	9.02

2.2.2.2. Thermogravimetric analysis on biomass-coal and PE-coal co-pyrolysis

Thermogravimetric (TG) curves were obtained by pyrolysis experiments using a Mettler Toledo DSC-1. Coal, biomass, polyethylene (PE) and their blends were dried at 482 K for 24 h prior to the TG experiment. The sample weights were adjusted to be close to 5 mg, and an argon flow (100 NmL min⁻¹) was continuously maintained. The experiments were carried out in dynamic temperature conditions; in this case the pyrolysis temperature was varied from 298–1073 K with a constant heating rate of 50 K min⁻¹. All data were then analyzed to investigate the effect of co-pyrolysis from its decomposition phenomena.

2.2.2.3. Integrated pyrolysis–tar decomposition

A co-pyrolysis effect on integrated biomass-coal pyrolysis–tar decomposition was observed by comparing the product distribution at each different biomass blending ratio (BBR). A quartz reactor tube (inner diameter of 30 mm, the height of 550 mm) equipped with a temperature-controlled furnace was used to conduct the tar decomposition and carbon deposition experiments as shown in Figure 2.2.1. Experiments were performed at atmospheric pressure with an N₂ flow of 250 mL min⁻¹ (STP). Solid fuel was continuously added to the reactor using a bowl feeder at a rate of 0.1 g min⁻¹ for 40 min after the reactor reached the constant temperature needed for pyrolysis and tar

decomposition at 1073 and 873 K, respectively. Cahyono et al. have discussed the selection of these temperatures previously.³⁴

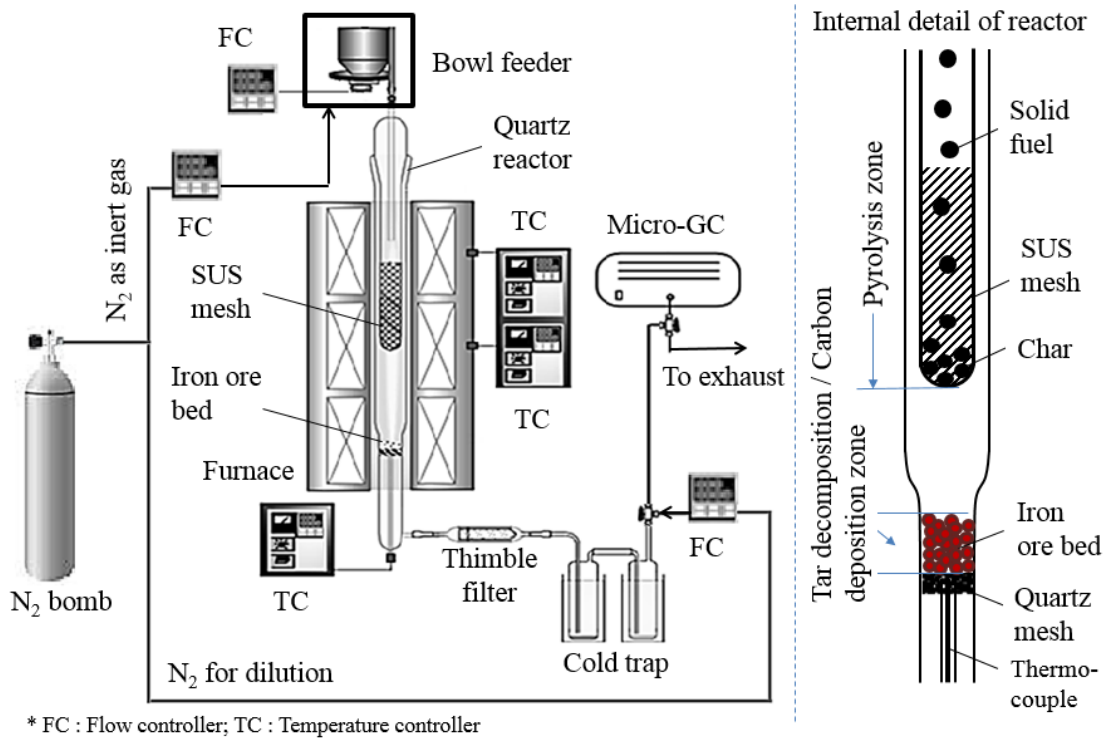


Figure 2.2.1 Apparatus configuration for integrated pyrolysis-tar decomposition-carbon deposition over iron ore

The char product was collected using a Steel Use Stainless (SUS) 304 mesh (aperture diameter of 40 μm , wire diameter of 30 μm), while the tar vapor and gases were flowed directly through to the iron ore bed (3 g) for the tar decomposition process. Tar product was collected separately as heavy and light tar. Tar trapped in the thimble filter (383 K) was measured as heavy tar by adapting Xu et al.'s methods [25]. While remaining tar collected in the cold trap (200 K) was measured as light tar. Incondensable gases were diluted with an N_2 flow of 400 mL min^{-1} (STP), and then measured using a gas chromatograph (Agilent 3000, INFICON Co., Ltd., Yokohama, Japan) to observe the H_2 , CH_4 , CO , and CO_2 produced during the process. Char structure was observed using scanning electron microscopy (SEM; JSM-7001FA, JEOL, Tokyo, Japan). Ore structure

and composition were characterized using X-ray diffractometry (XRD; Miniflex, Rigaku, Tokyo, Japan), while a gas adsorption measurement (Autosorb 6AG, Yuasa Ionics Co. Ltd., Osaka, Japan) was used to examine changes in the surface area, average pore diameter, and pore size distribution. The carbon content within the iron ore was measured using a CHN/O/S elemental analyzer (CE-440; EAI, United States). From these experimental results, effects on the BBR were evaluated by performing experiments using combined coal-biomass at different blending ratios while observing the product distributions.

2.2.3. Result and Discussion

2.2.3.1. Thermal decomposition behavior of coal-biomass co-pyrolysis.

Pyrolysis characteristics of coal-biomass blending at different BBRs were observed using thermogravimetric (TG) analysis at 50 K min^{-1} in an inert atmosphere (Figure 2.2.2). A biomass blending ratio of 0% (BBR-0%; i.e., 100% coal) has the smallest total weight loss due to its high fixed carbon content. In this case, more char and less volatiles are produced. On the contrary, BBR-100% (i.e., pure biomass) has the highest weight loss due to the high volatile matter content of biomass consisting mainly of tars and pyrolytic water, which are released much earlier than in the case of coal pyrolysis. The differential thermogravimetric (DTG) curve shows the decomposition rate peaks of the coal-biomass blends. Two decomposition rate peaks observed in one DTG curve for BBR-0% can be attributed to a two-step pyrolysis decomposition process. An additional shoulder peak occurring after the decomposition peak in the DTG curve for BBR-100% was also observed. Coal and biomass are individually pyrolyzed in a primary reaction step that mainly results in the devolatilization of light components as light tar

and gases. The mixture of components produced from coal and biomass triggers the synergetic effect in a secondary reaction step that results in aromatization of macromolecules, thereby producing char while continuing to release gases. This reaction also involved reforming, water-gas shift, cracking, dehydration, oxidation, polymerization, and gasification reactions.³⁶

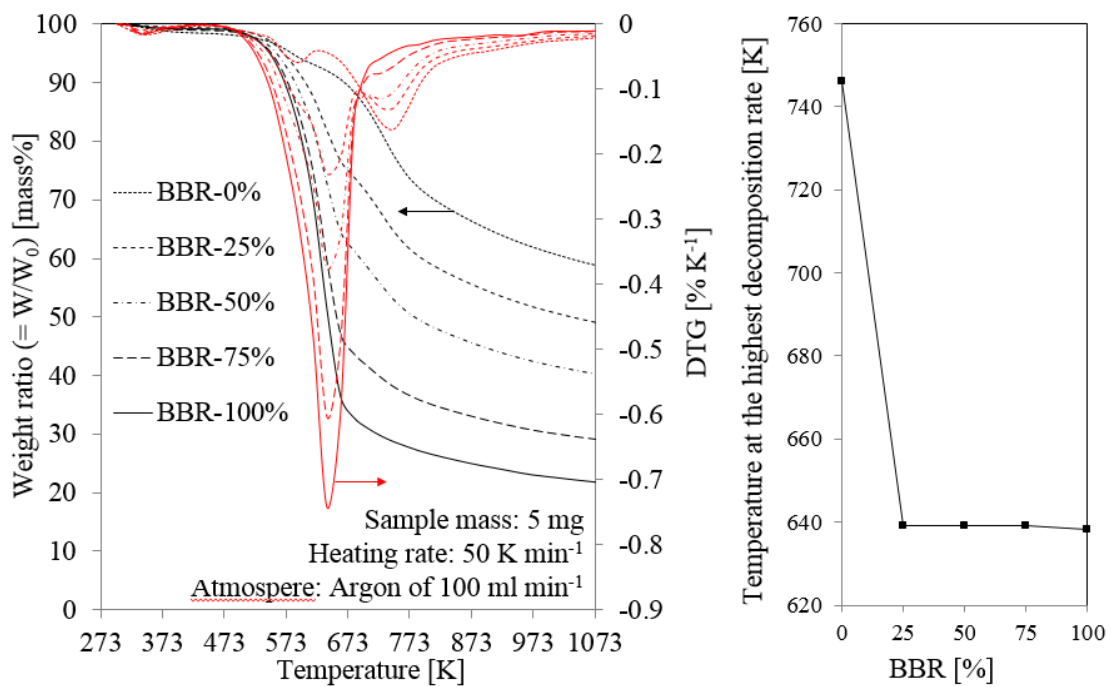


Figure 2.2.2 TG/DTG profiles and the highest decomposition rate temperatures for coal-biomass blending with different BBRs during pyrolysis; coal and biomass particle size, 125–355 μm .

Corresponding to the pyrolysis temperature in Figure 2.2.2, the highest decomposition rate of BBR-0% occurs at a higher temperature, while BBR-100% has a lower decomposition temperature. The temperature of the highest decomposition rate of coal-biomass co-pyrolysis decreases with increasing BBR. In fact, the temperature of biomass decomposition depends on the cellulose, hemicelluloses, and lignin content. However, cellulose is mainly responsible for volatiles; lignin is the main contributor to char, while hemicelluloses contribute almost equally to both.⁴⁰ It is obvious that the temperature decrease is not linearly proportional to the BBR, which means that

introducing 25wt% of biomass to coal pyrolysis can cause a significant shift of pyrolysis temperature. This is probably due to the volatile compound generated from biomass might cause convective mass transfer effect that promotes more decomposition rate in coal particle. Another report also described that biomass has a strong cooling effect of pyrolysis that could lower pyrolysis temperature that is caused by two reasons.⁴¹ First, the pyrolysis process is an endothermic reaction. Second, when the generated volatile flowed through the particle from inside to outside, it would cause convective cooling effects on the particle.

2.2.3.2. Kinetic study on coal-biomass co-pyrolysis using the distributed activation energy model (DAEM).

The synergetic effect on coal-biomass co-pyrolysis is not explicitly shown from mass changes in the TG experiment (Figure 2.2.2), apart from the temperature shift of the highest decomposition rate in the DTG curve. However, this temperature shift could be interpreted as the shift of the activation energy obtained from the kinetic study of pyrolysis which means different decomposition reaction occurs in coal-biomass blending. However, the decomposition reaction is very complex and hard to be observed during the experiment. The kinetic study could be more convenient tools to investigate the decomposition reaction as well as to observe the synergetic effect of coal-biomass blending. Some researchers reported that a complex reaction occurred during pyrolysis that could be approximated using the distribution activation energy model (DAEM) that was first introduced by Vand, however, still under development [13-21]. Filippis et al. had successfully developed and performed a model based on a double distribution of the activation energy (2-DAEM). This model was able to adequately describe the two

separate steps of primary and secondary pyrolysis, which characterized the thermochemical processing of most of the energetic materials [22]. The method is also attractive for analyzing the synergetic effect of combining coal-biomass on the pyrolysis from a kinetic viewpoint.

The basic assumption of the DAEM is that many solid fuel decomposition reactions take place during pyrolysis. It can be simply approached as a sum of an unlimited number of parallel first order decomposition reactions. Applying the multiple Gaussian distributions of activation energy, so the DAEM equation can be written as:

$$X_{calc} = \sum_{i=1}^n \int_{E=0}^{\infty} \exp\left(-\frac{k_{0i}}{\beta} \int_{T_0}^T \exp\left(-\frac{E}{RT}\right) dT\right) \left(\frac{1}{\sigma_i \sqrt{2\pi}} \exp\left(-\frac{(E - E_{0i})^2}{2\sigma_i^2}\right)\right) dE \quad (2.2-1)$$

where X_{calc} is the calculated residual volatile fraction of solid fuel at a given time [-]; n is the number of activation energy distributions; β is the heating rate [K s^{-1}]; k_{0i} is the pre-exponential factor of constituent i [s^{-1}]; σ_i is the activation energy variance of constituent i , [kJ mol^{-1}]; E_{0i} is the mean activation energy of constituent i , [kJ mol^{-1}]; R is the gas constant [$\text{J mol}^{-1} \text{K}^{-1}$]; and T is the absolute temperature [K]. Gašparovič et al. reported that a constant pre-exponential factor for every decomposition reaction can be assumed for various activation energies [20]. Additionally, De Filippis et al. reported that coal and biomass pyrolysis were satisfactorily modeled using a double distribution of the activation energy (2-DAEM) by applying weighting factor w for each Gaussian distribution functions [22]. Adapting those previous methods, the 2-DAEM equation becomes:

$$X_{calc} = \sum_{i=1}^2 \int_{E=0}^{\infty} \exp\left(-\frac{k_{0i}}{\beta} \int_{T_0}^T \exp\left(-\frac{E}{RT}\right) dT\right) \left(\frac{w_i}{\sigma_i \sqrt{2\pi}}\right) \exp\left(-\frac{(E - E_{0i})^2}{2\sigma_i^2}\right) dE \quad (2.2-2)$$

where w_i means the contribution ratio of each reaction [-]. While $\sum_{i=1}^2 w_i = 1$.

Furthermore, the parameter k_{0i} of each constituent can be set at the same constant value as k_0 to increase the independency of parameters estimation. Thus the 2-DAEM equation can be expressed as

$$X_{calc} = \int_{E=0}^{\infty} \exp\left(-\frac{k_0}{\beta} \int_{T_0}^T \exp\left(-\frac{E}{RT}\right) dT\right) \left(\frac{w}{\sigma_1 \sqrt{2\pi}} \exp\left(-\frac{(E - E_{01})^2}{2\sigma_1^2}\right) + \dots \right. \\ \left. \frac{(1-w)}{\sigma_2 \sqrt{2\pi}} \exp\left(-\frac{(E - E_{02})^2}{2\sigma_2^2}\right)\right) dE \quad (2.2-3)$$

The X_{calc} in eq. (2.2-3) represents the volatile fraction of the sample during pyrolysis, and can be experimentally evaluated from the TG data according to the equation:

$$X_{exp} = \frac{m_0 - m}{m_0 - m_f} \quad (2.2-4)$$

where X_{exp} is the observed residual volatile fraction at time t [-]; m is the remaining mass obtained experimentally at time t [mg]; m_0 and m_f are the initial mass [mg] and the mass at final temperature [mg], respectively.

Therefore, in eq. (2.2-3), only five parameters are estimated: contribution factor w , two mean activation energies, E_{01} and E_{02} coupled with two standard deviations σ_1 and σ_2 . These five parameters were estimated by a curve fitting method using the sum square error (SSE) as the objective function (eq. (2.2-5)).

$$\text{SSE} = \sum \left(X_{\text{calc}} - X_{\text{exp}} \right)^2 \quad (2.2-5)$$

Numerical solution for Eq.(2.2-3) was performed in MATLAB® adapting the Gašparovič et al. algorithm. Numerical integration for E-term and T-term of eq.(2.2-3) was calculated using "TRAPZ" and "QUADL" function, respectively. Integration limit of E-term and T-term were set from 0 to 500 kJ mol⁻¹ and 293 K to 1073 K, respectively. The curve fitting using this model was only limited to the decomposition process of solid fuel. Curve fitting was performed by running an optimization program to minimize the SSE value of 105 data points in eq. (2.2-5) using "LSQNONLIN" function with iteration parameters "TolX" = 1e-7; "TolFun" = 1e-7; "MaxIter" = 10000; "MaxFunEvals" = 10000. The parameter k_0 was set to 10¹³. The initial guessing value of the parameters w , E_{01} , E_{02} , σ_1 and σ_2 were 0.5, 200, 200, 5, and 5, respectively. Lower boundary for all parameters were set to zero. The goodness of fit using R^2 were also calculated. The activation energy distribution was then plotted and analyzed ranging at 0 – 400 kJ mol⁻¹ to investigate the effect of combined coal-biomass in pyrolysis at different blending ratios.

The curve fitting method was performed using the double-distributed activation energy model (2-DAEM). Figure 2.2.3(a) shows the curve fitting results of a 2-DAEM model that was satisfactorily fitted to the experimental data. Table 2.2.3 shows the obtained fitting parameters at different BBRs with SSE and the goodness of fit using R^2 for each curve are provided.

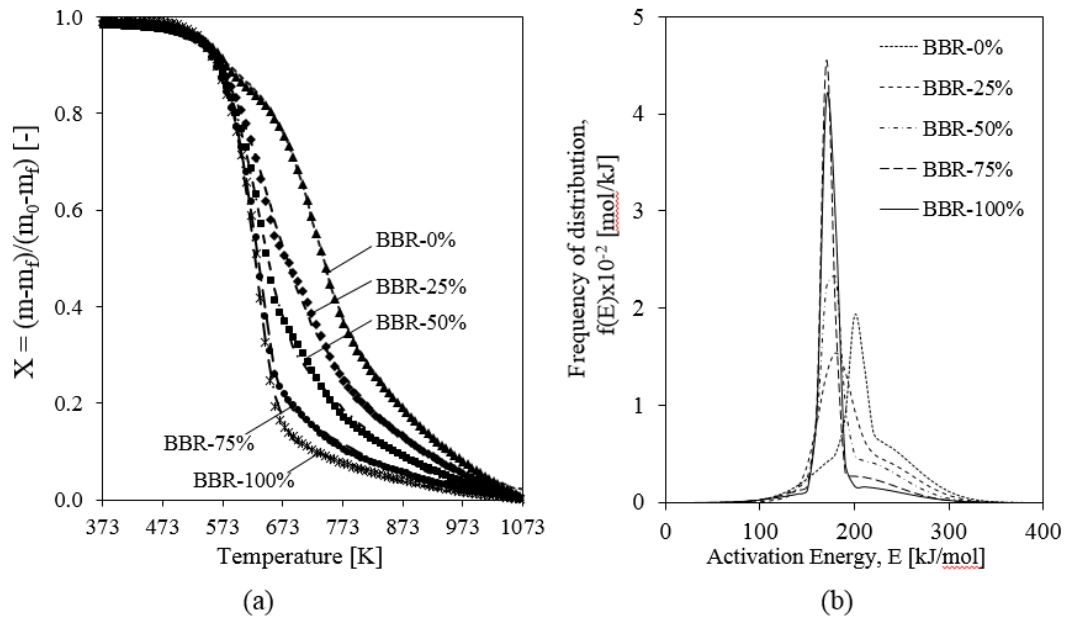


Figure 2.2.3 (a) Comparison between the experimental data (dotted lines) and the curves calculated by the 2-DAEM (dashed lines) at different BBRs. (b) Double Gaussian activation energy distribution curves for coal-biomass co-pyrolysis at different BBRs obtained from the 2-DAEM fitting.

Table 2.2.3 Kinetic parameter of thermal decomposition at various biomass blending ratio (BBR) obtained from 2-DAEM method with the Gaussian distribution.

Parameter	BBR0%	BBR25%	BBR50%	BBR75%	BBR100%
k_0 [1/s] (fixed)	10^{13}	10^{13}	10^{13}	10^{13}	10^{13}
E_{o1} [kJ/mol]	202.3	178.8	175.2	171.3	173.0
E_{o2} [kJ/mol]	214.1	218.2	204.1	197.1	197.6
σ_1 [kJ/mol]	7.2	16.4	9.2	6.1	7.1
σ_2 [kJ/mol]	45.9	43.2	44.7	46.8	51.9
w [-]	0.24	0.50	0.51	0.68	0.78
SSE	4.69×10^{-3}	8.76×10^{-3}	8.36×10^{-3}	5.17×10^{-3}	7.29×10^{-3}
R^2	0.9993	0.9989	0.9991	0.9995	0.9994

Figure 2.2.3(b) shows the activation energy distribution curves for coal-biomass co-pyrolysis at different BBRs according to the simultaneous 2-DAEM using the Gaussian distribution function. The coal has two ranges of activation energy distribution from 195–209 kJ mol⁻¹ and 168–260 kJ mol⁻¹ with mean activation energies of 202.3 kJ mol⁻¹ and 214.1 kJ mol⁻¹, respectively, with the value of parameter w is 0.24. The shape of its distribution curve shows that the activation energy of primary pyrolysis is

superimposed with the secondary reaction. This result is similar to a report by Fillipis et al. for Sulcis (subbituminous) coal that has two range of activation energy distributions of 195–209 kJ mol⁻¹ and 185–289 kJ/mol with mean activation energy of 202 kJ mol⁻¹ and 237 kJ mol⁻¹, respectively, with the value of parameter w is 0.44 [22]. The two activation energy distribution ranges correspond to the two decomposition steps occurring during pyrolysis. The first peak of the distribution contributes to the primary step which light tar and gases are released at a lower temperature whereas the second peak of activation energy distribution corresponds to the secondary step which macromolecules are aromatized to produce char while gases continue to be released [32,33]. The superimposed two Gaussians could be interpreted as the cross-linking reactions and char condensation begin at the same time of the primary decomposition step. However, it is agreed that primary pyrolysis occurs in a narrower range of activation energy than secondary peak that means this process is fast. The secondary pyrolysis step is slower and requires more energy to be accomplished. Meanwhile, biomass has narrower ranges of activation energies, 165–180 kJ mol⁻¹ and 145–249 kJ mol⁻¹ with mean activation energies of 173.0 kJ mol⁻¹ and 197.6 kJ mol⁻¹, respectively, with the value of parameter w is 0.78. Similar result also reported by other researchers [19,22]. The narrower range of activation energies of biomass means that it has faster decomposition than coal. The higher value of parameter w for biomass means that the overall biomass pyrolysis reaction is highly dominated by primary decomposition step. It corresponds to the biomass exhibits more rapid gas evolution than coal due to the relatively lower bond energies of ether (R–O–R) and C–C bonds associated with lignocellulosic biomass, compared to the aromatic C=C bonds typically found in coal [33]. At higher BBR, primary decomposition peak shifts to the lower activation energy

meaning the primary decomposition reaction seem correlate to the shift of pyrolysis temperature (Figure 2.2.1b). In this case, the biomass behavior predominates the primary decomposition of the blending, thereby contributing to the more volatiles released. In contrast, the secondary peaks of activation energy distributions become lower at higher BBRs. The behavior of secondary decompositions seems to be dominated by coal. The higher amount of coal in the blends would increase the number of secondary decomposition reactions. At BBR-25%, the activation energy distribution curve of primary decomposition obviously has a different trend. The wider range of the primary peak at this blending could be interpreted as the interaction coal and biomass in the blending promotes the other complex reactions resulting in the lowest number of primary decomposition comparing to other BBRs. Yet, there is slightly no trending change for secondary decomposition reaction. On the other hand, this phenomenon could also be interpreted from the value of the parameter w (Table 2.2.3) that increase at higher BBRs with the significant increase occurs at BBR-25%. In this case, introducing a small amount of biomass (25wt%) could affect the significant change in overall kinetic behavior. This effect could be called as the synergetic effect of co-pyrolysis. However, the synergetic effect of coal-biomass co-pyrolysis is confirmed only for primary decomposition reaction. This synergetic effect is confirmed in a later subsection.

2.2.3.3. The synergetic effect of co-pyrolysis on integrated coal-biomass co-pyrolysis–tar decomposition

The integrated coal-biomass co-pyrolysis–tar decomposition over low-grade iron ore was designed to reduce the tar product while simultaneously converting it to carbon deposited into the iron ore. Moreover, production of high carbon content carbonized ore

is desired. Figure 2.2.4 shows the product distribution carbon yields from integrated coal-biomass pyrolysis, both for pyrolysis only (case A), and for pyrolysis–tar decomposition over porous iron ore (3 g) (case B). The observed pyrolysis products were the carbon yield of char, heavy tar, light tar, deposited carbon in iron ore (case B only) and gas at any BBRs. Heavy tar and light tar in this experiment were separated by the boiling point according IEA tar protocol that the components with the boiling point higher than 378 K could be categorized as heavy tar fraction [25].

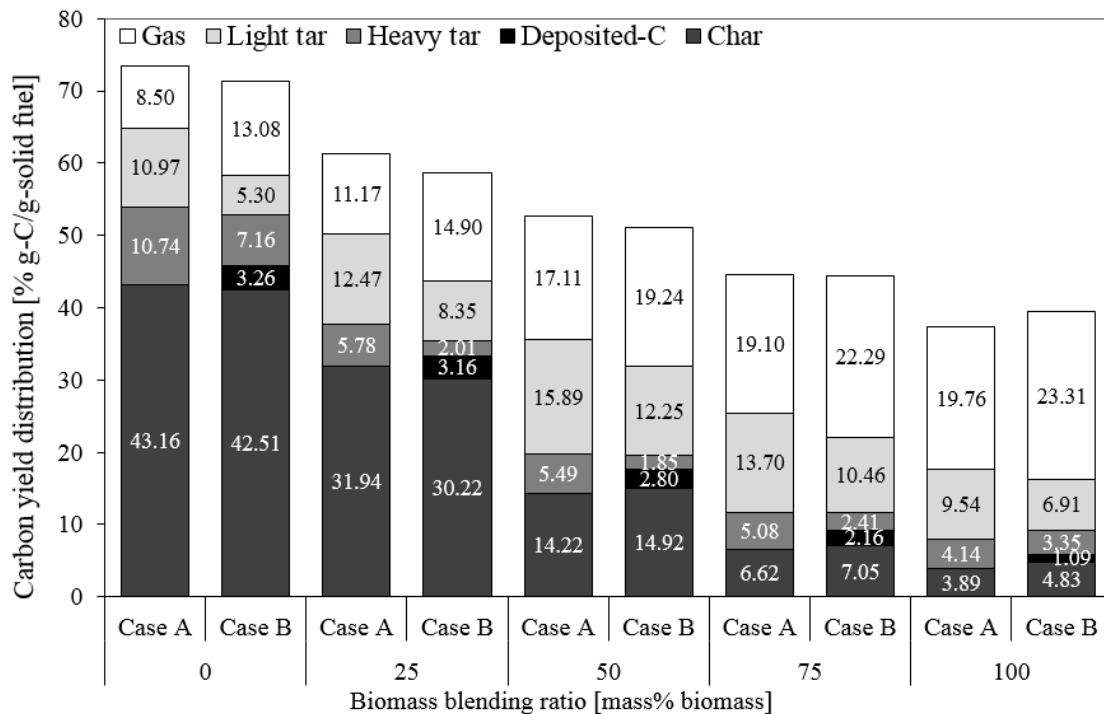
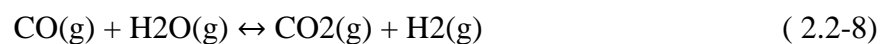
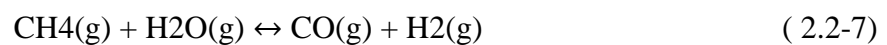
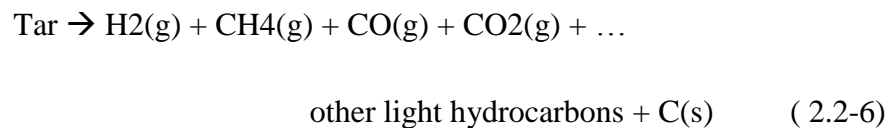


Figure 2.2.4 Carbon yield product distribution of integrated pyrolysis–tar decomposition in a N₂ atmosphere at a pyrolysis temperature of 1073 K and a tar decomposition temperature of 873 K for 40 min. Case A: co-pyrolysis only; Case B: co-pyrolysis with tar decomposition over porous iron ore (3 g).

The deposited carbon in iron ore is the carbon amount of solid fuel that deposited in iron ore bed during CVI process, which was evaluated from mass balance. In contrast, carbon content in iron ore was measured by CHN/O/S elemental analyzer. The term of the deposited carbon and the carbon content in CVI ore were introduced to distinguish

the different points of view. It was obvious that the total carbon yield of the biomass pyrolysis product is lower than the coal product since biomass has a lower carbon content than coal. Total carbon yields of the coal-biomass blends gradually decreased at elevated BBRs.

Effects of coal-biomass co-pyrolysis on gas products are shown in Figure 2.2.5. For case A, only CO gas significantly increased at higher BBRs. This is due to OH radicals from biomass attacking the aromatic rings in coal and reacting with aliphatic species, thereby generating more CO.^{11,12,20} Moreover, H₂ and CO₂ gas only changed slightly at elevated BBRs. However, co-pyrolysis had no significant effect on CH₄ production. In case B, the introduction of iron ore into tar pyrolysis increased the amount of H₂, CH₄, CO and CO₂ due to the catalytic activity of iron ore. The reactions involved were tar reforming¹¹ as in Eq. (2.2-6). The significant increase of H₂ and CO₂ at higher BBRs could be correlated to the presence of water from biomass pyrolytic tar promoting steam reforming as in Eq. (2.2-7) and water gas shift reaction (WGSR) as in Eq.(2.2-8).



Another researcher reported that Fe₂O₃ has a good catalytic activity for steam reforming [34] and WGSR [35]. However, H₂ was found decrease at BBR-100%. This was probably due to H₂ is consumed by hydrocracking process of biomass tar [36]. Blending coal to biomass could provide sufficient carbon amount in gas promoting more H₂ through steam reforming and WGSR to overcome the H₂ consumption of hydrocracking process. In this case, the water content in tar could be an important role in

the gas reaction. An investigation of the effect of water content in tar decomposition is necessary to be conducted. This will be left for the next future study.

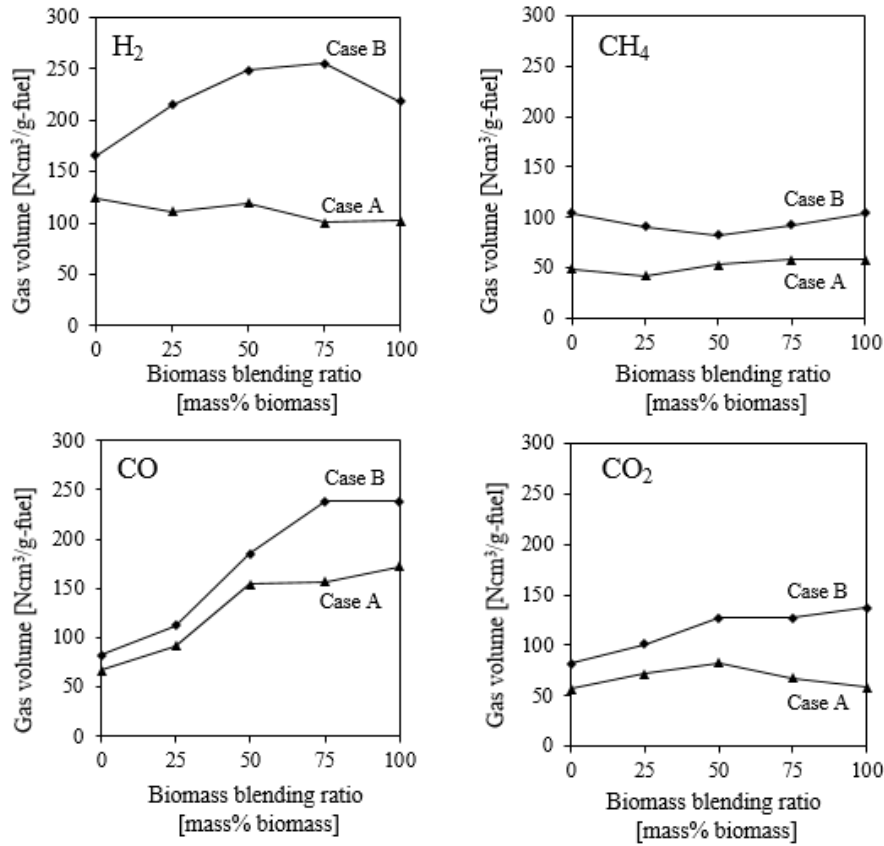


Figure 2.2.5 Effect of co-pyrolysis at different BBRs on gas H₂, CH₄, CO, and CO₂ product distribution of integrated pyrolysis–tar decomposition in N₂ atmosphere. Pyrolysis and tar decomposition temperatures were 1073 K and 873 K, respectively. The reaction time was 40 min. Case A: pyrolysis; case B: integrated pyrolysis with tar decomposition over porous iron ore (3 g).

The linear reference line method was preferable to observe the synergetic effect of co-pyrolysis for each pyrolytic product. Synergetic effects can be approximated by the deviation of each observed datum and the reference line, as expressed in equation (2.2-9).

$$\delta_i = \frac{y_i - y_{i\text{ref}}}{y_{i\text{ref}}} \quad (2.2-9)$$

where δ_i is the calculated synergetic effect at different BBRs, y_i is the observed data of each product, $y_{i\text{ref}}$ is the reference line calculated as $(= \frac{y_{100}i + y_0(100-i)}{100})$, and i is the experimental BBR percentage. The non-zero deviation value means that the synergetic effect occurs in coal-biomass blending. All synergetic effects were clearly found on co-pyrolysis product distributions in both case A and case B (Figure 2.2.6). In case A, synergetic effects of coal-biomass co-pyrolysis contribute to decreased char and heavy tar with increased light tar and gas products. In case B, the effect became more significant after introducing tar decomposition over porous iron ore. Overall, a significant synergetic effect occurred at BBR-50%.

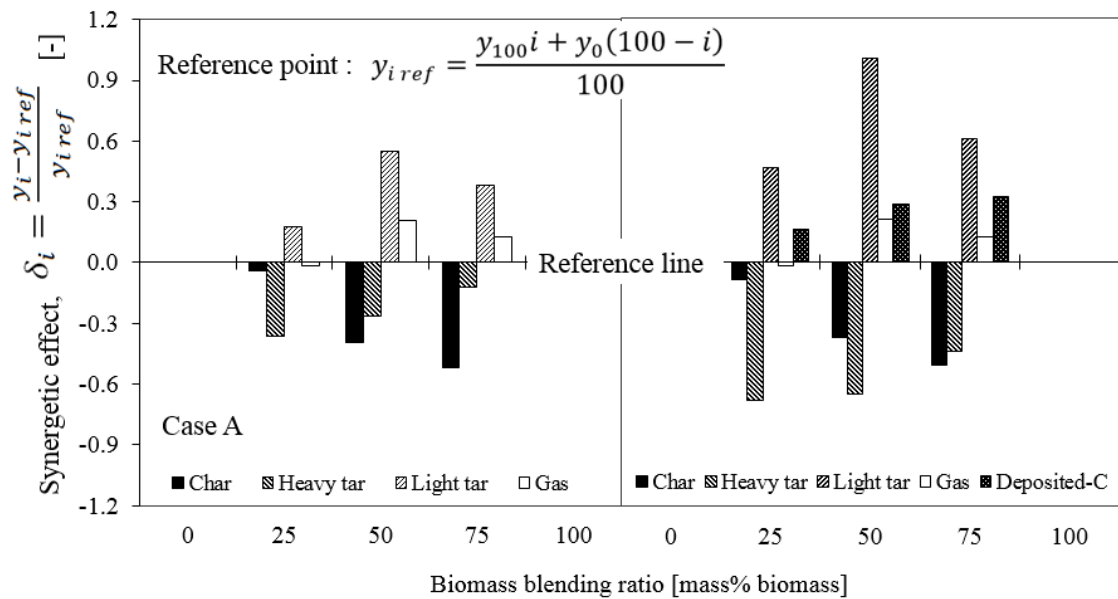


Figure 2.2.6 The synergetic effect on carbon yield product distributions of integrated pyrolysis–tar decomposition in an N_2 atmosphere at a pyrolysis temperature of 1073 K and tar decomposition temperature of 873 K for 40 min. Case A: co-pyrolysis only; case B: co-pyrolysis with tar decomposition over porous iron ore (3 g).

Char products tended to decrease at elevated BBRs. The highest amount of synergy on char was found at BBR-75%. Char that was captured in SUS mesh in both cases was not influenced by the presence of iron ore; therefore, this could be confirmed

as the reproducibility of the synergetic effect on char. SEM observations on char particles confirmed the synergetic effect of co-pyrolysis on char (Figure 2.2.7). Coal chars (a1 – a4) and biomass chars (b1-b4) remained still maintain their round shape and flakes-like shape, respectively. So, it could be distinguished between them in the char mixture at any BBRs. Coal chars from coal only (a1) seems only had a small number of cracks and pores on its surface. While after blending with biomass, more cracks and pores were formed on the coal char surface. The morphology of coal char in the blend then became a loosely packed, more porous structure at elevated BBRs (a2-a4). The largest pore was observed on coal char surface at BBR-75% (a4). However, there was little to no change in biomass char in the blend during co-pyrolysis. This was probably due to volatile matter in the biomass promoting more coal particle decomposition, but the opposite was not observed.

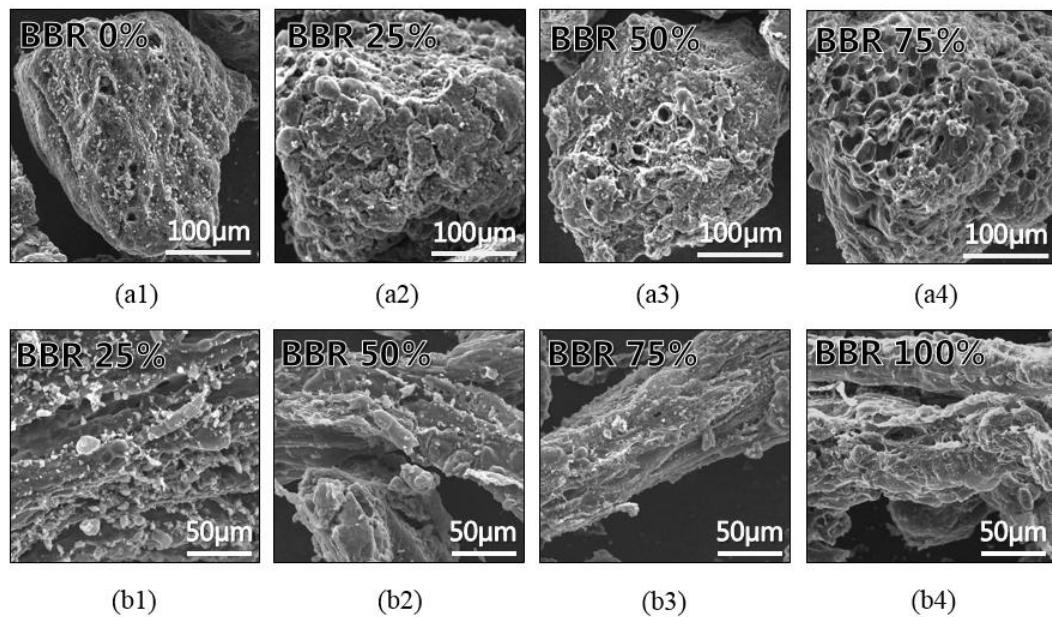


Figure 2.2.7 SEM images of pyrolysis char products at different BBRs in an N₂ atmosphere at 1073 K for 40 min. Coal char particles at BBR-0%, 25%, 50%, and 75% are shown in a1, a2, a3, and a4, respectively. Biomass char particles at BBR-25%, 50%, 75%, and 100% are shown in b1, b2, b3, and b4, respectively.

A synergetic effect of coal-biomass co-pyrolysis was also found for tar decomposition (Figure 2.2.8). The effect was observed on the amount of reacted tars

during tar decomposition and on the ratio of deposited carbon (Figure 2.2.8(a)). Compared to the reacted heavy tar, the deposited carbon ratio and carbon content (Figure 2.2.8(b)) have similar curve shapes and peaks to BBR-25%. The reacted heavy tar apparently contributes to increasing the deposited carbon ratio, thereby giving the carbon content increase in CVI ore. This phenomenon probably correlates with the kinetic behavior discussed earlier regarding activation energy distribution. However, a molecular investigation of the heavy tar would be needed to confirm this effect.

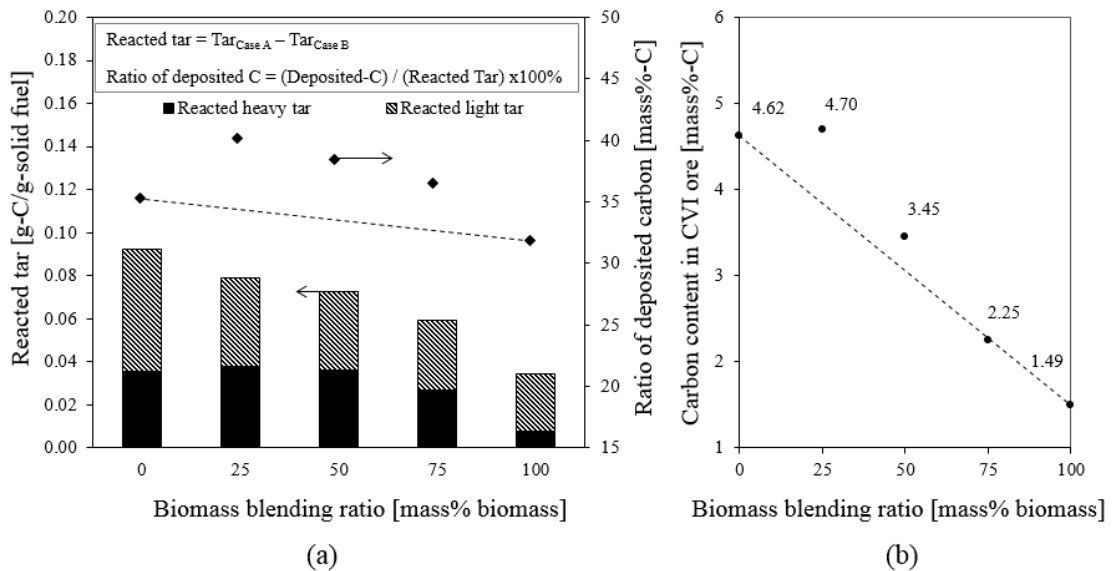


Figure 2.2.8 Effect of coal-biomass co-pyrolysis on the amount of reacted tar and the deposited carbon ratio (a) and carbon content in the CVI ore (b) during tar decomposition over porous iron ore in an N₂ atmosphere. Pyrolysis and tar decomposition temperatures were 1073 K and 873 K, respectively. The reaction time was 40 min. Case A: pyrolysis; case B: integrated pyrolysis with tar decomposition over porous iron ore (3 g).

XRD analysis was performed to clarify changes in the iron ore structure occurring during ore structure from goethite to hematite with the following reaction:



There was no FeOOH peak after dehydration at 723 K (Figure 2.2.9). Thus, the dehydration was complete at this temperature. A similar result has been reported previously [22]. The removal of combined water increased the porosity of the dehydrated

ore (Figure 2.2.10(a)). After dehydration, the ore was dominated by pores smaller than 4 nm that were then infiltrated by carbon via CVI (Figure 2.2.10(b)). Synergetic effects of coal-biomass co-pyrolysis on carbon infiltrated CVI ores were confirmed by a decrease in the BET surface area and total pore volume of the CVI ore which correlated with the carbon content in the CVI ore. However, it could not be ascribed that directly correlated by pyrolysis fuel type and BBR.

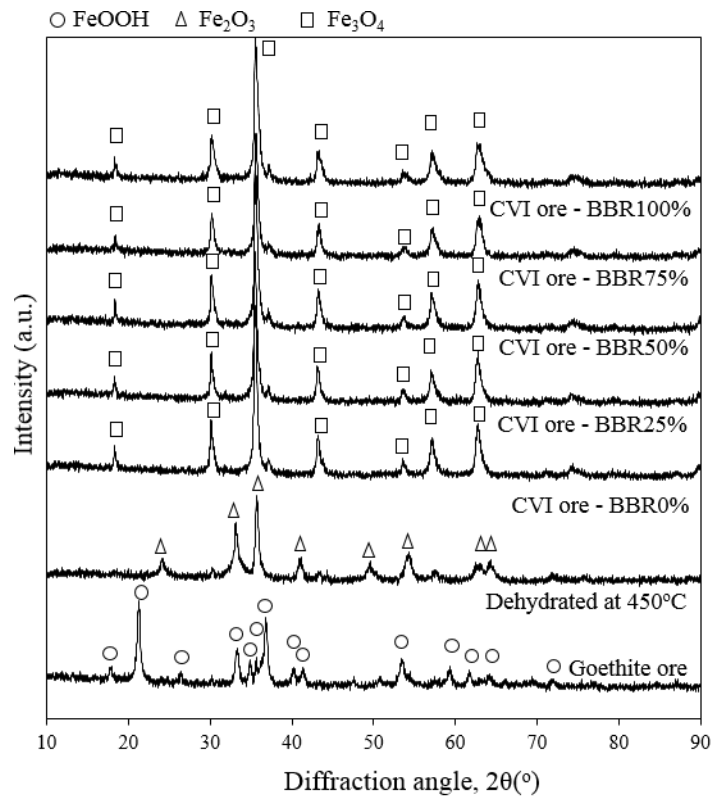


Figure 2.2.9 XRD spectra of changes in the original ore, dehydrated ore, and CVI ores. Pyrolysis and tar decomposition temperatures were 1073 K and 873 K, respectively. The reaction time was 40 min. All CVI ores had a magnetite structure during the CVI process at any BBR.

During the tar decomposition, all CVI ore obtained from different coal-biomass blends was reduced to magnetite (Figure 2.2.9). No synergetic effect was found in the reduction of hematite to magnetite corresponding to coal-biomass co-pyrolysis at any BBR in case B, which means that this reduction occurs during the tar decomposition

process at 873 K. This reduction result was agreed to other reports [1, 24]. This reduction involved prominent reactions of iron ore component with gas evolved during tar decomposition such as indirect reductions and dry gas reforming:

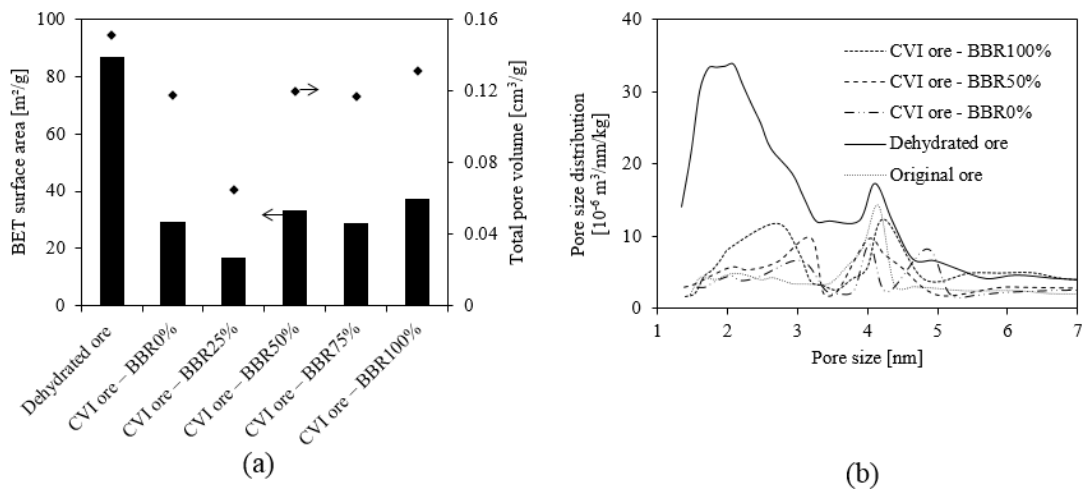
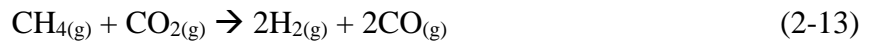


Figure 2.2.10 Effects of co-pyrolysis on total pore volume and BET surface area (a), and pore size distribution (b) of iron ore and CVI ore at different BBRs. Pyrolysis and tar decomposition temperatures were 1073 K and 873 K, respectively. The reaction time was 40 min. SAA analyzer conditions: Adsorbate N₂; molecular weight = 28.0134 g/mol; cross-sectional area = 16.2 Å²/molecule; non ideality = 6.580E-05; P/Po tolerance = 2; outgas temperature = 393 K; outgas time = 1.0 h; bath temperature = 77.35 K. All samples were dried under vacuum at 378 K for 24 h prior to SAA analysis.

2.2.4. Summary

Introducing coal-biomass co-pyrolysis to the integrated pyrolysis–tar decomposition process was attractive, since synergistic effects were observed on the pyrolysis products, and the tar decomposition process increased the carbon content of CVI ore. The following conclusions have been reached:

1. Thermogravimetric (TG) experiments showed that pyrolysis of combining coal and biomass had a synergetic effect that lower the decomposition temperature. The temperature shift had a non-linear correlation with the biomass blending ratio (BBR). A co-pyrolysis kinetic study using the 2-DAEM was performed, showing that coal-biomass blending had a synergetic effect on co-pyrolysis. However, the synergetic effect of coal biomass co-pyrolysis is confirmed only for primary decomposition reaction.
2. The reference line method was used to identify synergetic effects on each pyrolysis product. A positive synergetic effect on coal-biomass co-pyrolysis has also been found for increasing light tar and gas as well as for decreasing char and heavy tar product. Overall, a significant synergetic effect occurred at BBR-50%.
3. Coal-biomass co-pyrolysis had a synergetic effect in increasing carbon content in CVI. The highest CVI carbon content (4.70 wt%) was obtained using BBR-25%. This is due to increased reacted heavy tar contributes to increasing the deposited carbon ratio. In other words, the co-pyrolysis of coal blending with 25 wt% of biomass (which has a lower carbon amount) could produce higher carbon content CVI ore. However, the carbon content was not enough for a perfect reduction of iron ore. That is why future work still needs to be conducted to produce higher carbon content CVI ore which is required for the iron reduction process.

References

- [1] Cahyono, R.B.; Rozhan, A.N.; Yasuda, N.; Nomura, T.; Purwanto, H.; Akiyama, T., Energy Fuels. 2013, 27, 2687.
- [2] Suzuki, K.; Hayashi, K.; Kuribara, K.; Nakagaki, T.; Kasahara, S., ISIJ Int. 2015, 55, 340.
- [3] IEA, Tracking Industrial Energy Efficiency and CO₂ Emissions, 2009, 52.

- [4] Krerkkaiwan, S.; Fushimi, C.; Tsutsumi, A.; Kuchonthara, P.; Fuel Process Technol. 2013, 115,11.
- [5] Zhang, L.; Xu, S.P.; Zhao, W.; Liu, S.Q. Fuel. 2007, 86, 353.
- [6] Kumabe, K.; Hanaoka, T.; Fujitomo, S.; Minowa, T.; Sakanishi, K. Fuel. 2007, 86, 684.
- [7] Alzate, C.A.; Chejne, F.; Valdes, C.F.; Berrio, A.; De La Cruz, J.; Londono, C.A. Fuel. 2009, 88, 437.
- [8] Zhu, W.K.; Song, W.L.; Lin, W.G. Fuel Process Technol. 2008, 89, 890.
- [9] Park, D.K.; Kim, S.D.; Lee, S.H.; Lee, J.G., Bioresour. Technol. 2010, 101, 6151.
- [10] Haykiri-Acma, H.; Yaman, S. Fuel. 2007, 86, 373.
- [11] Idris, S.S.; Rahman, N.A.; Ismail, K.; Alias, A.B.; Rashid, Z.A; Aris, M.J, Bioresour. Technol., 2010, 101, 4584.
- [12] Wang, Z.; Wan, K.; Xia, J.; He, Y.; Liu, Y.; Liu, J., Energy Fuels. 2015, 29, 5036.
- [13] Yilgin, M.; Duranay, ND.; Pehlivan D. Energy Convers. Manage. 2010, 51, 1060.
- [14] Yuan, S.; Dai, Z.H.; Zhou, Z.J.; Chen, X.L.; Yu, G.S.; Wang, F.C. Bioresour. Technol. 2012, 109, 188.
- [15] Haykiri-Acma, H.; Yaman, S. Renew. Energy. 2010, 35, 288.
- [16] Higman, C.; Van der Burgt, M. Gasification. Gulf Professional Publishing: London 2011; pp 11-31.
- [17] Soncini, R.M.; Means, N.C.; Weiland, N.T. Fuel. 2013, 112, 74.
- [18] Vand, V. Proc. Phys. Soc. 1943, A55, 222.
- [19] de Caprariis, B.; Santarelli, M.L.; Scarsella, M.; Herce, C.; Verdone, N.; De Filippis, P. J. Therm. Anal. Calorim. 2015, 121(3), 1403.
- [20] Gašparovič, L.; Labovský, J.; Markoš, J.; Jelemenský, L. Chem. Biochem. Eng. Q. 2012, 26, 45.
- [21] Cai, J.; Wu, W; Liu, R. Renew. Sustainable Energy Rev. 2014, 36, 236.
- [22] De Filippis, P.; de Caprariis, B.; Scarsella, M; Verdone, N.; Energies. 2015, 8, 1730.
- [23] Akiyama T.; Takahashi R.; Yagi J.I, ISIJ-Int. 1991, 31, 24.
- [24] Cahyono, R.B.; Yasuda, N.; Nomura, T.; Akiyama, T. Fuel Process Technol. 2014, 119, 272.
- [25] Xu, M., Brown, R.C., Norton, G., Smeenk, J.; Energy Fuels. 2005, 19, 2509.
- [26] Neves, D.; Thunman, H.; Matos, A.; Tarelho, L.; Gómez-Barea, A. Prog. Energy Combust. Sci. 2011, 37, 611.
- [27] Lv, D; Xu, M.; Liu, X.; Zhan, Z.; Li, Z.; Yao, H. Fuel Process Technol. 2009, 91, 903.
- [28] Yang, H.; Yan, R.; Chen, H.; Lee, DH.; Zheng, C. Fuel. 2007, 86, 1781.
- [29] Haykiri-Acma H.; Yaman S.; Kucukbayrak S. Fuel Process Technol. 2010, 91, 759.

- [30] Wei, L.; Xu, S.; Zhang, L.; Zhang, H.; Liu, C.; Zhu, H.; Liu, S. *Fuel Process. Technol.* 2006, 87, 863.
- [31] Wan, K.; Wang, Z.; He, Y.; Xia, J.; Zhou, Z.; Zhou, J.; Cen, K., *Fuel.* 2015, 139, 356.
- [32] Kader, M.A.; Islam, M.R.; Parveen, M.; Haniu, H.; Takai, K. *Bioresour. Technol.* 2013, 149, 1.
- [33] Gaqa, S.; Mamphweli, S.; Katwire, D; Meyer, E. *Int. J. Energy Environ.* 2014, 5, 251.
- [34] Guan, G.; Chen, G.; Kasai, Y.; Lim, E.W.C.; Hao, X.; Kaewpanha, M.; Abuliti, A.; Fushimi, C; Tsutsumi, A. *Appl. Catal., B*, 2012, 115, 159.
- [35] Jeong, D.W.; Subramanian, V.; Shim, J.O.; Jang, W.J.; Seo, Y.C.; Roh, H.S.; Gu, J.H.; Lim, Y.T. *Catalysis letter.* 2013, 143(5), 438.
- [36] Huang, J.; Schmidt, K.G.; Bian, Z. *Energies*, 2011,4(8), 1163.

2.3. Integrated Pyrolysis-Tar Decomposition of Polyethylene-Coal Blends over Low-Grade Iron Ores

(as presented in Open Chemistry 2018 – under review)

2.3.1. Introduction

Recently, the shortage of both high-grade coal as a carbonaceous reducing material as a primary reduction agent (i.e., coke) as well as high-grade iron ore as a raw material become the main problems in ironmaking industries. As reported in a modern blast furnace operation, to produce each ton of hot metal, it required coke and pulverized coal injection of 385 kg and 112 kg, respectively [1]. Around 1.6 ton of coking coal is needed to produce each ton of coke [2]. Since the coking coal (the high-grade coal) are now become limited availability, and higher cost, the utilization of alternate sources - instead of the low-grade coals (i.e., sub-bituminous or lignite coals)- waste plastic or wood biomass have gained much attention solving environmental concerns as well as reducing greenhouse gas emissions. Moreover, one study predicted that, until 2025, around 10 million tons annual of Indonesian mismanaged waste plastic pollute its ocean [3]. Indonesia, becoming the second most significant plastic waste contributor to the world, has seriously been taking the issue in the state of emergency regarding mismanaged waste plastic. As one approach, the combining utilization of low-grade coal and plastic waste is an attractive method to solve the issue. Since, most of the waste plastic component (up to 74 mass-%) is polyethylene (PE) [4], the utilization of PE as ironmaking fuel has already become attractive to be studied [5].

On the other hand, the depletion of high-grade iron ores is now highly driving some research works aiming for the effective utilization of low-grade ores (i.e., goethite) in the modern ironmaking industry. Goethite (FeOOH), however, due to its high

combined water content, will cause some permeability problems if it is directly charged into a blast furnace [6,7]. One researcher proposed a new process called the integrated pyrolysis–tar decomposition process to solve these problems simultaneously [8]. This process was designed to reduce pyrolytic tar product by decomposing it as deposited carbon over dehydrated low-grade iron ore, as well as to produce carbonized ore via chemical vapor infiltration (CVI). Similar reports mentioned a possible application using steelmaking slag [9] as well as utilizing various solid fuels (i.e., high-grade bituminous coal, low-grade lignite coal, and palm kernel shells) [10]. The decomposition of tar produced carbon that deposited within the iron ore pores, resulting in a partial reduction of the iron. Furthermore, the nanocracks suitable for carbon deposition were initiated and propagated during the dehydration. Interestingly, the carbon tar entering the nanocracks within ore plays a role as a potential reduction agent [11] with a significantly higher reduction reactivity due to the nanoscale contact between iron oxide and carbon [12].

To produce an ore with carbon deposited in the pore as its reduction agent, is a new challenge in these works, including blending PE-coal as its fuel. Although PE-coal co-pyrolysis has been already studied [13,14], yet none has investigated the effect of PE-coal co-pyrolysis that to be applied in the CVI process for ironmaking. At this time, the effect of the blending PE-coal on integrated co-pyrolysis–tar decomposition over low-grade iron ores were studied, observing the changes in product distributions at various blending ratios. The objective of this study is to find the synergetic effect of the blending ratio on PE-coal on its pyrolytic tar decomposition over low-grade iron ore.

2.3.2. Experimental Methods

2.3.2.1. Materials

As the carbonaceous materials, Indonesian Tanjung Enim coal (sub-bituminous coal) and polyethylene (PE) reagent were employed in this experiment with the proximate and ultimate analyses data are shown in Table 2.3.1. The particle size of coal and PE reagent were 125–355 μm (as crushed and sieved) and 1000 μm (as received), respectively.

Table 2.3.1 Proximate and ultimate analysis of Indonesian coal, woody biomass and PE reagent sample.

Sample	Proximate [mass%, air-dried basis]				Ultimate [mass%, dry ash free basis]				
	VM	Ash	FC	TM*	C	H	N	S	O**
Tanjung Enim sub-bituminous coal, coal	45.2	5.7	49.1	11.7	65.7	4.9	1.1	0.7	27.6
Polyethylene (PE) reagent	99.9	0.08	15.9	9.7	84.9	14.5	0.00	0.0	0.0

VM, Ash, FC, = Volatile matter, Ash content, Fixed carbon

TM* = Total moisture (% as received basis)

C, H, N, S = Carbon, Hydrogen, Nitrogen and Sulphur content

O** = Oxygen content was calculated by different

Two type of iron ores: Australian limonite and Indonesian laterite ores were utilized in this experiment with the properties shown in Table 2.3.2. The ores were dehydrated at 500 °C with a heating rate of 3 °C min⁻¹ and hold for 4 h under air atmospheric conditions. The dehydration treatments were needed to remove the combined water (CW) forming porous ore increasing the surface area. One report mentioned that the CW is completely removed at 500 °C, changing goethite (αFeOOH) to hematite ($\alpha\text{Fe}_2\text{O}_3$) [15]. The average pore volume, Brunauer–Emmett–Teller (BET) surface areas were measured using a gas adsorption measurement (Autosorb 6AG, Yuasa Ionics Co. Ltd., Japan).

Table 2.3.2 Brief properties of iron ores employed in this study.

Parameter	Limonite ore	Laterite ore
Total Fe content [mass%]	57	51
Ni content [mass%]	0	0.48
Combined water [mass%]	8.1	9.02
Particle size [mm]	0.95 - 2.0	0.95 - 2.0
Surface area [m ₂ g ⁻¹]	21 ^a	25 ^a
	71 ^b	87 ^b

^a As received; ^b After dehydration at 500 °C for 4 hr

2.3.2.2. Thermogravimetric analysis on PE-coal co-pyrolysis

Thermogravimetric (TG) curves of coal, polyethylene, and the blend at 50wt%-PE were obtained using Mettler Toledo TG DSC-1. Each sample of around 5 mg weight was put into a 150µl alumina crucible and heated under 100 NmL min⁻¹ of argon flow. The temperature was increased from 25 to 120 °C with a heating rate of 85 °C min⁻¹ then hold for 30 min at 120 °C to remove the moisture in the sample. Then, it heated up to 1000 °C with a constant heating rate of 75 °C min⁻¹ and hold for 10 min at 1000 °C to obtain the thermal decomposition behavior under an inert atmosphere. The inert (argon) gas flow then switched to 100 Nml min⁻¹ of airflow for 20 min to obtain the amount of remaining ash in the sample.

2.3.2.3. Integrated pyrolysis-tar decomposition of PE-coal blends

Figure 1 shows the scheme of experimental apparatus and condition on integrated pyrolysis-tar decomposition in a quartz reactor tube (the ID of 30 mm, the height of 550 mm) equipped with electrical furnace like the previous study [20]. The experiments were carried out with an N₂ flow of 250 mL min⁻¹ (STP) at atmospheric pressure. The carbonaceous materials were continuously charged to the reactor at a rate of 0.1 g min⁻¹ for 40 min after the reactor reached the constant set temperature. The temperatures were set for the pyrolysis at 700, 800, & 900 °C while the tar decomposition at 400, 500, & 600 °C as well selected in the similar study [16]. The pyrolytic char product was trapped in the upper part using a wire mesh (SUS304, 400 mesh), while the tar vapor and gases

were flowed directly through to the iron ore bed (3 g) for the tar decomposition process. Tars trapped in the thimble filter (110 °C) and the cold trap (-73 °C) were measured as heavy and light tar, respectively. The gases then measured using an online gas chromatograph (Agilent 3000, INFICON) to observe the concentrations of H₂, CH₄, CO, and CO₂. Char structures were visualized using scanning electron microscopy (SEM; JSM-7001FA, JEOL). The ore structure and composition were characterized using X-ray diffractometry (XRD; Miniflex, Rigaku). The carbon contents of the iron ores were measured using a CHN/O/S elemental analyzer (CE-440; EAI). Though this experiment, the effects of the PE-coal blending ratios on the product distributions of the integrated pyrolysis-tar decomposition were evaluated at 0, 25, 50, 75 and 100 wt%-PE.

2.3.3. Result and Discussions

2.3.3.1. Decomposition behavior of PE, coal, and PE-coal blending.

Figure 2 shows the TG result on pyrolysis of PE, TE Coal (coal), and the blending of PE-coal (50wt.% PE). TG experiments were set to observe the decomposition behavior of the samples including the moisture drying (at 120 °C for 30 min), thermal decomposition (pyrolysis at 120 - 1000 °C) and char combustion (at 1000 °C for 30 min under air flow). PE reagent has no moisture in it. PE reagent is rapidly decomposed at 400-500 °C leaving no char detected under this condition. In contrast, coal has inherent moisture that can be removed at 120 °C. Coal starts to be decomposed slightly at 220 °C, and rapidly at 400-500 °C as similar with PE. However, the coal was still being decomposed at 1000 °C leaving around 50wt% of char remains. It is probably due to the coal has more complex components to be decomposed rather than PE reagent, although, PE has more carbon content than coal. Meanwhile, the PE-coal blend 50wt%-PE

attributes both behaviors with a rapid decomposition at around 500 °C. Comparing with the reference curve of PE-coal at 50wt% PE, it was apparent that the experimental curve of the PE-coal blend is tightly fit to the reference curve, even the combustion behavior is also similar. In another way, it was confirmed that the PE decomposition temperature is identical to sub-bituminous coal decomposition.

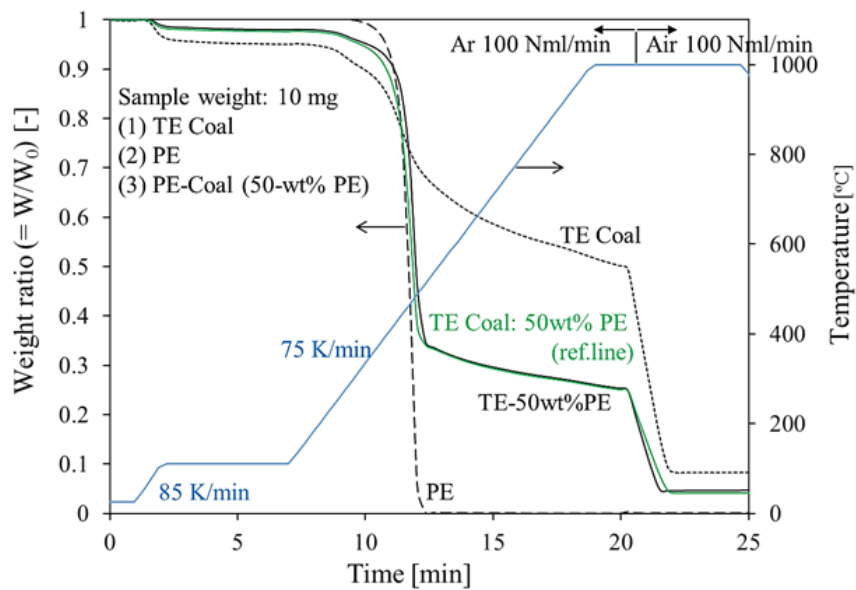
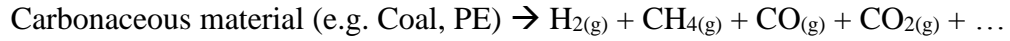


Figure 2.3.1 TG curves of coal (dotted line), PE (dashed line), and the blend at 50wt%-PE (solid line). TE Coal:50wt%PE (green ref. line) means the reference curve of PE-coal mixture at 50wt%-PE that is calculated by averaging the curves of PE and coal data.

2.3.3.2. The synergetic effect of integrated pyrolysis-tar decomposition of PE-coal blends

Reducing the tar products is the aim of the integrated pyrolysis–tar decomposition over low-grade iron ore. Tar is simultaneously converted to a deposited carbon in the pore of iron ore. Additionally, the production of higher carbon content carbonized ore is desired as well as the higher H₂, CO, and CH₄ contents in the tail gas. Figure 3 shows the product distribution carbon yields from PE-coal pyrolysis in three cases. Case a is the pyrolysis only. While, Case b1 and b2 are the integrated pyrolysis–tar decomposition

over porous limonite and laterite ores, respectively. It was apparent that in Case b1 and b2 (Figure 3(a)) the iron ore has a catalytic effect of cracking heavy tar producing light tar and gas. The reactions involved were tar reforming as in Eq. (2.3-1).



Gas reforming reaction also occurred during iron ore interaction increasing H₂ and CH₄ in case b1. Additional H₂ and CH₄ in Case b2 (Figure 3(b)) occur at the presence of Ni in the ore. Some researchers mentioned that Ni has a more powerful catalytic performance than iron oxide [18]. However, it suppresses the carbon deposition in iron ore.

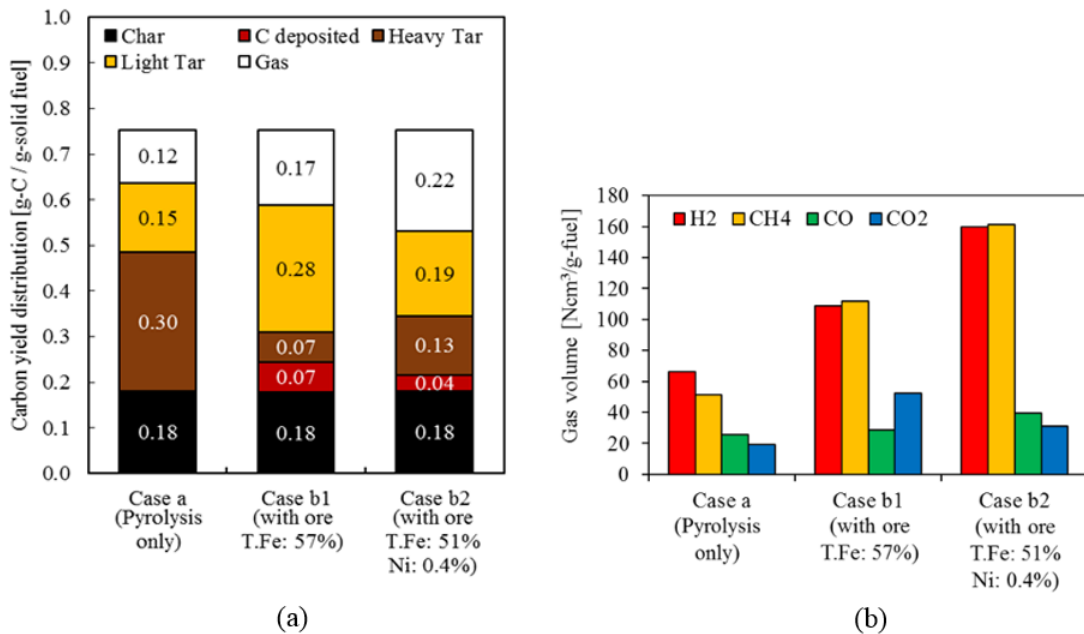


Figure 2.3.2 Carbon product distributions (a) and composition of product gas (b) from the integrated pyrolysis-tar decomposition over limonite and laterite ores. The experimental conditions were: fuel types, 50wt.%-PE; pyrolysis temp. = 800 °C; tar decomposition temp. = 500 °C; reaction time = 40 min; Case a: pyrolysis only; Case b1 & b2: pyrolysis-tar decomposition over limonite & laterite ores, respectively.

Effects of PE-coal co-pyrolysis on the product distribution carbon yields and gas compositions are shown in Figure 4. The total carbon yield increase at the higher blending

ratio is due to PE has more carbon content than coal. Blending PE-coal could suppress heavy tar production and increase light tar and gas. CH₄ is increased at the higher blending ratio. However, H₂ is found decreasing in the blending ratio at higher than 50wt%-PE. One report mentioned that H₂ might be consumed by tar hydrocracking process [19,20]. CO was decreased at higher blending ratio due to the lack of oxygen content in the fuel blends. Meanwhile, CO₂ tended to be higher than CO as the result of iron oxide reacting with CO as well ore reduction occurs.

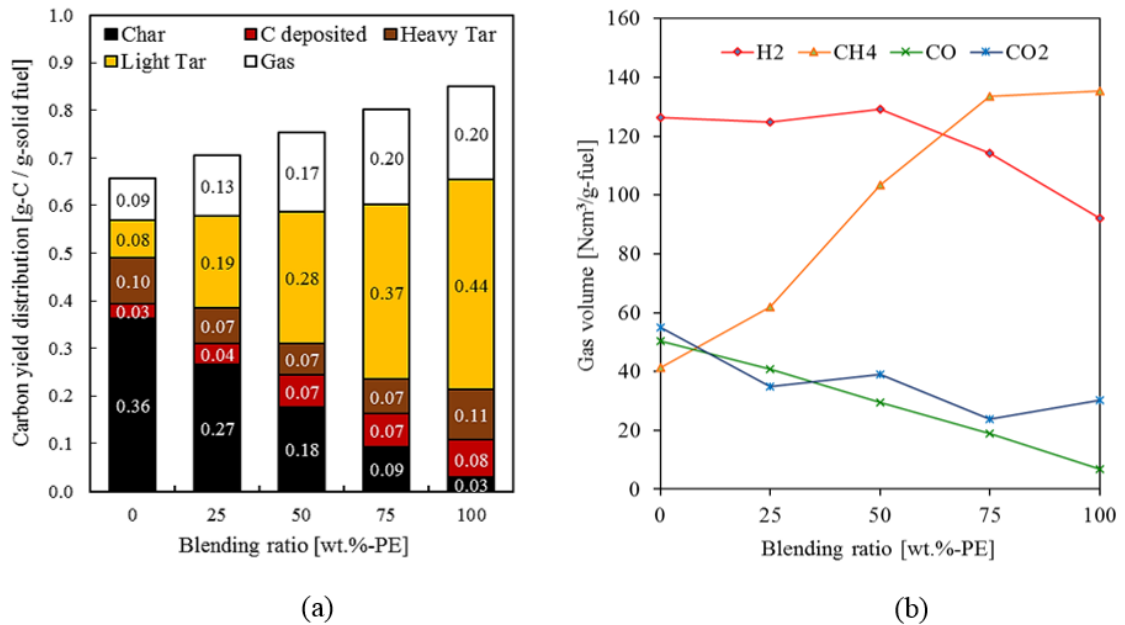


Figure 2.3.3 Carbon product distributions (a) and composition of product gas (b) from the integrated pyrolysis-tar decomposition over limonite ore at different blending ratios. The experimental conditions were: fuel types, TE coal & PE blends; ore type: dehydrated limonite ore; pyrolysis temperature = 800 oC; tar decomposition temperature = 500 oC; and reaction time = 40 min.

To clarify the effect of PE-coal blend for each pyrolytic product, the linear reference line the synergetic effects can be estimated by the deviation of each observed datum from the reference line, as well expressed [20]:

$$\delta_{i,j} = \frac{y_{i,j} - y_{i,j}^{ref}}{y_{i,j}^{ref}} \quad (2.3-2)$$

where $\delta_{i,j}$ is the deviation value (the synergetic effect) at different blending ratios, $y_{i,j}$ is the observed data of each pyrolytic product, $y_{i,j}^{ref}$ is the reference line calculated using $\left(= \frac{y_{100,j} + y_{(100-i),j}}{100} \right)$, i is the experimental PE-coal blending ratio [wt.%-PE], and j is the product of pyrolysis (e.g., chars, deposited, carbon in ore, heavy tar, light tar, and gas). The non-zero value of $\delta_{i,j}$ means that the synergetic effect occurs in PE-coal blends on pyrolysis. The synergetic effects were clearly found on the PE-coal blend in the integrated pyrolysis-tar decomposition over limonite ore (Figure 5). In the integrated pyrolysis-tar decomposition, synergetic effects of coal-polyethylene blend contribute in significantly decreasing heavy tar, slightly decreasing char, increasing the carbon deposition, light tar, and gas products. Overall, a significant synergetic effect occurred at the blending ratio of 50wt%-PE.

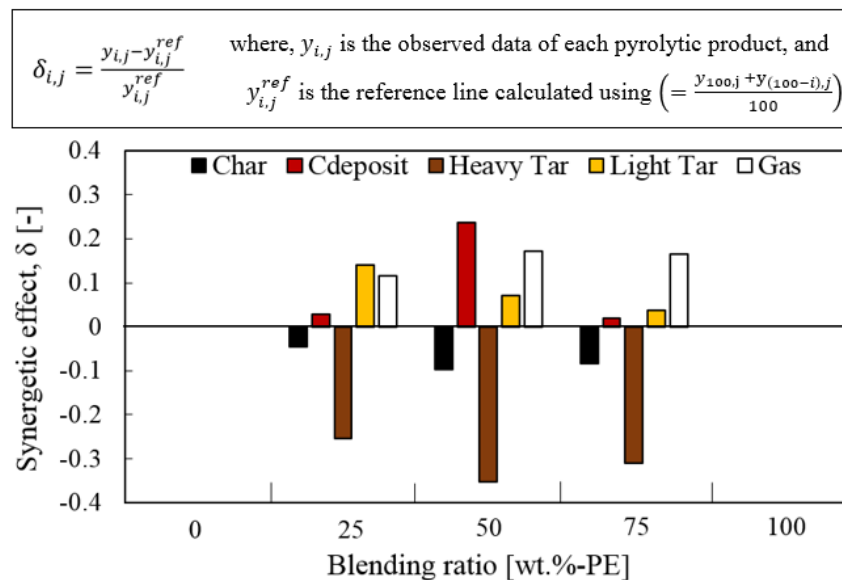


Figure 2.3.4 The synergetic effect of PE-coal on integrated pyrolysis-tar decomposition over limonite ore at different blending ratios. The experimental conditions were: fuel types, TE coal & PE blends; ore type: dehydrated limonite ore; pyrolysis temperature = 800 oC; tar decomposition temperature = 500 oC; and

reaction time = 40 min. i denotes the experimental PE-coal blending ratio [wt.%-PE], and j is the product of pyrolysis (e.g., chars, deposited, carbon in ore, heavy tar, light tar, and gas).

SEM observations on char particles confirmed the effect of PE-coal co-pyrolysis on char product (Figure 6). Pyrolysis of PE produced small particle chars (at 100w%PE), while coal chars (0 – 75wt%PE) remained still maintaining their original shapes. So, it could be easily distinguished between them in the char mixture at any blending ratios. Coal chars from coal only (0wt%PE) seem only had small cracks and pores on its surface. Similar like biomass-coal blending, on the blending with PE, more cracks and pores were formed on the coal char surface. The morphology of coal char in the blend then became a loose-packed, more porous structure at the higher blending ratios (25-75wt%PE). The most significant cracks were observed on the coal char surface at 75wt%PE. The similar cracking phenomena were also found on pyrolysis at elevated temperature. It is probably due to volatile matter in the polyethylene promoting more coal particle decomposition.

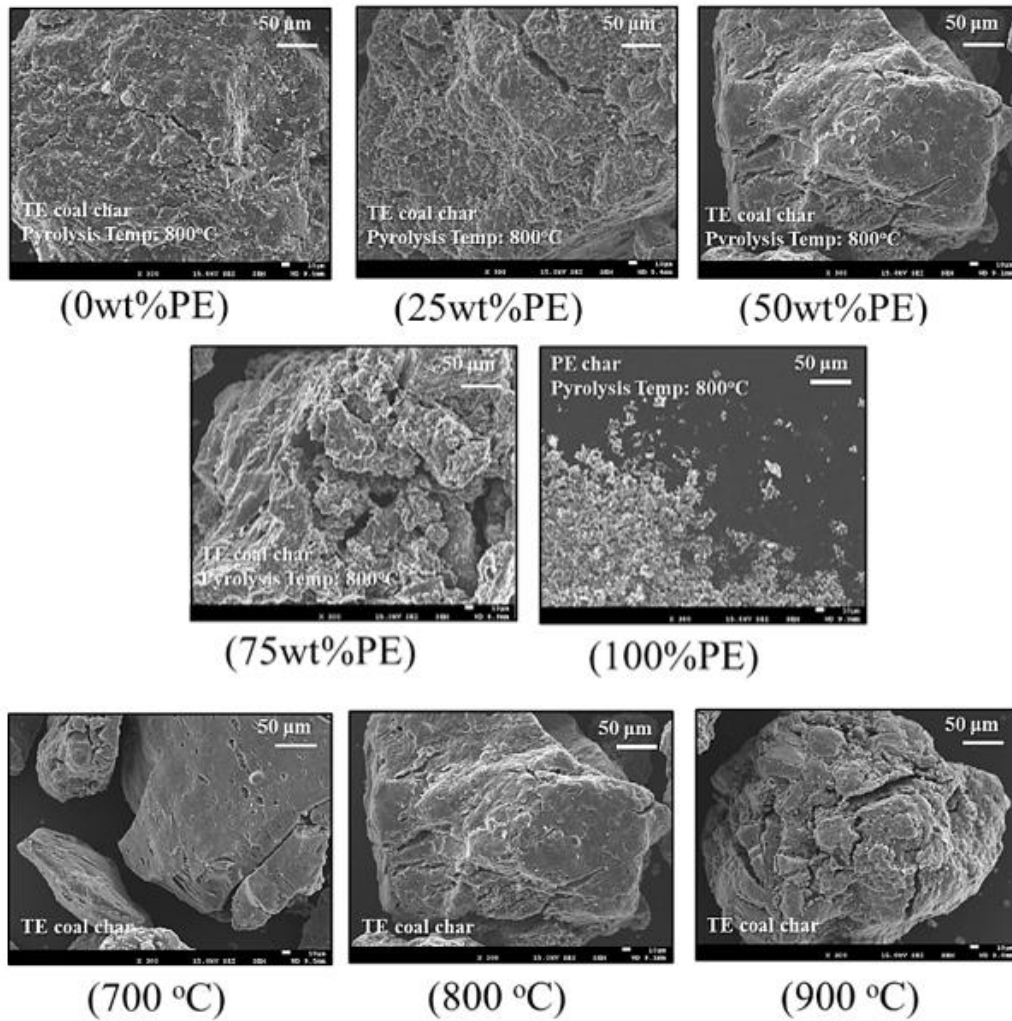


Figure 2.3.5 SEM images of char products on PE-coal co-pyrolysis at different blending ratios and pyrolysis temperatures.

2.3.3.3. Carbon depositions and structures of iron ore from tar decomposition reaction

The carbon content of iron ores after tar decomposition reaction as influenced by fuel blending, pyrolysis temperatures, and tar decomposition/CVI temperatures were shown in Figure 7. The deposited carbon content, as the product of heavy tar decomposition, increase when the PE-coal blend was introduced to integrated pyrolysis-tar decomposition (Figure 7(a)). Meanwhile, under the effect of pyrolysis temperature (Figure 7(b)), carbon content decrease at a higher temperature. Higher temperature pyrolysis generates more significant amounts of volatile matter (tar and gases). However,

the higher pyrolysis temperature is also not preferable, because the produced heavy tar is predominantly decomposed in the pyrolytic zone rather than decomposed in the surface of iron ore. On the other hand, the higher temperature of tar decomposition (Figure 7(c)) promotes a higher kinetic of tar produces more carbon deposited into porous iron ore. However, since the small pores in iron ore will disappear at a higher temperature (>500 °C). It will limit the amount of carbon deposited into the pore of iron ores. The previous researcher already mentioned that the pyrolysis and tar decomposition were both highly sensitive to temperature and exhibited different behaviors during carbon deposition [16]. In this experiment, the optimum temperatures for pyrolysis and tar decomposition should be determined to maximize the carbon deposition. The maximum carbon deposit (4.4 mass%) was obtained at the blending of 50wt%-PE, pyrolysis temperature of 800 °C, and CVI reaction temperature of 600 °C. However, the carbon content in iron ore is still far from the stoichiometric expectation which is up to 18 mass%-C required to reduce Fe₂O₃ to metallic-Fe. It was also suggested that around 24 mass%-C is needed to promote a faster reduction process [22].

XRD analysis and SEM observation on ores (as shown in Figure 8) were performed to observe the iron ore structure changes after the dehydration and after tar decomposition reactions.

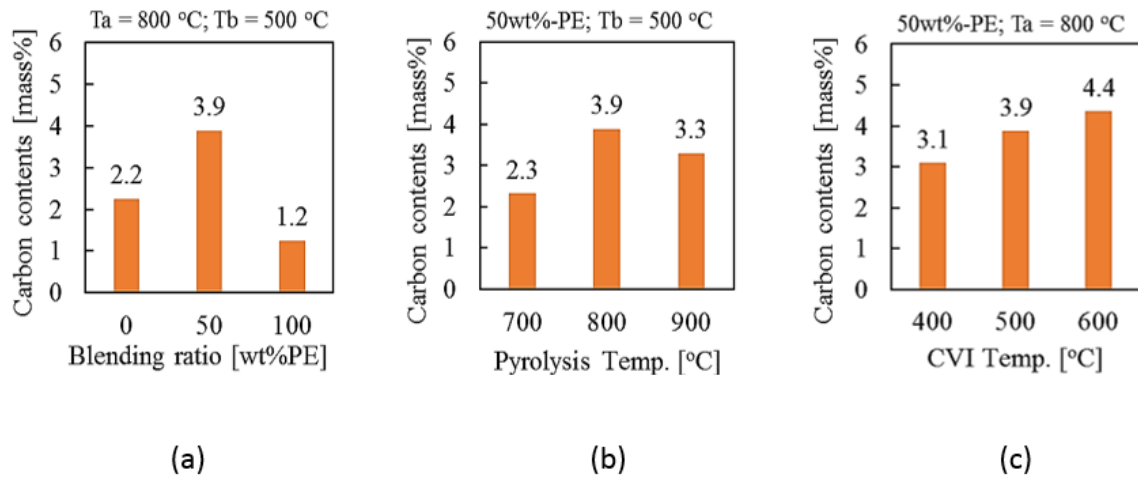


Figure 2.3.6 The carbon content of ores after tar decomposition reactions. (a), (b), and (c) correspond to the effect of PE-coal blending, pyrolysis temperatures, and tar decomposition/CVI temperatures, respectively. (Remarks: Ta = Pyrolysis temperature; Tb = Tar decomposition/CVI temperature).

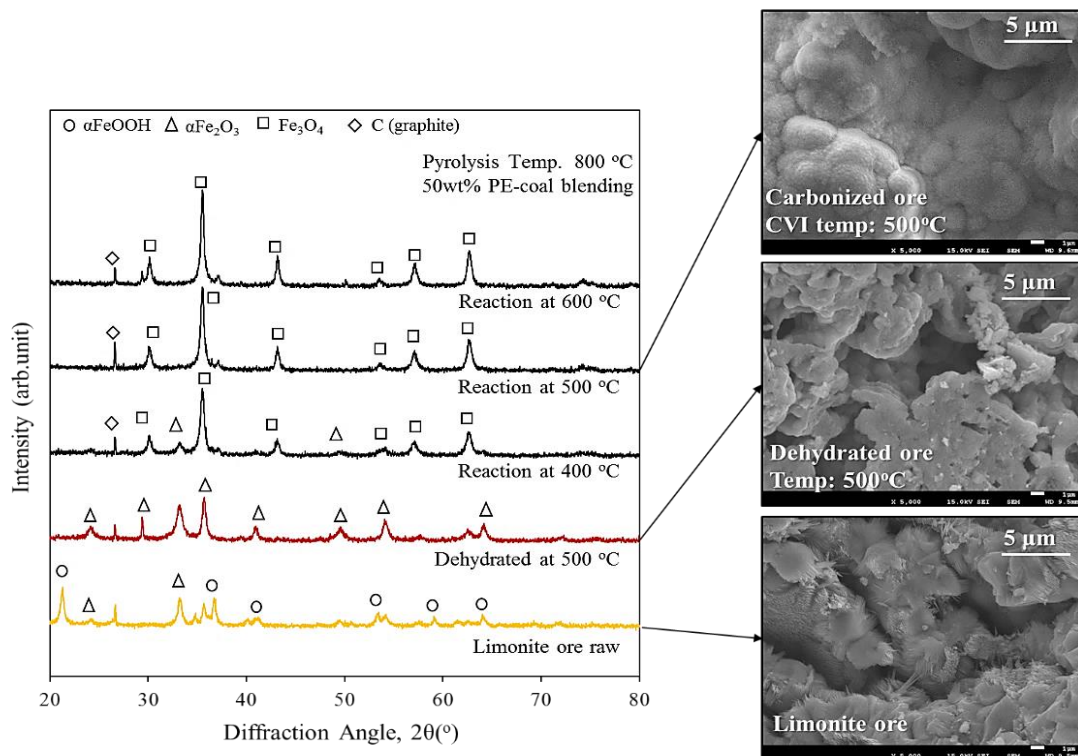
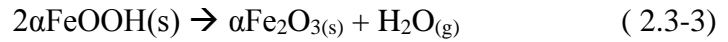


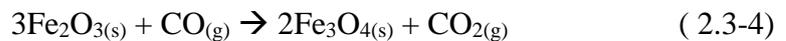
Figure 2.3.7 XRD patterns of limonite ores at the raw condition, after dehydration at 500 °C, and after 40 min reaction on integrated pyrolysis-tar decomposition at 400, 500, & 600 °C. SEM images of the ores at raw, dehydrated, and after reaction at 500 °C were also provided.

As received, the limonite ore has α FeOOH (goethite) peaks on XRD pattern as well correspond with the needle-like structure observed using SEM. After the

dehydration at 500 °C, there is no FeOOH peak on XRD patterns neither the needle-like structure in the SEM image. Thus, the dehydration might be completed at this temperature. One report mentioned that along with releasing the CW; the ore structure changes from αFeOOH (goethite) to $\alpha\text{Fe}_2\text{O}_3$ (hematite) with the following reaction [21]:



During the tar decomposition reaction, the ore was reduced to magnetite (Fe_3O_4). Hematite was fully reduced to magnetite during tar decomposition at higher than 400 °C. Graphite carbon was deposited on the surface of iron ore during tar decomposition/CVI process. This reduction result agreed to another report [20] involving the reactions of hematite component in the iron ore with CO and H_2 [23] during tar decomposition process such as indirect reductions:



2.3.4. Summary

Waste plastic (i.e., PE) is attractive as an alternative carbon resource for ironmaking through CVI method. PE decomposition is like the subbituminous coal decomposition. Iron ore has a catalytic effect on cracking heavy tar producing light tar and gas. Gas reforming reaction also occurs during iron ore interaction. The presence of Ni content in iron ore performs as a reforming catalyst in producing more H_2 in the gas stream. The higher blending ratio of PE-coal suppresses heavy tar production and increase light tar and gas. The higher PE content in the blending can increase CH_4 . The blending at 50wt% -PE was found optimum in lowering heavy tar product, increasing gas amount, and increasing carbon deposition. The more porous chars were obtained at, the higher PE blending as well as increasing the pyrolysis temperature. Hematite is reduced

to magnetite during tar decomposition at higher than 400 °C with contains carbon deposit. The highest carbon deposit (4.4 mass%-C) was obtained at the blending of 50wt%-PE, pyrolysis temperature of 800 °C, and CVI reaction temperature of 600 °C. Further searches are still needed to increase the amount of deposited carbon into porous iron ore to proceed iron ore reduction to metallic-Fe.

References

- [1] Suzuki, K., Hayashi, K., Kuribara, K., Nakagaki, T., Kasahara, S., Quantitative evaluation of CO₂ emission reduction of active carbon recycling energy system for ironmaking by modeling with aspen plus, *ISIJ Int.*, 2015, 55(2), 340-347.
- [2] International Energy Agency. World energy outlook. Organization for Economic Co-operation and Development, 2007, https://www.iea.org/publications/freepublications/publication/WEO_2007.pdf.
- [3] Jambeck, J.R., Geyer, R., Wilcox, C., Siegler, T.R., Perryman, M., Andrady, A., Narayan, R., Law, K.L., Plastic waste inputs from land into the ocean. *Science*, 2015, 347(6223), 768-771.
- [4] Areeprasert, C., Asingsamanunt, J., Srisawat, S., Kaharn, J., Inseemeeesak, B., Phasee, P., Khaobang, C., Siwakosit, W., Chiemchaisri, C., Municipal plastic waste composition study at transfer station of bangkok and possibility of its energy recovery by pyrolysis. *Energy Procedia*, 2017, 107, 222-226.
- [5] Murakami, T., Akiyama, T., Kasai, E., Reduction behavior of hematite composite containing polyethylene and graphite with different structures with increasing temperature. *ISIJ Int.*, 2009, 49(6), 809-814.
- [6] Akiyama, T., Ohta, H., Takahashi, R., Waseda, Y., Yagi, J.I., Measurement and modeling of thermal conductivity for dense iron oxide and porous iron ore agglomerates in stepwise reduction. *ISIJ Int.*, 1992, 32(7), 829-837.
- [7] Purwanto, H., Shimada, T., Takahashi, R., Yagi, J.I., Lowering of grinding energy and enhancement of agglomerate strength by dehydration of Indonesian laterite ore. *ISIJ Int.*, 2002, 42(3), 243-247.
- [8] Hata, Y., Purwanto, H., Hosokai, S., Hayashi, J.I., Kashiwaya, Y., Akiyama, T., Biotar ironmaking using wooden biomass and nanoporous iron ore. *Energy Fuels*, 2009, 23(2), 1128-1131.

- [9] Rozhan, A.N., Cahyono, R.B., Yasuda, N., Nomura, T., Hosokai, S., Akiyama, T., Carbon deposition of biotar from pine sawdust by chemical vapor infiltration on steelmaking slag as a supplementary fuel in steelworks. *Energy Fuels*, 2012, 26(6), 3196-3200.
- [10] Hosokai, S., Matsui, K., Okinaka, N., Ohno, K.I., Shimizu, M., Akiyama, T., Kinetic study on the reduction reaction of biomass-tar-infiltrated iron ore. *Energy Fuels*, 2012, 26(12), 7274-7279.
- [11] Cahyono, R.B., Rozhan, A.N., Yasuda, N., Nomura, T., Purwanto, H., Akiyama, T., Carbon deposition using various solid fuels for ironmaking applications. *Energy & Fuels*, 2013, 27(5), 2687-2692.
- [12] Rozhan, A.N., Cahyono, R.B., Yasuda, N., Nomura, T., Hosokai, S., Akiyama, T., Carbon deposition of biotar from pine sawdust by chemical vapor infiltration on steelmaking slag as a supplementary fuel in steelworks. *Energy & Fuels*, 2012, 26(6), 3196-3200.
- [13] Qian, C., Zhou, M., Wei, J., Ye, P., Yang, X., Pyrolysis and co-pyrolysis of lignite and plastic. *Int. J. Min. Sci. Technol.*, 2014, 24(1), 137-141.
- [14] Saha, G.R., Das, T., Handique, P., Kalita, D., Saikia, B.K., Copyrolysis of low-grade indian coal and waste plastics: future prospects of waste plastic as a source of fuel. *Energy Fuels*, 2018, 32(2), 2421-2431.
- [15] Saito, G., Nomura, T., Sakaguchi, N., Akiyama, T., Optimization of the dehydration temperature of goethite to control pore morphology. *ISIJ Int.*, 2016, 56(9), 1598-1605.
- [16] Cahyono, R.B., Yasuda, N., Nomura, T., Akiyama, T., Optimum temperatures for carbon deposition during integrated coal pyrolysis–tar decomposition over low-grade iron ore for ironmaking applications. *Fuel Process. Technol.*, 2014, 119, 272-277.
- [17] Xu, M., Brown, R.C., Norton, G., Smeenk, J., Comparison of a solvent-free tar quantification method to the international energy agency's tar measurement protocol. *Energy fuels*, 2005, 19(6), 2509-2513.
- [18] Abe, K., Kurniawan, A., Nomura, T., Akiyama, T., Effects of reduction on the catalytic performance of limonite ore. *J Energy Chem.*, 2017. In press. <https://doi.org/10.1016/j.jechem.2017.09.032>
- [19] Huang, J., Schmidt, K.G., Bian, Z., Removal and conversion of tar in syngas from woody biomass gasification for power utilization using catalytic hydrocracking. *Energies*, 2011, 4(8), 1163-1177.
- [20] Kurniawan, A., Abe, K., Nomura, T., Akiyama, T., Integrated pyrolysis–tar decomposition over low-grade iron ore for ironmaking applications: effects of coal–biomass fuel blending. *Energy & Fuels*, 2018, 32(1), 396-405.

- [21] Akiyama, T., Takahashi, R., Yagi, J.I., Heat transfer simulation on drying processes of nonfired pellets containing combined water in the moving bed reactor. *ISIJ Int.*, 1991, 31(1), 24-31.
- [22] Abe, K., Kurniawan, A., Ohashi, K., Nomura, T., Akiyama, T., Ultrafast iron-making method: carbon combustion synthesis from carbon-infiltrated goethite ore. *ACS Omega*, 2018, 3(6), 6151-6157.
- [23] Kurniawan, A., Abe, K., Ohashi, K., Nomura, T., Akiyama, T., Reduction of mild-dehydrated, low-grade iron ore by ethanol. *Fuel Processing Technology*, 2018, 178, 156-165.

2.4. Conclusions

This chapter concludes several aspects to intensify in the previously proposed CVI ironmaking:

1. Production of nanoporous hematite from goethite is time-consuming due to the removal of combined water is slow under atmospheric air condition. Vacuum dehydration ($P = 1$ kPa) of goethite successfully removed the CW in 1 hour at 300 °C generating similar porous hematite with 2-4 nm pore-sized, surface area, and total pore volume as found in the previous 24 h under atmospheric air condition. Vacuum dehydration is attractive to make it faster and suitable in an actual application.
2. Introducing coal-biomass co-pyrolysis to the integrated pyrolysis–tar decomposition process was attractive since coal-biomass co-pyrolysis has a synergetic effect to enhance overall pyrolysis efficiency in increasing carbon content in CVI. The highest CVI carbon content (4.70 wt%) was obtained using BBR-25%. This is due to increased reacted heavy tar contributing to increasing the deposited carbon ratio. In other words, the co-pyrolysis of coal blending with 25 wt% of biomass (which has a lower carbon amount) could produce higher carbon content CVI ore.
3. Waste plastic (i.e., PE) is also attractive as an alternative carbon resource for ironmaking through CVI method. PE decomposition is like the subbituminous coal

decomposition. Iron ore has a catalytic effect on cracking heavy tar producing light tar and gas. The higher blending ratio of PE-coal suppresses heavy tar production and increase light tar and gas. The higher PE content in the blending can increase CH₄. The blending at 50wt%-PE was found optimum in lowering heavy tar product, increasing gas amount, and increasing carbon deposition.

However, the deposited carbon content was not enough for the perfect reduction of iron ore as depicted in Figure 2.4.1 for comparison with the previous study to produced CVI ore or carbon composite iron ore.

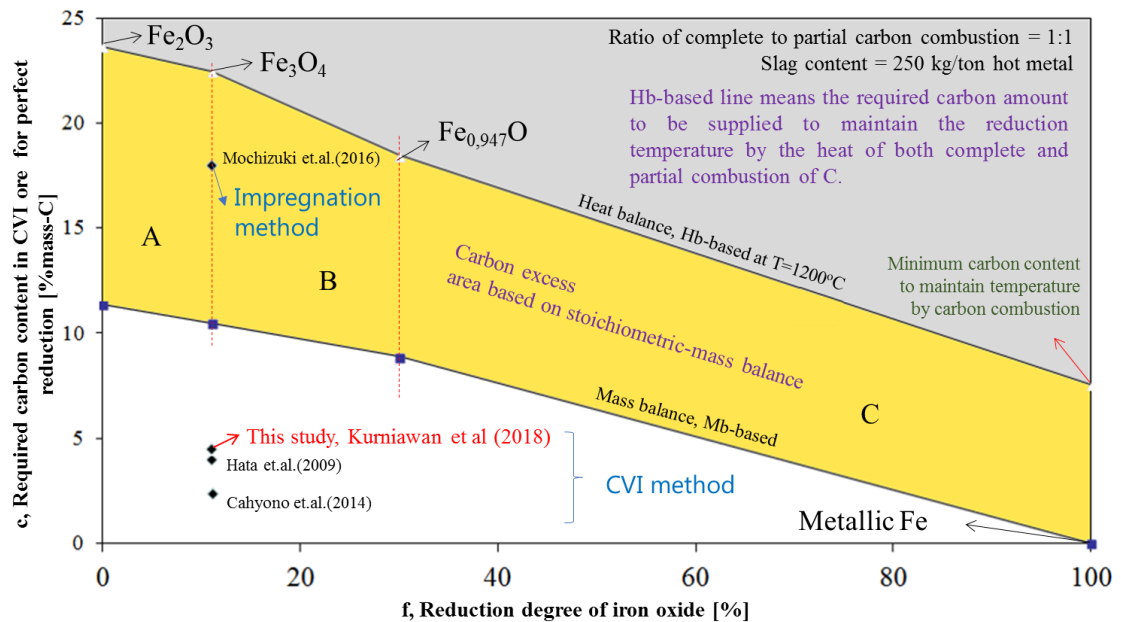


Figure 2.4.1 Simulated required carbon content in CVI ore for perfect iron reduction with some footprints of producing carbon composite ore from nanoporous iron ore.

Reference for Figure 2.4.1:

- [1] Hata, Y., Purwanto, H., Hosokai, S., Hayashi, J.I., Kashiwaya, Y. and Akiyama, T., 2009. Biotar ironmaking using wooden biomass and nanoporous iron ore. *Energy & Fuels*, 23(2), pp.1128-1131.
- [2] Cahyono, R.B., Yasuda, N., Nomura, T. and Akiyama, T., 2014. Optimum temperatures for carbon deposition during integrated coal pyrolysis–tar decomposition over low-grade iron ore for ironmaking applications. *Fuel processing technology*, 119, pp.272-277.
- [3] Mochizuki, Y., Nishio, M., Ma, J., Tsubouchi, N. and Akiyama, T., 2016. Preparation of Carbon-Containing Iron Ore with Enhanced Crushing Strength from Limonite by Impregnation and Vapor Deposition of Tar Recovered from Coke Oven Gas. *Energy & Fuels*, 30(8), pp.6233-6239.
- [4] Kurniawan, A., Abe, K., Nomura, T. and Akiyama, T., 2018. Integrated Pyrolysis–Tar Decomposition over Low-Grade Iron Ore for Ironmaking Applications: Effects of Coal–Biomass Fuel Blending. *Energy & Fuels*, 32(1), pp.396-405.

CHAPTER III

REDUCTION BEHAVIOR OF POROUS HEMATITE ORE OVER ETHANOL DECOMPOSITION

3.1. Introduction

Recently, numerous methods have been proposed to reduce carbon dioxide emissions in the ironmaking process. The Paris Agreement (2015) requires the implementation of several actions on climate change mitigation by reducing greenhouse gas emissions [1]. One of the most challenging problems for reducing carbon dioxide emissions is to replace non-renewable carbonaceous materials such as coke as the reducing agent in ironmaking. Another difficult challenge is to improve the reactivity of iron ore and the reducing agent, resulting in the opportunity to perform faster and lower-temperature reduction processes. In the case of blast furnaces, the temperature of the thermal reserve zone, where the temperature is 1000 °C, is determined by the reaction rate of coke gasification by carbon dioxide; this prevents the effective use of the reducing agent [2]. Thus, one of the most effective solutions to improve reactivity is to place composites of the iron ore and carbon in close contact with each other [3–6].

On the other hand, to overcome the abundance trend of low-grade iron ore (i.e., goethite) over hematite/magnetite ore, an innovative solution is required. A new ironmaking method known as chemical vapor infiltration (CVI) ironmaking using a renewable carbonaceous material such as biomass together with nanoporous hematite ore was proposed [7]. This process requires three steps to reduce iron ore. The first step is the dehydration process of the combined water (CW) contained in the goethite in high amounts, e.g., 8.8 mass% in lower temperature (so-called mildly-dehydration), to change

the goethite ore structure to nanoporous hematite ore [8]. The second step is the carbonization process of the porous iron ore to invoke the simultaneous mechanisms of pyrolysis, catalytic tar decomposition, and carbon deposition through CVI in one integrated process [9–13]. The deposited carbon structure, detected as amorphous carbon, provides higher reactivity for the reduction process [14]. Infiltration of carbon into the ore pores improves not only the reactivity of the iron ore but also its mechanical strength [15]. During tar decomposition and carbon deposition in iron ore, the iron ore structure changes from hematite to magnetite (or even wüstite), meaning the reduction occurs; that is called pre-reduction processes [16]. However, because pre-reduction produces mainly the magnetite structure, the reduction degree (RD) is only approximately 11% [17]. Thus, it requires a third step, which is the reduction process to reach metallic Fe (RD 100%) [18]. Narrowing the large gap of RD from 11% to 100% by increasing the RD from the pre-reduction process has aroused much research interest. By focusing on the improvement of the pre-reduction mechanism, CVI technology might become more attractively applicable.

One approach is to introduce a small-molecule carbonaceous material such as ethanol as the reducing agent in porous hematite ore. As a biomass derivative considered carbon-neutral in contributing to CO₂ emission, bioethanol is widely applicable as a fuel with a simple production process. It might be attractive as a reducing agent in ironmaking to solve the depletion of carbonaceous reducing agents in ironmaking as well [19]. Yet, few researchers have tried to explore the merits of ethanol use in ironmaking, because the ethanol availability is bound by the limitation of land use for ethanol crops and the lower yield of ethanol fermentation technologies [20]. However, ethanol yield technologies are still emerging, and gas fermentation has become attractive [21]. Recently, some projects

have started to utilize the tail gas consisting of H₂-CO-CO₂ and waste heat from the steelmaking process to produce ethanol via gas fermentation by microorganisms [22,23]. Those emerging technologies are promising approaches to ensure the availability of ethanol. Therefore, ethanol-assisted ironmaking might become an attractive option in the future.

Chapter 2 discusses the simultaneous decomposition of ethanol over porous iron ore along with the reduction of the porous iron ore, in which the effects of decomposition temperatures, ethanol flowrates, and charging temperatures on the reduction were mainly investigated by temperature-programmed reaction experiments. Different iron ores with different CW content were also investigated. Combined with the utilization of nanoporous iron ore, this approach would enhance the merits of co-utilization of low-grade iron ore with a renewable reducing agent.

3.2. Materials and experimental methods

3.2.1. Preparation of porous ore samples

Different iron ores: Australian goethite (GE) ore, Western Australian (WA) ore, and Brazilian Riodoce (RC) ore with different CW contents were employed. Porous hematite (Fe₂O₃) reagent produced from goethite (FeOOH) reagent was also used as a reference. Table 1 shows the compositions and pore structure of the iron oxide and ores used in the experiments. The original ore was sieved so that a particle size ranged from 1 to 2 mm. The reagent and ores were first mildly dehydrated at 300 °C with a heating rate of 3 °C min⁻¹ and kept for 24 h under air atmosphere by a method like that in [8]. The heating profile of mild-dehydration of the iron ore materials is shown in Figure 3.1. This heat treatment makes the ore porous because CW is removed from the ore producing

hematite structure with many nanopores. In order to confirm this effect, the surface area and pore volume of the ores were analyzed using N₂ adsorption equipment (Autosorb 6AG, Yuasa Ionics) before and after, as shown in Table 2.

Table 3.2.1 Properties of iron ore samples.

Sample	Particle size	Total Fe [mass%]	Combined water [mass%]
FeOOH reagent	1 μm	62	9.7
GE ore (Australian iron ore)	1–2 mm	57	8.6
WA ore (Australian iron ore)	1–2 mm	61	5.1
RC ore (Brazilian iron ore)	1–2 mm	65	0.77

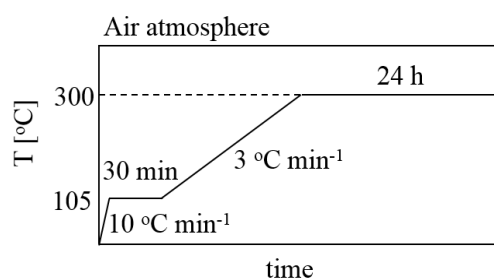


Figure 3.2.1 Temperature profile of the furnace for mild-dehydration of iron ores; FeOOH changes to slit-shaped nano-porous Fe₂O₃.

Table 3.2.2 Brunauer-Emmett-Teller (BET) surface area and total pore volume of different iron ores before and after mild-dehydration treatments.

Sample	BET surface area [m ² /g]		Total pore volume [cm ³ /g]	
	Original ^a	Dehydrated ^b	Original ^a	Dehydrated ^b
FeOOH reagent	15	110	0.1301	0.1760
GE ore	13	92	0.0409	0.1058
WA ore	12	79	0.0620	0.1213
RC ore	2	11	0.0081	0.0211

a = as received, b = after 24 h dehydration at 300 °C under air atmosphere

SAA analyzer condition: Adsorbate N₂, mol.wt = 28.0134 g/mol, cross-sec area = 16.2 Å²/molec., non-ideality = 6.580×10⁻⁰⁵, P/Po toler. = 2, outgas temp.= 120 °C, outgas time = 1.0 h, bath temp. = 77.35 K.

3.2.2. Ethanol decomposition over porous iron ores

Figure 3.2 shows the experimental apparatus scheme for the temperature programmed reaction (TPR) of the ethanol decomposition process. Approximately 0.3 g

of iron ore was placed as a packed bed (7 mm of bed length) in a quartz tube reactor (6 mm of ID, 554 mm of length). Quartz wool of approximately 0.04 g was also put as bed support (8 mm of support length). The detailed information of the reactor set was reported in a similar study [24]. Argon at 100 Nml min⁻¹ was introduced to keep the atmosphere in an inert condition. The reactor was heated in a vertical infrared (IR) furnace from room temperature to different final temperatures (400–900 °C) at a heating rate of 10 °C min⁻¹. A thermocouple for the programmed temperature was placed inside the quartz tube below the bed support. A preliminary experiment had already conducted to confirm that there is no temperature disparity at the different axial position in the reaction.

Ethanol (C₂H₅OH) reagent (99.5 vol%) at a liquid flow rate of 0.04 ml min⁻¹ was introduced using a peristaltic injection pump into the ore bed in a quartz tube starting from 100 °C until the final temperature was reached. The starting temperature was chosen to ensure that the ethanol was vaporized (the boiling point of ethanol is 78 °C) before contacting the iron ore surface. The upper quartz wool was placed as an impingement baffle to prevent unvaporized ethanol liquid drops from propagating through the iron ore bed.

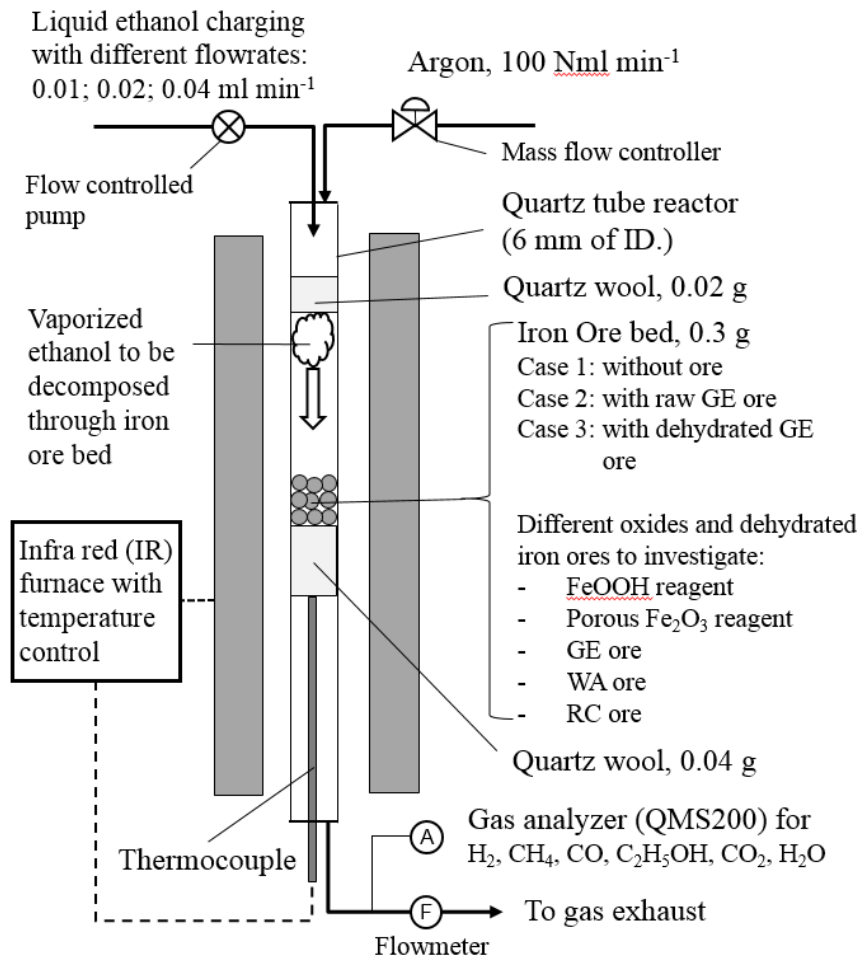


Figure 3.2.2 Experimental apparatus scheme for ethanol charging to iron ore beds

The gas concentrations of the outlet gases, such as C₂H₅OH, H₂, CH₄, CO, CO₂, and H₂O were analyzed online using quadruple mass spectroscopy (QMS200, Pfeiffer). The evolution of total outlet gas flowrate was also monitored by a gas flowmeter. The molar flowrates of each gas were calculated using

$$\dot{n}_i = f_T \frac{C_i}{100} \frac{10^6}{24.0548} \quad (3.2-1)$$

where \dot{n}_i is the calculated molar flowrate of each components i (i.e., C₂H₅OH, H₂, CH₄, CO, CO₂, H₂O) [μmol min⁻¹]. C_i is the gas concentration of each component i measured by QMS200 [mol%]. f_T is the total volumetric flowrate in the reactor outlet

gas [Nml min^{-1}]. The factor of $\left(\frac{10^6}{24.0548}\right)$ is the conversion factor of gas volumetric flowrate to molar flowrates at NTP-Normal Temperature and Pressure - condition [$\mu\text{mol Nml}^{-1}$]. The NTP condition is defined as air at 20°C (293.15 K) and 1 atm. Figure 3.3 shows a schematic of the heating and ethanol charging scenarios during the reaction.

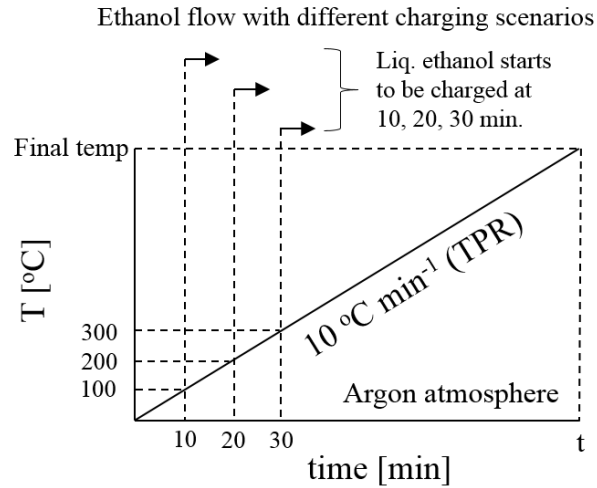


Figure 3.2.3 Temperature profile of the furnace in ethanol charging.

3.2.3. Sample characterizations

Characteristics of the ore structures and compositions before and after the reactions were analyzed using X-ray diffractometry (XRD; Miniflex, Rigaku). The carbon content in the iron ore was calculated by the weight change of the iron ore after reduction in ethanol decomposition and after combustion at 1000°C for 30 min under 500 ml min^{-1} of air flow. Considering the reoxidation of reduced iron ore to hematite, the carbon content calculation as expressed

$$X_C = \left(1 - \frac{w_{sb}}{w_{sa}} \left(1 - \frac{23.99}{55.85} \frac{X_{FeO} X_{RDa}}{(1 - X_{CW})} \right) \right) \times 100\% \quad (3.2-2)$$

where X_C is the fraction of carbon content in the sample after reduction in ethanol decomposition [mass%]. w_{sa} and w_{sb} are the sample weight after reduction in ethanol

decomposition and after combustion in air flow, respectively [mg]. The factor of $\left(\frac{23.99}{55.85}\right)$ corresponds to the ratio of the stoichiometric mass equivalent of oxygen to Fe in Fe_2O_3 structure (calculated as $\text{FeO}_{1.5}$). X_{FeO} and X_{CW} are the mass fraction of total Fe and the combined water (CW) content in raw material, respectively [-]. X_{RDa} is the mass fraction of the reduction degree (RD) of the sample after a reduction in ethanol decomposition [-]. The reduction degree (RD) of each sample was then calculated using

$$RD = \frac{\text{mass of removed oxygen}}{\text{mass of removable oxygen}} \times 100\% \quad (3.2-3)$$

However, it was difficult to evaluate the exact amount of removed and removable oxygen because the presence of gangue materials such as SiO_2 , Al_2O_3 , and other oxides might be different within the ore samples. The RD of each sample was then calculated on the basis of the composition of iron oxides in the sample using

$$RD = \sum x_i RD_i \quad (3.2-4)$$

where x_i is the mass fraction of iron oxide component i ($i = \text{Fe}_2\text{O}_3, \text{Fe}_3\text{O}_4, \text{FeO}, \text{Fe},$ or Fe_3C) in the sample from the composition of oxide structure adapting the reference intensity ratio (RIR) methods [25]. x_i is the weight fraction of component i according to the intensity of X-rays diffracted by a selected plane (hkl) of the component. RD_i is the reduction degree of the different iron structures, where RD_i of $\text{Fe}_2\text{O}_3, \text{Fe}_3\text{O}_4, \text{FeO}, \text{Fe},$ and Fe_3C are 0%, 11%, 30%, 100%, and 100%, respectively.

3.3. Result and discussions

3.3.1. Ethanol decomposition over goethite (GE) ore

The ethanol was charged into the reactor with the liquid flow rate of 0.04 ml min^{-1} in an argon flow at 100 Nml min^{-1} ($3623 \text{ } \mu\text{mol min}^{-1}$) at a transient temperature of 100

– 900 °C with a heating rate of 10 K min⁻¹. The observed amount of remaining ethanol is address as the ethanol molar flowrates in the bulk gas phase at the outlet reactor calculated from the gas concentration measured by QMS and the total gas flowrate. Figure 3.4(a) shows the comparison of the remaining ethanol molar flowrates on the decomposition in three cases. Case 1 is the ethanol decomposition without introducing any ore to observe only the ethanol thermal decomposition behavior under an inert atmosphere. Cases 2 and 3 are the ethanol decomposition introducing the raw and dehydrated GE ore (porous hematite ore), respectively. In Case 1, the ethanol molar flowrate increases rapidly to 390 μmol min⁻¹ at 150 °C as initial charged, then slowly reaches its maximum of 632 μmol min⁻¹ at 550 °C. The ethanol molar flowrates decrease above 550 °C as significant thermal decomposition of ethanol occurs. When iron ores were introduced in Cases 2 and 3, the ethanol molar flowrates decrease more significantly due to catalytic decomposition of ethanol through iron ores. The molar flowrate of ethanol (at 0.04 ml min⁻¹ of liquid) entering the reactor was 686 μmol min⁻¹. This value was calculated considering the ethanol liquid density and molar mass of 0.789 g ml⁻¹ (20 °C) and 46.07 g mol⁻¹, respectively. However, it was difficult to reach this value on the experiment since the total vaporization of ethanol and the thermal decomposition co-occurs at elevated temperature. The lower ethanol molar flowrate at below 550 °C is not because of a faster ethanol decomposition occur, but the ethanol vaporization rates seem slower at these temperatures. Therefore, to estimate the initial molar flowrate of ethanol entering the reactor without any decomposition reaction at this transient state, the reference line was roughly estimated using the logarithmic trend of ethanol molar flowrate of Case 1 among temperatures of 150-300 °C resulting the correlation equation of $\dot{n}_{C_2H_5OH Case 1} = 175.56 \ln(T) - 475.51$ with R² value (the goodness of fit) of 0.9714. $\dot{n}_{C_2H_5OH Case 1}$ is

the molar flowrate of ethanol in the Case 1 [$\mu\text{mol min}^{-1}$] and T is the selected temperature in the assumption of no ethanol decomposition. The trendline was then extrapolated to reach the molar flowrate of $686 \mu\text{mol min}^{-1}$ at a higher temperature.

(a) Ethanol molar flowrate in outlet reactor

(b) Ethanol conversions

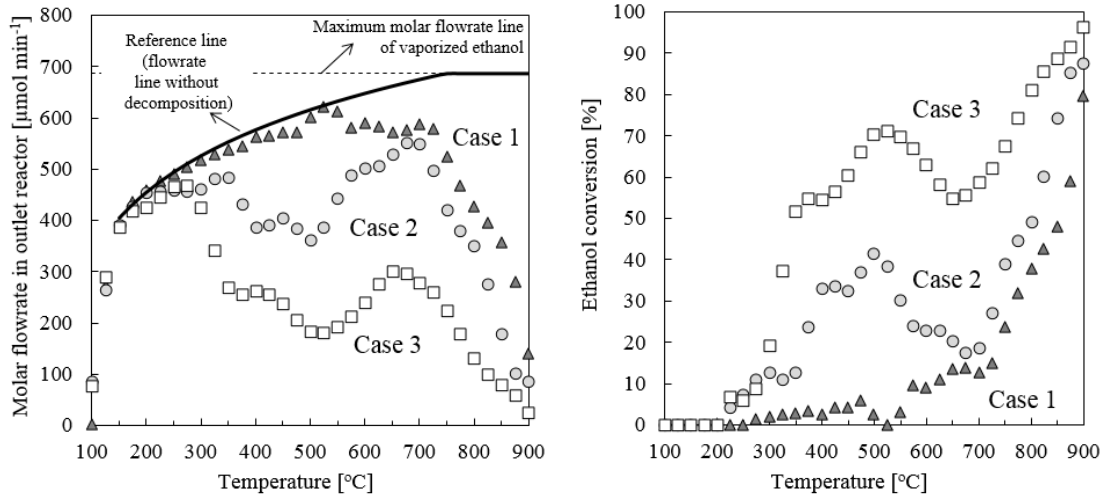


Figure 3.3.1 (a) Ethanol molar flowrates in outlet reactor and (b) conversions during the decomposition process. Case 1 is the ethanol decomposition without introducing any ore. Case 2 and Case 3 are the ethanol decomposition introducing the original GE ore (raw ore) and dehydrated GE ore (porous ore), respectively. The reference line in (a) was roughly estimated using the logarithmic trendline of ethanol flowrate of Case 1 among temperatures of 150-300 oC then extrapolated to reach the molar flowrate of $686 \mu\text{mol min}^{-1}$ at the higher temperature.

The ethanol conversion as depicted in Figure 3.3.1(b) was calculated from

$$X_{C_2H_5OH} [\%] = \frac{\dot{n}_{C_2H_5OH in} - \dot{n}_{C_2H_5OH(T)}}{\dot{n}_{C_2H_5OH in}} \times 100\% \quad (3.3-1)$$

where $X_{C_2H_5OH}$ is the conversion of ethanol on the decomposition process. $\dot{n}_{C_2H_5OH in}$ is the initial molar flowrate of ethanol entering the reactor in gas phase [$\mu\text{mol min}^{-1}$] at the reference line. $\dot{n}_{C_2H_5OH(T)}$ is the molar flowrate of the remaining ethanol as calculated from the measurement by QMS during the experiments. The profiles of ethanol conversion reveal that the more significant ethanol decomposition occurred over dehydrated GE ore. According to the N_2 adsorption analysis result, the surface area of

GE ores, both original and dehydrated ores, were 21 and 92 m² g⁻¹, respectively. Because the ethanol conversion increases in accordance with the increase of the surface area of the iron ore, it can be interpreted that the ethanol decomposition takes place inside the iron ore pores. The ethanol conversion in the presence of iron ores (both Cases 2 and 3) significantly increased at 300–500 °C because of the catalytic activity of the iron ore. The ethanol conversion slightly decreased at 500–650 °C and increased again at above 650 °C. Somehow, the catalytic activity of the iron ore might be reduced at 500–650 °C in the ethanol decomposition. It is probably due to the structure change of the iron oxide during ethanol decomposition, as well reported in similar research [19].

Figure 3.3.2 shows the gas evolved analysis of H₂, CH₄, CO, H₂O, and CO₂ during the ethanol decomposition process for the three cases. In Case 1, significant thermal decomposition occurred above 700 °C as per the increasing H₂, CO, and CH₄ profiles. Meanwhile, for Cases 2 and 3, those gases started to increase at 300 °C, confirming that the catalytic decomposition of ethanol starts to occur at this temperature, which is significantly lower than that of the thermal decomposition. The H₂ generation of both Cases 2 and 3 are correlated to the decomposition of ethanol on the ore. The decrease in H₂ and CO molar flowrates for both Cases 2 and 3 between 500–650 °C also corresponds to the behavior of ethanol decomposition. The CO₂ and H₂O gases were not significantly increased in the case of the thermal decomposition of ethanol. It can be interpreted as the CO₂ and H₂O not being generated initially from the ethanol decomposition. For Cases 2 and 3, it seems evident that with the addition of ores, the generated H₂, CO, CH₄, H₂O, and CO₂ gases increased significantly. The significant increase of CO₂ and H₂O in Cases 2 and 3 reveals that those gases are generated from other reactions involved instead of

ethanol decomposition. Those possible reactions might be steam reforming, water gas shift reaction, and iron oxide reduction.

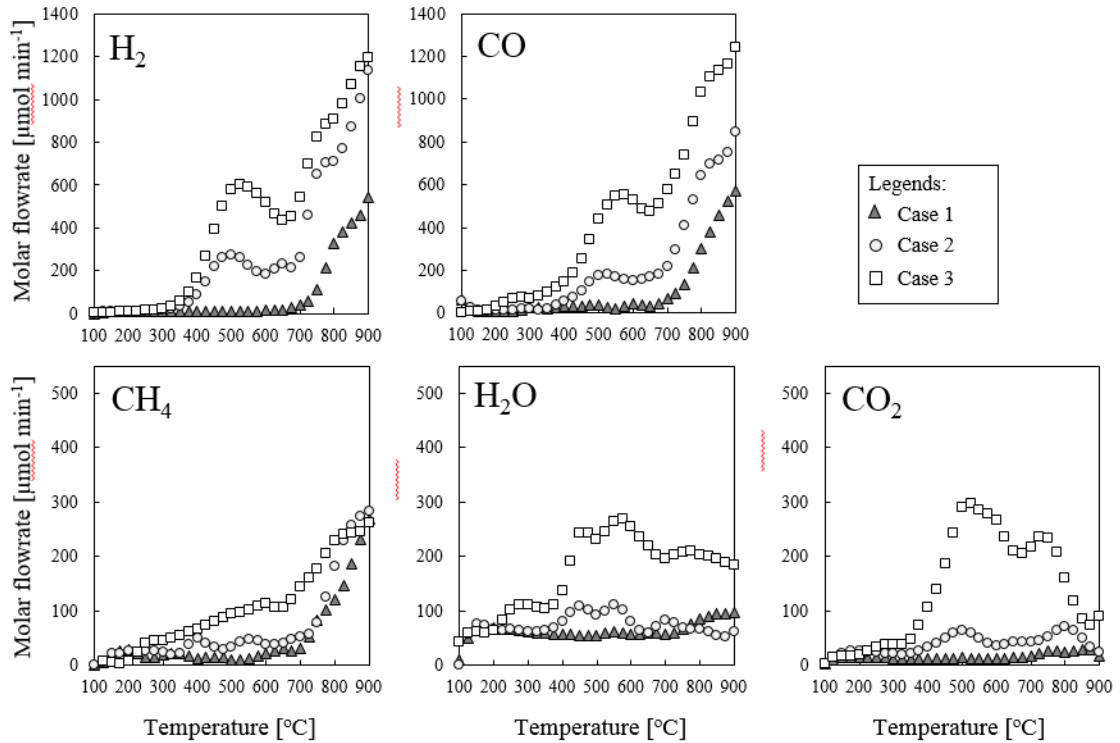


Figure 3.3.2 Gases generation during ethanol decomposition. Case 1 is the ethanol decomposition without introducing any ore. Case 2 and Case 3 are the ethanol decomposition introducing the original goethite ore (raw ore) and dehydrated goethite ore (porous ore), respectively.

Carbon deposition also found in iron ore was introduced in the ethanol decomposition process. Figure 3.6 shows that some carbon is deposited in the iron ore during the ethanol decomposition process. Higher carbon deposition from ethanol decomposition was found at higher temperatures. Some studies have reported that carbon deposited from ethanol and CH_4 has similar behavior in deposition rate and microstructure evolution [26]. The carbon deposition is well correlated with the behavior of ethanol decomposition; as well, as more CH_4 is generated, more carbon is deposited. However, the structures of the deposited carbon will be left for further study.

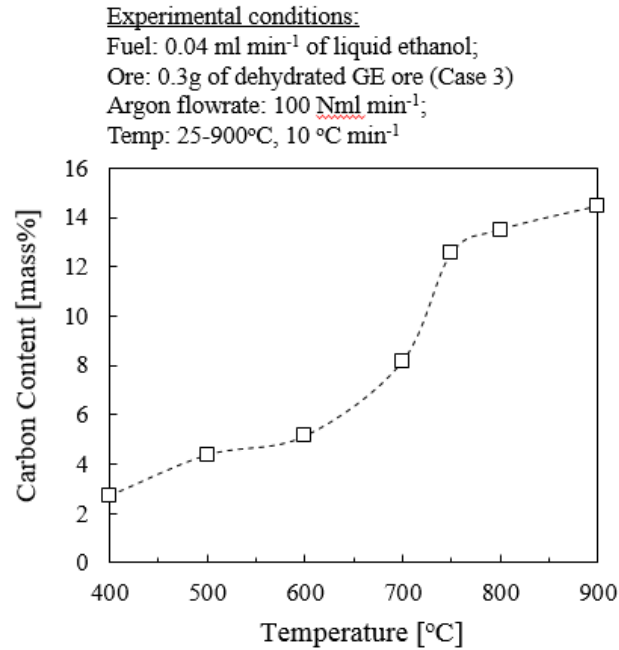
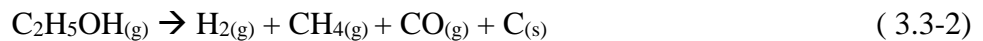


Figure 3.3.3 Carbon content of dehydrated GE ore during the ethanol decomposition process. Carbon deposition increases significantly at higher temperatures.

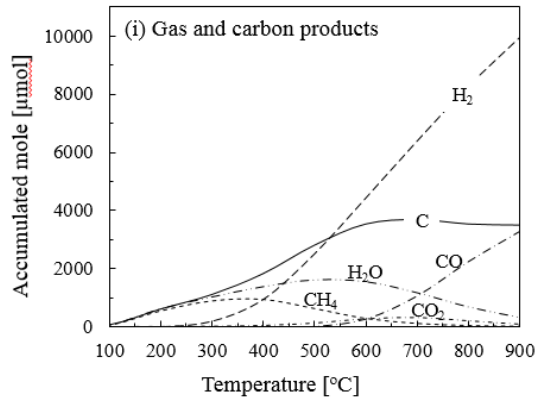
So far, the possible reactions involved during ethanol decomposition over iron ore pore surface are:



A thermodynamic calculation using HSC v5.1 software (Outokumpu) was conducted to obtain the equilibrium product distribution during the ethanol

decomposition. The results might be used to estimate how far the equilibrium to be. Figure 5 shows the thermodynamic equilibrium of the product distribution during the ethanol decomposition reaction in two cases: thermal decomposition of ethanol and ethanol decomposition with iron oxide reduction. In the case of thermal decomposition of ethanol (Figure 3.7(a)), theoretically, at lower temperatures, ethanol is completely decomposed to CH_4 , H_2O , and deposited carbon. Above 200 °C, CH_4 then decomposes to H_2 and more deposited carbon. CH_4 and H_2O significantly decrease because steam reforming and water gas shift reactions slightly occur releasing CO_2 also occur at 300–600 °C. Above 600 °C, the Boudouard reaction significantly occurs, decreasing the deposited carbon and CO_2 to generate more CO . At the higher temperature, ethanol is thermally decomposed to H_2 , CO , and deposited carbon. Significantly, when iron oxide (Fe_2O_3) is introduced to the ethanol decomposition (Figure 3.7(b)), H_2 is consumed for iron reduction, thus releasing more H_2O . CO_2 also increases because of the iron reduction by CO . Interestingly, CO still increases because of direct reduction by consuming the deposited carbon, generating more CO rather than the CO being consumed by indirect reduction.

(a) Product distribution of ethanol decomposition



(b) Product distribution of ethanol decomposition with iron oxide reduction

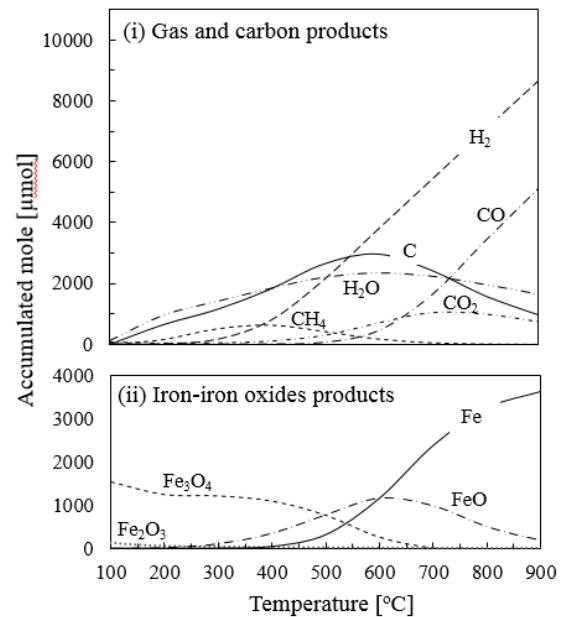


Figure 3.3.4 Thermodynamic equilibrium on product distribution during ethanol decomposition reaction in two cases: thermal decomposition of ethanol (a) and ethanol decomposition with iron oxide reduction (b). These calculations were conducted using software HSC 5.11 (Outokumpu).

Comparing the analysis and the experiments shows that the trend of product distributions of ethanol decomposition was different from the thermodynamic results of the equilibrium condition. The equilibrium conditions can only be reached when the reactions are held for a long time at each temperature. In contrast, in the temperature-programmed conditions of the experiments, the reaction occurred while the temperature increased, with no holding temperature. The residence times of iron bed (length of 7 mm) as ethanol catalytic decomposition are range from 0.12 - 0.10 s at 100 - 900 °C. The thermal decomposition might occur in the heated part of the reactor tube between the upper and lower quartz wool. In this case, considering the length of the heated part (200 mm), the total residence time of the reactor becomes 3.36 – 2.77 s at 100 – 900 °C. The values of both residence times were calculated from the volume of iron bed and the heated part of the reactor tube divided by the measured volumetric flowrate, respectively. By

considering the experimental method with the thermal state is continuously changing with elevated temperature and the short of residence time, the ethanol decomposition in the experiments might be still far from equilibrium condition. However, the H₂, CO, and CO₂ trends already correspond with the equilibrium trends at the higher temperatures. Meanwhile, CH₄ and deposited carbon in the experiments were still increasing with the ethanol still being decomposed.

3.3.2. Reduction behavior of porous iron ore at different temperatures

To observe the reduction behavior of porous iron ore, the reactor operation was interrupted at 100 °C intervals. The samples then were quickly cooled and observed using XRD. The reduction behavior of dehydrated GE ores using ethanol decomposition is shown in Figure 3.8. XRD patterns at different temperatures show that after mild-dehydration at 300 °C, GE ore has completely decomposed to hematite. After the introduction of ethanol decomposition, hematite is already reduced to magnetite at 600 °C, FeO starts to be formed at 700 °C, and metallic Fe has significantly formed at 750 °C. No FeO remains at 900 °C. Other report mentioned that in the case of introducing ethanol to iron oxide reagents [19], hematite is reduced mainly to magnetite up to 500 °C. Some FeO is formed at 600 °C. Then, at 700 °C, mainly the metallic Fe is formed. However, the higher temperatures used in this study probably caused by the presence of gangue materials in the iron ores, the difference in the particle sizes, and the number of materials employed. Figure 6 shows that the RD increases significantly from 18% at 600 °C to 81% at 750 °C. For blast furnace operation in the case of coke-iron ore [27], a reduction degree of over than 80% is reached at 1000 °C. Thus, using ethanol as an

ironmaking fuel for porous ore, significant reduction occurs at a lower temperature than when using coke fuel in the case of a blast furnace.

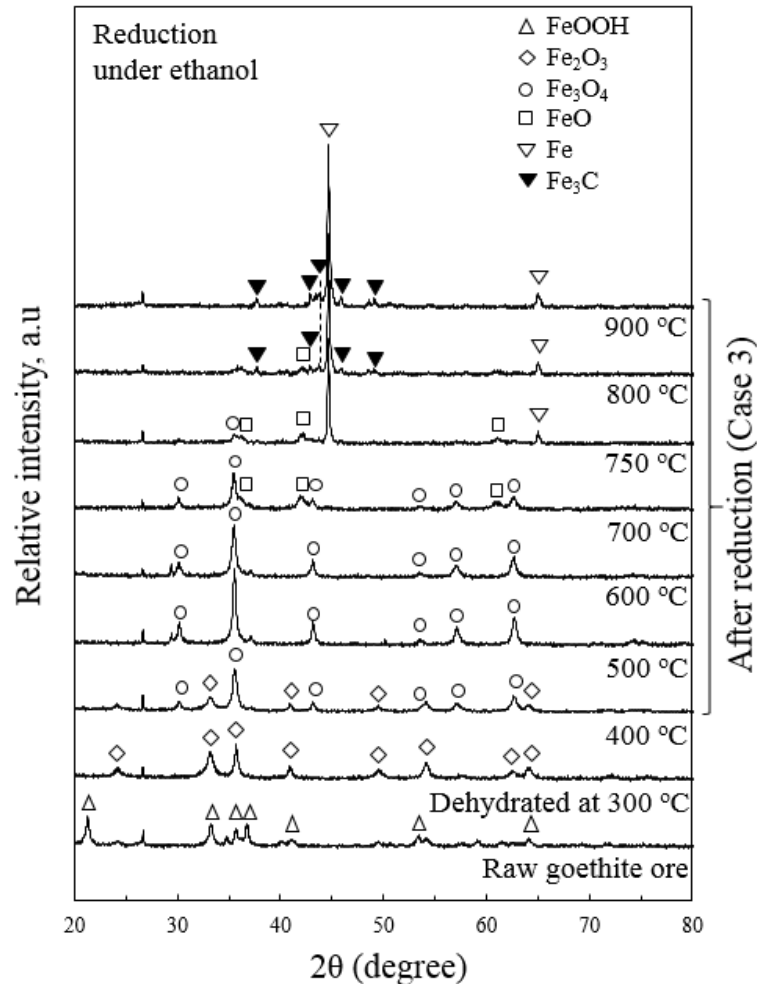


Figure 3.3.5 XRD patterns and the reduction degree of iron ore on ethanol decomposition at different temperatures. Experimental conditions were: 0.04 ml min⁻¹ of ethanol, 0.3 g of DH300 GE ore, argon flow rate of 100 Nml min⁻¹, and heating rate of 10 °C min⁻¹.

3.3.3. Reduction behaviors at different ethanol flow rates and starting temperatures

Figure 3.9 shows the reduction behavior of dehydrated GE ore at different ethanol flow rates. On the XRD result (Figure 3.9(a)), significant metallic Fe was found only at a liquid ethanol flowrate of 0.04 ml min⁻¹. This phenomenon might be correlated to the composition ratio of H₂ to H₂ + H₂O during the ethanol decomposition (Figure 3.9(b)) in

accordance with the phase diagram of iron oxides. It seems that only a liquid ethanol flow rate of 0.04 ml min^{-1} provides a sufficient H_2 ratio to produce metallic Fe.

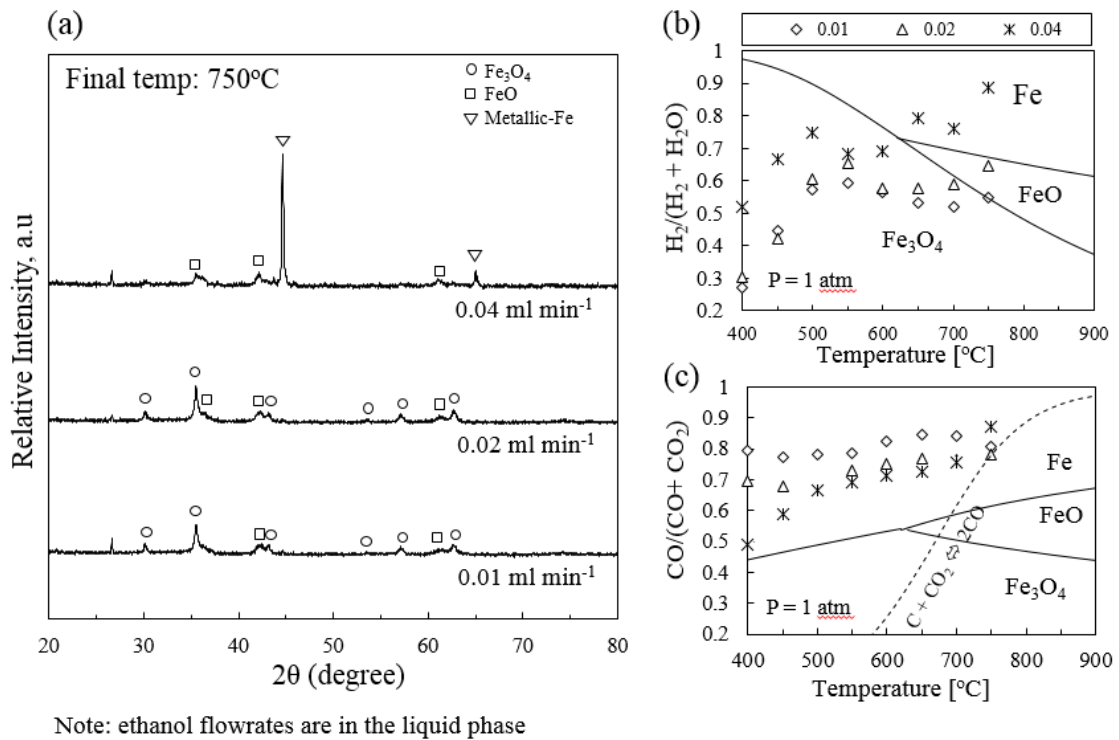


Figure 3.3.6 (a) XRD patterns of the dehydrated goethite ore on ethanol decomposition at different ethanol flowrates. The ratio of reducing gas (b) H_2 to $\text{H}_2 + \text{H}_2\text{O}$ and (c) CO to $\text{CO} + \text{CO}_2$ during the decomposition process.

However, at liquid ethanol flow rates of 0.01 , 0.02 , and 0.04 ml min^{-1} , the composition ratios of CO to $\text{CO} + \text{CO}_2$ seem sufficient to produce metallic Fe (Figure 7(c)). In this case, the reduction behavior might correspond more to the amount of H_2 than CO . This result agrees with some reports that the lower-temperature reduction behavior predominates because of the iron reduction of H_2 rather than CO . The reduction by H_2 was reported to practically occur at $590\text{--}630 \text{ }^\circ\text{C}$, which is lower than that by CO at $700\text{--}900 \text{ }^\circ\text{C}$ [28–31].

Figure 3.10 shows the XRD patterns, reduction degree, and carbon content of porous iron ores at different starting temperatures of ethanol charged. When ethanol starts

charging at 100 °C, the highest amount of deposited carbon of 14 mass-% and an RD of 81% were obtained. At 200 °C, the deposited carbon and the RD decreased to 11 mass-% and 57%, respectively. At 300 °C, even using a higher flow rate of 0.06 ml min⁻¹, the RD reached only 36%, and the deposited carbon content reached only 9 mass-%.

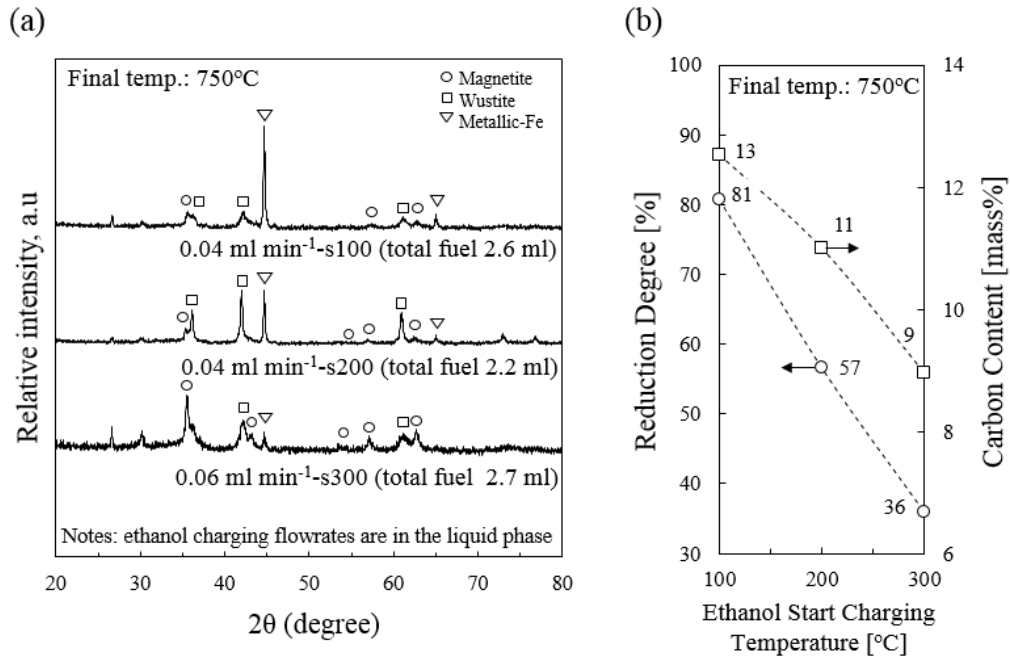


Figure 3.3.7 (a) XRD patterns and (b) reduction degrees and carbon contents of dehydrated goethite ore on ethanol decomposition at different ethanol start charging temperatures. The remarks of s100, s200, and s300 in (a) correspond to ethanol start charging temperature of 100, 200, and 300 oC in (b), respectively. Charging of the ethanol starts from each of those temperatures until a final temperature of 750 oC. The samples were observed after the final temperature was reached.

This result reveals that the more extended contact of ethanol with iron ore results in a higher deposited carbon and reduction degree. In this case, the critical factor might be the ethanol infiltration to the ore pore at the lower-temperature steps. This step ensures that the ethanol has a higher probability of having contact with all the iron oxide surfaces within the ore. It seems that the limiting step of the simultaneous ethanol decomposition and iron ore reduction process is the ethanol infiltration into the iron ore pores.

3.3.4. Reduction behaviors of different iron ores

Reduction behaviors for different iron ores at 750 °C were also investigated as shown by the XRD result in Figure 3.11(a). The FeOOH and porous Fe₂O₃ reagents were used as model compounds to compare the effect of porosity in iron ores on the reduction behaviors. Under ethanol decomposition, the FeOOH reagent can only be reduced to FeO with Fe₃O₄ remaining. The RD of the reduced FeOOH reagent was only 25%. Meanwhile, the porous Fe₂O₃ reagent (from FeOOH dehydration) shows significant reduction behavior, producing metallic Fe and FeO with a reduction degree of 74%. The dehydrated GE ore (Figure 10(b)) also has a significant reduction behavior as well as the dehydrated FeOOH reagent. The RD of the dehydrated GE ore (RD = 81%) was found to be higher than that of the dehydrated FeOOH reagent. The difference in reduction behavior between those two samples is probably due to the difference in the particle size employed. The porous Fe₂O₃ reagent has only 1 μm of particle size, whereas that of the dehydrated GE ore is 1-2 mm. The smaller particles size (1 μm) might agglomerate because of sintering, resulting in the smaller contact area between the iron oxide and the reducing agent, as similarly reported by other researchers [19].

Different iron ores with various CW contents showed different reduction behaviors in Figure 3.11 (b). The RD of porous GE, WA, and RC ores were 81%, 79%, and 69%, respectively. RC ore, as a high-grade ore, showed a lower reduction degree compared to other low-grade ores (WA and GE ore). The reduction degree of porous iron ores seems directly proportional to the surface area of the ores after dehydration: 92, 79, and 11 m² g⁻¹, respectively. RC ore has the smallest contact area with reducing agents (such as ethanol, CO, and H₂). Thus, the surface area of porous iron ores might play a role in the reduction behavior in ethanol-assisted ironmaking. The surface area is

generated by the removal of CW during the dehydration process. More CW contained in the ore corresponds to the larger surface area after mild-dehydration. Indirectly, higher CW in ore might provide more reactivity in the reduction process.

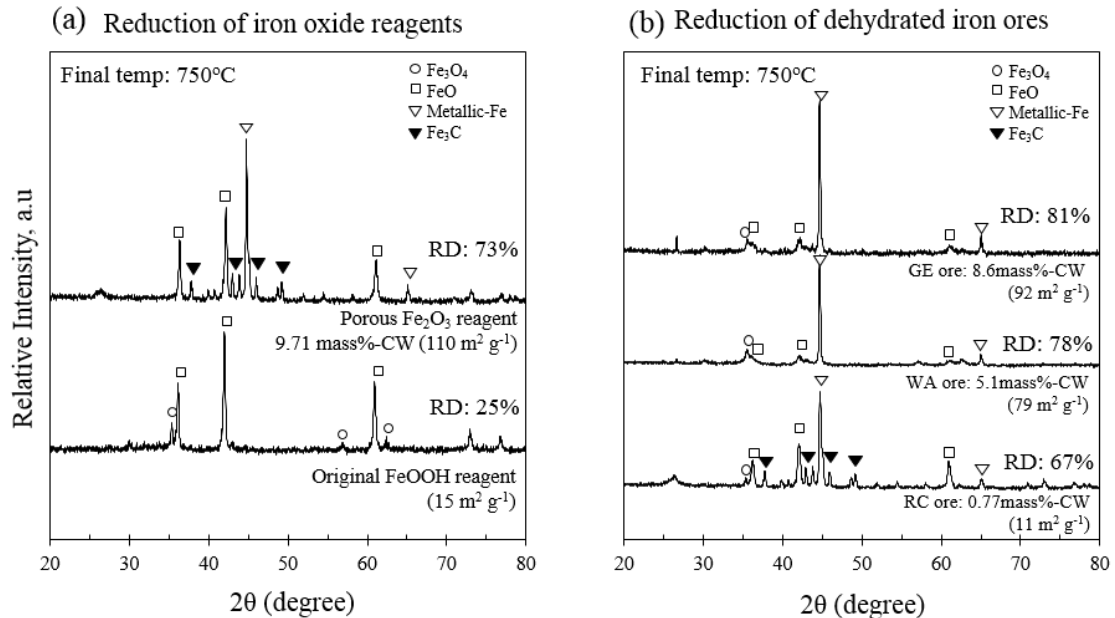
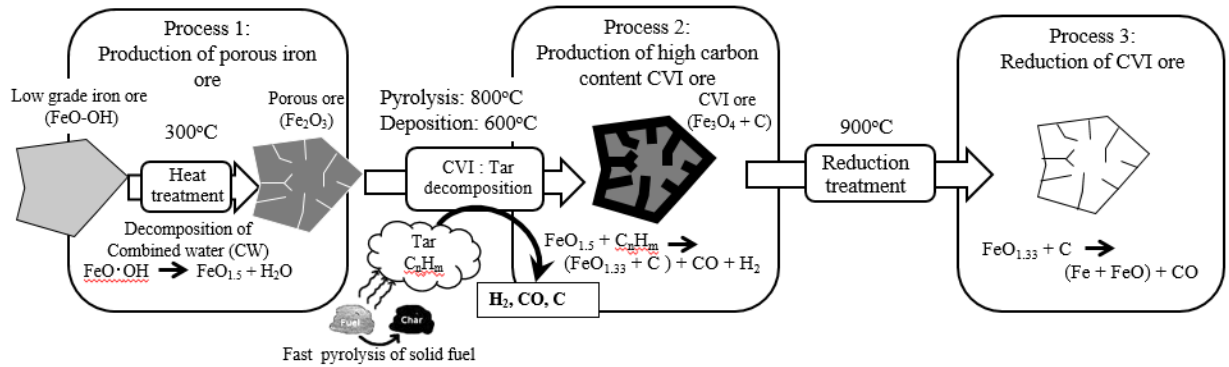


Figure 3.3.8 XRD patterns and the reduction degrees of different (a) iron oxides and (b) dehydrated ores after ethanol decomposition at 750 °C. The raw FeOOH reagent in (a) was used without dehydration treatment. The different CW contents in the samples show the significant difference of BET surface area (in the brackets) of ores after mild-dehydration treatments prior to reductions.

By introducing small-molecule carbonaceous material such as ethanol to porous ore reduction, the process intensification is fundamentally approached for CVI ironmaking development. Figure 3.12 shows the current proposed development of CVI ironmaking, including this study's result, proposing two steps for the CVI ironmaking process, a reduction of one step from the previous approach. Low-temperature iron reduction by ethanol may be attractive for future ironmaking processes. However, further studies are needed to clarify the feasibility of the proposed process regarding the availability ethanol sources for ironmaking, possible reactor designs, carbon removal from the reduced iron, slag-hot metal separation, and residual gas (CO-H₂) recovery.

Previous approach: 3-steps process



Current approach: 2-steps process

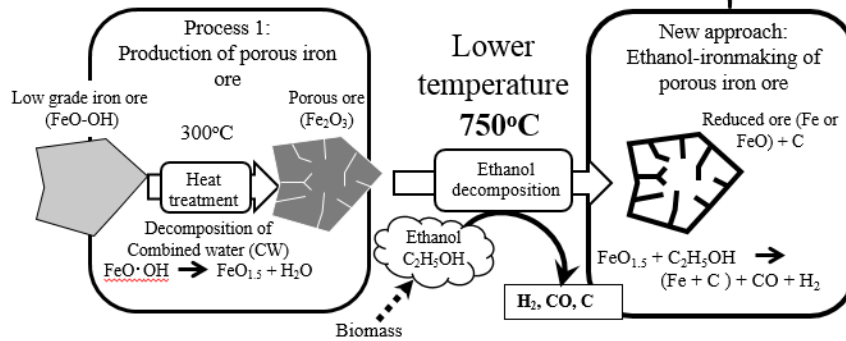


Figure 3.3.9 Previous and current approaches in the development of CVI ironmaking. The current approach results in significant process intensification compared with the previous approach.

3.4. Conclusions

Ethanol, a renewable source and considered carbon neutral when it is derived from biomass, is a promising candidate as a reducing agent for ironmaking. A fundamental experiment of ethanol decomposition over porous iron ore was conducted, resulting in several conclusions:

1. Ethanol is decomposed to CO-H₂ that then reduces the iron oxide via indirect reduction. The reduction temperature of 750 °C is significantly lower than that of the coke-iron oxide reaction in recent blast furnace operations, reaching an RD of 81%.

2. A longer time of ethanol charging in the porous iron ore promotes a more significant reduction degree, and the compositions of the reducing gas (H₂ and CO) are sufficient for the reduction process.
3. A significant reduction degree can be reached by ethanol decomposition with the porous ore from mild-dehydrating the high-CW ore. Porous iron ore acts as a suitable catalyst for ethanol decompositions as it simultaneously reduces to metallic iron. The higher CW in ore might provide the larger surface area in the iron ore, resulting in higher reactivity in the reduction process.

The result of the proposed process intensification in the CVI ironmaking process reduces one step from the previous approach. Low-temperature iron reduction by ethanol may be attractive for future ironmaking processes.

References

- [1] J. Rogelj, M. Den Elzen, N. Höhne, T. Fransen, H. Fekete, H. Winkler, R. Schaeffer, F. Sha, K. Riahi, M. Meinshausen, Paris Agreement climate proposals need a boost to keep warming well below 2 °c, *Nature*. 534 (2016) 631–639. doi:10.1038/nature18307.
- [2] A. Kasai, Y. Matsui, Lowering of thermal reserve zone temperature in blast furnace by adjoining carbonaceous material and iron ore, *ISIJ Int.* 44 (2004) 2073–2078. <http://jlc.jst.go.jp/DN/JALC/00245253179?from=Google>.
- [3] B.H. Huang, W.K. Lu, Kinetics and mechanisms of reactions in iron-ore coal composites, *ISIJ Int.* 33 (1993) 1055–1061. doi:10.2355/isijinternational.33.1055.
- [4] K. Nagata, R. Kojima, T. Murakami, M. Susa, H. Fukuyama, Mechanisms of Pig-iron Making from Magnetite Ore Pellets Containing Coal at Low Temperature., *ISIJ Int.* 41 (2001) 1316–1323. doi:10.2355/isijinternational.41.1316.

- [5] J.M. McClelland, G.E. Metius, Recycling ferrous and nonferrous waste streams with FASTMET, *Jom.* 55 (2003) 30–34. doi:10.1007/s11837-003-0101-3.
- [6] T. Murakami, T. Akiyama, E. Kasai, Reduction Behavior of Hematite Composite Containing Polyethylene and Graphite with Different Structures with Increasing Temperature, *ISIJ Int.* 49 (2009) 809–814. doi:10.2355/isijinternational.49.809.
- [7] Y. Hata, H. Purwanto, S. Hosokai, J. Hayashi, Y. Kashiwaya, T. Akiyama, Biotar Ironmaking Using Wooden Biomass and Nanoporous Iron Ore, *Energy & Fuels.* 23 (2009) 1128–1131. doi:10.1021/ef800967h.
- [8] G. Saito, T. Nomura, N. Sakaguchi, T. Akiyama, Optimization of the Dehydration Temperature of Goethite to Control Pore Morphology, 56 (2016) 1598–1605. doi:10.2355/isijinternational.ISIJINT-2016-231.
- [9] A.N. Rozhan, R.B. Cahyono, N. Yasuda, T. Nomura, S. Hosokai, H. Purwanto, T. Akiyama, Carbon deposition from biotar by fast pyrolysis using the chemical vapor infiltration process within porous low-grade iron ore for iron-making, *Energy & Fuels.* 26 (2012) 7340–7346. doi:10.1021/ef301409f.
- [10] R.B. Cahyono, A.N. Rozhan, N. Yasuda, T. Nomura, H. Purwanto, T. Akiyama, Carbon Deposition Using Various Solid Fuels for Ironmaking Applications, *Energy & Fuels.* 27 (2013) 2687–2692. doi:10.1021/ef400322w.
- [11] R.B. Cahyono, A.N. Rozhan, N. Yasuda, T. Nomura, S. Hosokai, Y. Kashiwaya, T. Akiyama, Catalytic coal-tar decomposition to enhance reactivity of low-grade iron ore, *Fuel Process. Technol.* 113 (2013) 84–89. doi:10.1016/j.fuproc.2013.03.012.
- [12] T. Nomura, R.B. Cahyono, T. Akiyama, Ironmaking System Including Coproduction of Carbon-Loaded Iron Oxide and Reformed Coke Oven Gas by Chemical Vapor Infiltration Process, *J. Sustain. Metall.* 1 (2015) 115–125. doi:10.1007/s40831-015-0012-x.
- [13] R.B. Cahyono, N. Yasuda, T. Nomura, T. Akiyama, Utilization of Low Grade Iron Ore (FeOOH) and Biomass Through Integrated Pyrolysis-tar Decomposition (CVI process) in

- Ironmaking Industry: Exergy Analysis and its Application, *ISIJ Int.* 55 (2015) 428–435. doi:10.2355/isijinternational.55.428.
- [14] R.B. Cahyono, G. Saito, N. Yasuda, T. Nomura, T. Akiyama, Porous ore structure and deposited carbon type during integrated pyrolysis-tar decomposition, *Energy & Fuels*. 28 (2014) 2129–2134. doi:10.1021/ef500201m.
- [15] Y. Mochizuki, M. Nishio, N. Tsubouchi, T. Akiyama, Reduction behavior and crushing strength of carbon-containing pellet prepared from COG tar, *Fuel Process. Technol.* 142 (2016) 287–295. doi:10.1016/j.fuproc.2015.10.025.
- [16] R.B. Cahyono, N. Yasuda, T. Nomura, T. Akiyama, Optimum temperatures for carbon deposition during integrated coal pyrolysis-tar decomposition over low-grade iron ore for ironmaking applications, *Fuel Process. Technol.* 119 (2014) 272–277. doi:10.1016/j.fuproc.2013.11.006.
- [17] A. Kurniawan, K. Abe, T. Nomura, T. Akiyama, Integrated Pyrolysis–Tar Decomposition over Low-Grade Iron Ore for Ironmaking Applications: Effects of Coal-Biomass Fuel Blending, *Energy & Fuels*. 32 (2018) 396–405. doi:10.1021/acs.energyfuels.6b02509.
- [18] S. Hosokai, K. Matsui, N. Okinaka, K. Ohno, M. Shimizu, T. Akiyama, Kinetic Study on the Reduction Reaction of Biomass-Tar-Infiltrated Iron Ore, *Energy & Fuels*. 26 (2012) 7274–7279. doi:10.1021/ef3013272.
- [19] M.G. Rosmaninho, F.C.C. Moura, L.R. Souza, R.K. Nogueira, G.M. Gomes, J.S. Nascimento, M.C. Pereira, J.D. Fabris, J.D. Ardisson, M.S. Nazzarro, K. Sapag, M.H. Araújo, R.M. Lago, Investigation of iron oxide reduction by ethanol as a potential route to produce hydrogen, *Appl. Catal. B Environ.* 115–116 (2012) 45–52. doi:10.1016/j.apcatb.2011.11.038..
- [20] D. Pimentel, A. Marklein, M.A. Toth, M.N. Karpoff, G.S. Paul, R. McCormack, J. Kyriazis, T. Krueger, Food versus biofuels: Environmental and economic costs, *Hum. Ecol.* 37 (2009) 1–12. doi:10.1007/s10745-009-9215-8.

- [21] F.M. Liew, M.E. Martin, R.C. Tappel, B.D. Heijstra, C. Mihalcea, M. Köpke, Gas Fermentation-A flexible platform for commercial scale production of low-carbon-fuels and chemicals from waste and renewable feedstocks, *Front. Microbiol.* 7 (2016). doi:10.3389/fmicb.2016.00694..
- [22] X. Ou, X. Zhang, Q. Zhang, X. Zhang, Life-cycle analysis of energy use and greenhouse gas emissions of gas-to-liquid fuel pathway from steel mill off-gas in China by the LanzaTech process, *Front. Energy.* 7 (2013) 263–270. doi:10.1007/s11708-013-0263-9.
- [23] R.M. Handler, D.R. Shonnard, E.M. Griffing, A. Lai, I. Palou-Rivera, Life Cycle Assessments of Ethanol Production via Gas Fermentation: Anticipated Greenhouse Gas Emissions for Cellulosic and Waste Gas Feedstocks, *Ind. Eng. Chem. Res.* 55 (2016) 3253–3261. doi:10.1021/acs.iecr.5b03215.
- [24] K. Abe, G. Saito, T. Nomura, T. Akiyama, Limonitic Laterite Ore as a Catalyst for the Dry Reforming of Methane, *Energy & Fuels.* 30 (2016) 8457–8462. doi:10.1021/acs.energyfuels.6b00940.
- [25] C.R. Hubbard, R.L. Snyder, RIR-measurement and use in quantitative XRD, *Powder Diffr.* 3(1988) 74-77. doi: 10.1017/S0885715600013257.
- [26] A. Li, S. Zhang, B. Reznik, S. Lichtenberg, O. Deutschmann, Synthesis of Pyrolytic Carbon Composites Using Ethanol As Precursor, *Ind. Eng. Chem. Res.* 49 (2010) 10421–10427. doi:10.1021/ie100230b.
- [27] J.A. de Castro, H. Nogami, J. Yagi, Transient mathematical model of blast furnace based on multi-fluid concept, with application to high PCI operation, *ISIJ Int.* 40 (2000) 637–646. doi:10.2355/isijinternational.40.637.
- [28] K. Abe, A. Kurniawan, T. Nomura, T. Akiyama, Effects of reduction on the catalytic performance of limonite ore, *J. Energy Chem.* 0 (2017) 1–7. doi:10.1016/j.jechem.2017.09.032.
- [29] B. Hou, H. Zhang, H. Li, Q. Zhu, Study on kinetics of iron oxide reduction by hydrogen, *Chinese J. Chem. Eng.* 20 (2012) 10–17. doi:10.1016/S1004-9541(12)60357-7.

- [30] H. Chen, Z. Zheng, W. Shi, Investigation on the kinetics of iron ore fines reduction by CO in a micro-fluidized bed, *Procedia Eng.* 102 (2015) 1726–1735. doi:10.1016/j.proeng.2015.01.308.
- [31] C.D. Bohn, J.P. Cleeton, C.R. Müller, J.F. Davidson, A.N. Hayhurst, S.A. Scott, J.S. Dennis, The kinetics of the reduction of iron oxide by carbon monoxide mixed with carbon dioxide. *AIChE J.* 56 (2010) 1016-1029. Doi: 10.1002/aic.12084.
- [32] S.P. Trushenski, K. Li, W.O. Philbrook, Non-Topochemical Reduction of Iron Oxides, *Metall. Trans.* 5 (1974) 1149–1158. doi:10.1007/BF02644326.

CHAPTER IV

KINETIC STUDY ON SIMULTANEOUS ETHANOL DECOMPOSITION AND IRON REDUCTION UNDER TEMPERATURE PROGRAMMED CONDITION

4.1. Introduction

The light alcohol such as ethanol is a prominent candidate as a reducing agent for ironmaking [1]. Not only is it less hazardous but it can be produced from a variety of biomass sources. Its use could possibly lead to a decrease in CO₂ emissions. Currently, bioethanol is produced by the fermentation of sugar cane, corn grains, and other starch-rich materials, and is a mature technology [2]. Recent researchers have focused on producing bioethanol from lignocellulosic biomass, the so-called second-generation bioethanol. Ethanol production from lignocellulose would open the possibility for the utilization of different and low-cost biomass, such as agricultural wastes and forestry residues (e.g., straw, grasses, corn stover, and wood); in this way, a competition of energy-food production from agricultural sources would be avoided [3]. Another remarkable finding of ethanol production from gas fermentation, recently, is also getting more attractive to be implemented. Ethanol recovery like Lanzatech process, utilize the tail gas of iron and steelmaking processes might be one approach to realize the idea to ensure ethanol security as ironmaking fuel [4]. Yet, more approaches are needed to evaluate the benefit of ethanol utilization as a reduction agent for ironmaking.

On the other hand, the abundance of goethite over hematite and magnetite ore might need more attention to be effectively utilized. Goethite, is a low-grade iron ore containing high combined water, needs more energy to be converted to hematite through a dehydration process prior to reduction [5]. For compensating the energy requirement

for a dehydration process, the reduction reaction should be faster or held at a lower temperature. As mentioned in the previous study, ethanol reduces the iron oxide at a low temperature compared to coke-iron oxide reaction; this feature is attributed to iron reduction by H_2 . Figure 4.1.1 shows the processing mechanism of ironmaking utilizing the porous iron ore from goethite dehydration as raw material.

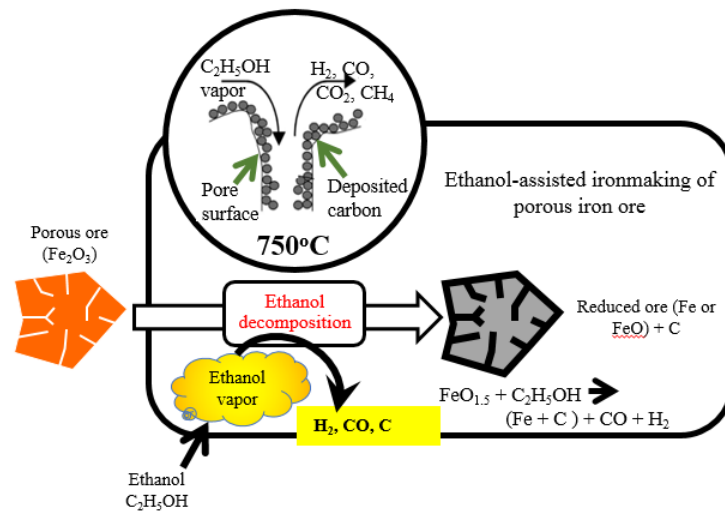


Figure 4.1.1 Mechanism of ethanol decomposition – iron reduction

Ethanol is decomposed to H_2 , CO , and C that then reduces the iron oxide via indirect reduction and direct reduction. The reduction temperature of $750^\circ C$ is significantly lower than that of the coke-iron oxide reaction in recent blast furnace operations, reaching an RD of 81% [1]. Kinetic study on carbon composite ore through CVI method mentioned that a nano-contact between the iron oxide (within ore) and carbon from carbonized tar is one important key to perform a fast reduction reaction and lowering reduction temperature [6].

Ethanol assisted-ironmaking, however, is one novel idea to utilize ethanol as one of biomass form to be a reducing agent in ironmaking. However, it is still unclear, in particular, the mechanism of simultaneous ethanol decomposition and iron reduction still

remain unknown. Therefore, a kinetic study is necessary to explain more detailed mechanisms of the process. This study will reveal the understanding of the aspects of the simultaneous ethanol decomposition-iron reduction process. Overall, the hope is to move us closer to make the beneficial use of bioethanol as a reducing agent in the ironmaking process.

4.2. Experimental Methods

4.2.1. Sample preparation

Australian goethite (GE) with the total Fe content of 57wt% and combined water (CW) of 8.6wt% was employed in this study. The original ore was sieved so that a particle size ranged from 1 to 2 mm. Two cases of ore were prepared, the original (without dehydration) and the mild-dehydrated ones. The porous ore was prepared by mild-dehydration at 573 K with a heating rate of 3 K min⁻¹ and kept for 24 h under air atmosphere as the method like in [1]. The surface area and pore volume of the ores were analyzed using N₂ adsorption equipment (Autosorb 6AG, Quantachrome) to confirm the effect before and after, as shown in Table 4.2.1.

Table 4.2.1 *Brunauer-Emmett-Teller* (BET) surface area and total pore volume of different iron ores before and after mild-dehydration treatments.

Sample	BET surface area [m ² /g]		Total pore volume [cm ³ /g]	
	Original ^a	Dehydrated ^b	Original ^a	Dehydrated ^b
Goethite ore	15	110	0.1301	0.1760

a = as received, b = after 24 h dehydration at 300 °C under air atmosphere

SAA analyzer condition: Adsorbate N₂, mol. wt = 28.0134 g/mol, cross-sec area = 16.2 Å²/molec., non-ideality = 6.580×10⁻⁰⁵, P/Po toler. = 2, outgas temp.= 120 °C, outgas time = 1.0 h, bath temp. = 77.35 K.

4.2.2. Simultaneous ethanol decomposition and iron reduction in temperature programmed reaction

Approximately 0.3 g of dehydrated iron ore was placed in a quartz tube reactor (ID of 6 mm) equipped with an infrared furnace using approximately 0.04 g of quartz wool as bed support. The detailed information of the reactor set was reported in [1]. Argon at 100 Nml min⁻¹ was introduced to keep the atmosphere in an inert condition. The reactor was heated in a vertical infrared furnace to different temperatures (673–1173 K) at a heating rate of 10 K min⁻¹. Ethanol reagent (99.5 vol%) at 0.04 ml min⁻¹ was drop-wise introduced using a flow-controlled peristaltic pump into the reactor starting at 373 K until the final temperature reached. The outlet gases, such as C₂H₅OH, H₂, CH₄, CO, CO₂, and H₂O were analyzed online using quadruple mass spectroscopy (QMS200, Pfeiffer).

4.2.3. Sample analysis and characterizations

4.2.3.1. Gas analysis

The outlet reactor gases, such as C₂H₅OH, H₂, CH₄, CO, CO₂, and H₂O were analyzed online using quadruple mass spectroscopy (QMS200, Pfeiffer). The evolution of total outlet gas flowrate was also monitored and recorded using a gas flowmeter. The molar flowrates of each gas were calculated using the equation:

$$\dot{n}_i = f_T \frac{C_i}{100} \frac{10^6}{24.0548} \quad (4.2-1)$$

where \dot{n}_i is the calculated molar flowrate of each components i (i.e., C₂H₅OH, H₂, CH₄, CO, CO₂, H₂O) [μmol min⁻¹]. C_i is the gas concentration of each component i measured by QMS200 [mol%]. f_T is the total volumetric flowrate in the reactor outlet gas [Nml min⁻¹]. The factor of $\left(\frac{10^6}{24.0548}\right)$ is the conversion factor of gas volumetric

flowrate to molar flowrates at NTP - Normal Temperature and Pressure - condition [$\mu\text{mol Nml}^{-1}$]. The NTP condition is defined as air at 20°C (293.15 K) and 1 atm.

4.2.3.2. Reduction degree (RD) calculation

Characteristics of the ore structures and compositions before and after the reactions were analyzed using X-ray powder diffractometry (XRD; Miniflex, Rigaku). The reduction degree (RD) of each sample was then calculated using

$$RD = \frac{\text{mass of removed oxygen}}{\text{mass of removable oxygen}} \times 100\% \quad (4.2-2)$$

However, it was difficult to evaluate the exact amount of removed and removable oxygen because the presence of gangue materials such as SiO_2 , Al_2O_3 , and other oxides might be different within the ore samples. The RD of each sample was then calculated on the basis of the composition of iron oxides in the sample using

$$RD = \sum x_i RD_i \quad (4.2-3)$$

whereas x_i is the mass fraction of iron oxide component i ($i = \text{Fe}_2\text{O}_3, \text{Fe}_3\text{O}_4, \text{FeO}, \text{Fe},$ or Fe_3C) in the sample from the composition of oxide structure adapting the reference intensity ratio (RIR) methods. x_i is the weight fraction of component i according to the intensity of X-rays diffracted by a selected plane (hkl) of the component. RD_i is the reduction degree of the different iron structures, where RD_i of Fe_2O_3 , Fe_3O_4 , FeO , Fe , and Fe_3C are 0%, 11%, 30%, 100%, and 100%, respectively.

4.2.3.3. Carbon content calculation

The carbon content in the iron ore was calculated by the weight change of the iron ore after reduction in ethanol decomposition and after combustion at 1000 °C for 30 min under 500 ml min⁻¹ of air flow. Considering the reoxidation of reduced iron ore to hematite, the carbon content was calculated using

$$X_C = \left(1 - \frac{w_{sb}}{w_{sa}} \left(1 - \frac{23.99}{55.85} \frac{X_{FeO} X_{RD\alpha}}{(1-X_{CW})} \right) \right) \times 100\% \quad (4.2-4)$$

where X_C is the carbon content in the sample after a reduction in ethanol decomposition [mass%]. w_{sa} and w_{sb} are the sample weight after reduction under ethanol decomposition and after combustion in air flow, respectively [mg]. The factor of $\left(\frac{23.99}{55.85}\right)$ corresponds to the ratio of the stoichiometric mass equivalent of oxygen to Fe in Fe₂O₃ structure (calculated as FeO_{1.5}). X_{FeO} and X_{CW} are the mass fraction of total Fe and the combined water (CW) content in raw material, respectively [-]. $X_{RD\alpha}$ is the mass fraction of the reduction degree (RD) of the sample after a reduction in ethanol decomposition [-].

4.2.4. Kinetic analysis

4.2.4.1. Reactions mechanisms in the gas-solid system

Ethanol vapor decomposed rapidly in the presence of iron ore means that the catalytic reaction of ethanol decomposition occurs. Simultaneously, the Fe₂O₃ changes to metallic-Fe, reduction occurs. In this approach, there are eight main reactions involved, (1) Decomposition of ethanol; (2) Decomposition of methane; (3) Steam reforming of methane; (4) Water gas shift reaction; (5) Boudouard reaction; (6) Iron reduction by carbon; (7) Iron reduction by CO; (8) Iron reduction by H₂. The kinetic equations with

the second order reaction at each reaction in term of generation of component j is expressed as in Eq. 4.2-5.

$$r_j = k_{Overall\ i} n_j n_k \quad (4.2-5)$$

The mechanisms of ethanol decomposition in gas-solid reaction systems can be evaluated as depicted in Fig. 3. The mechanism includes the mass transfers of both reactants and products, in term of external diffusion and internal diffusion in the pore, the adsorption/desorption into the pore surface, and the surface reactions.

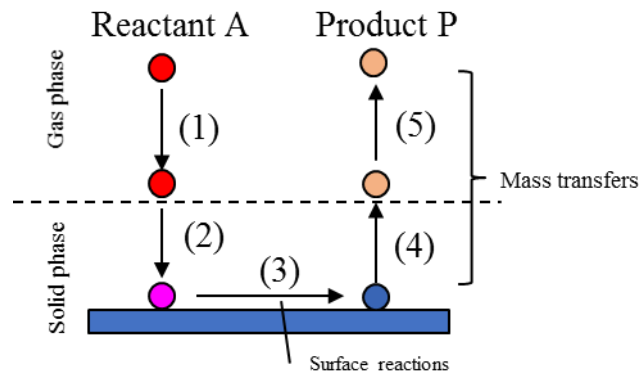


Figure 4.2.1 Simplified reaction pathway of ethanol decomposition over the surface of iron ore. (1) Mass transfers of reactants in term of external diffusion and internal diffusion in pore; (2) Mass transfers of reactant adsorption; (3) Surface reaction of adsorbed phase; (4) Mass transfer of product desorption; and (5) Mass transfer of product in term external diffusion and internal diffusion in the pore.

In overall terms, introducing a resistance concept in reaction model would simplify the overall kinetic term as in Eq. 4.2-6.

$$\frac{1}{k_{Overall\ i}} = \frac{1}{k_{di}} + \frac{1}{k_{ri}} \quad (4.2-6)$$

Where $k_{i\ overall}$ is the overall rate coefficient in bulk reaction i , k_{di} is rate coefficients of mass transfer including external diffusion and internal diffusion in the pore, k_{ri} is rate coefficients of reactions (surface reaction). Mass transfer phenomena of gases into pore including internal and external diffusion are evaluated by the coefficient

of apparent mass transfer rate effect on overall kinetic C_{dj} , for each component j . Thus, the overall kinetic term should be

$$k_{Overall\ i} = C_{dj}k_{ri} \quad \text{with } C_{dj} = \left(\frac{k_{di}}{k_{di}+k_{ri}} \right)_j \quad (4.2-7)$$

Some assumptions were taken into consideration: (1) C_{dj} was assumed as a constant. (2) Since the iron ore bed (0.3 g) in the reactor (ID = 6 mm; H = 7 mm) is quite small, and with a preliminary experiment confirming the temperature is uniform at any axial position around bed position. In other meaning, reactions were assumed uniform at any positions in bed. (3) The reduction of FeO_x are considered as an oxygen removal of from iron oxide (i.e. $FeO_x + xC \rightarrow Fe + xCO$ with $x = 1.5$ for hematite). This reaction can be simplified as $RO_{(s)} + C_{(s)} \rightarrow CO_{(g)}$.

In the complex system, the overall rate generation of component j can be expressed

$$r_j = C_{dj} \sum k_{ri} n_j n_k \quad (4.2-8)$$

An Arrhenius-type overall kinetic equation was used to model k_{ri} expressing

$$k_{ri} = k_{fr0i} \exp \left(-\frac{E_{ai}}{R} \left(\frac{1}{T} - \frac{1}{T_0} \right) \right) \quad (4.2-9)$$

whereas k_{fr0i} is the rate coefficient of forward reaction i at T_0 [$mol^{-1} s^{-1}$]; E_{ai} is the activation energy of reaction i [$J mol^{-1}$]; K_{0i} is the equilibrium constant of reaction i at T_0 [-]; ΔH_{ri} is the enthalpy of reaction i [$J mol^{-1}$]; R is the ideal gas constant [$=8.314 J mol^{-1}K^{-1}$]; T, T_0 are temperature [K] and the reference temperature [K], respectively; and β is heating rate [i.e., 10 K/min]. The term of $\left(\frac{1}{T} - \frac{1}{T_0} \right)$ in the overall kinetic equation was introduced to improve the independency of each parameter during curve fitting.

Applying a transient thermal state with a heating rate $\beta = \frac{dT}{dt}$, the mole balance of each components j can be expressed below

$$\frac{dn_j}{dT} = \frac{1}{\beta} (\dot{n}_{j0} + C_{dj} \sum k_{ri} n_j n_k) \quad (4.2-10)$$

With i is the reaction number (1~8). j, k are the components indices related to reaction i (e.g., RO, C, CO, CO₂, H₂, H₂O, CH₄, C₂H₅OH), respectively. n_j, n_k are the amounts of components j and k [mol]. \dot{n}_{j0} is the molar flowrate of gas entering the reactor. In the case of ethanol, $\dot{n}_{C_2H_5OH}^0$ is 686 mol min⁻¹, while for other product gases, the $\dot{n}_{j0} = 0$, respectively.

4.2.4.2. Curve fitting procedures

Therefore, as in Eq. (4.10), 24 parameters are estimated, consists of eight kinetics constants of reactions at $T_0 (= 1073 \text{ K})$, $kfr_{10} \sim kfr_{80}$, eight activation energies, $E_1 \sim E_8$, and eight coefficients of the mass transfer effect, $C_{dA} \sim C_{dH}$. These parameters were estimated by a curve fitting method using the sum square error (SSE) as the objective function. Since SSE should be not containing any units. Thus, the unitless SSE was introduced in the fitting as in Eq. 4.2-11.

$$\overline{SSE} = \sum \left(\frac{n_{j_{calc}} - n_{j_{data}}}{n_{j_{data}}} \right)^2 \quad (4.2-11)$$

Numerical solution for Eq. (4.2-10) was performed in MATLAB®. Numerical integration for simultaneous ordinary differential equation of Eq. (4.2-10) was calculated using "ode15s" function. Curve fitting was performed by running an optimization program to minimize the \overline{SSE} value of 100 data points in eq. (4.2-10) using "lsqnonlin" function with iteration parameters "TolX" = 1e-10; "TolFun" = 1e-10; "MaxIter" = 8000;

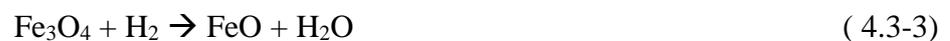
"MaxFunEvals" = 10000. Initial guess value of the parameter $k_{10} \sim k_{80}$, $E_1 \sim E_8$, $C_{dA} \sim C_{dH}$, were 10^{-3} , 10^5 , and 0.5, respectively. Lower boundary for all parameters were set as zero. The goodness of fit using R^2 were also calculated.

4.3. Results and Discussions

Temperature-programmed reduction (TPR) is a technique for the characterization of solid materials and is often used in the field of heterogeneous catalysis to find the most efficient reduction conditions [7]. An oxidized catalyst precursor is submitted to a programmed temperature rise while a reducing gas mixture flows over it. Figure 4.3.1 shows simultaneous ethanol decomposition with iron reduction reaction. Data was reorganized to find a correlation between kinetic activity and oxide structure in the ore. These data can be interpreted briefly that significant ethanol decomposition is started at 300 °C, together with iron reduction by CO.



At 400 °C, Iron reduction by H₂ is started:



At 600 ~ 700 °C, Ethanol decomposition seems slower when iron ore structure change from Fe₃O₄ to FeO. Above 700 °C, Significant iron reduction by deposited-C is started:



Experimental conditions:

Fuel: 0.04 ml/min of ethanol; Ore: 0.3g of DH300 goethite ore

Argon flowrate: 100 Nml/min; Temp: 25-900°C, 10 K/min

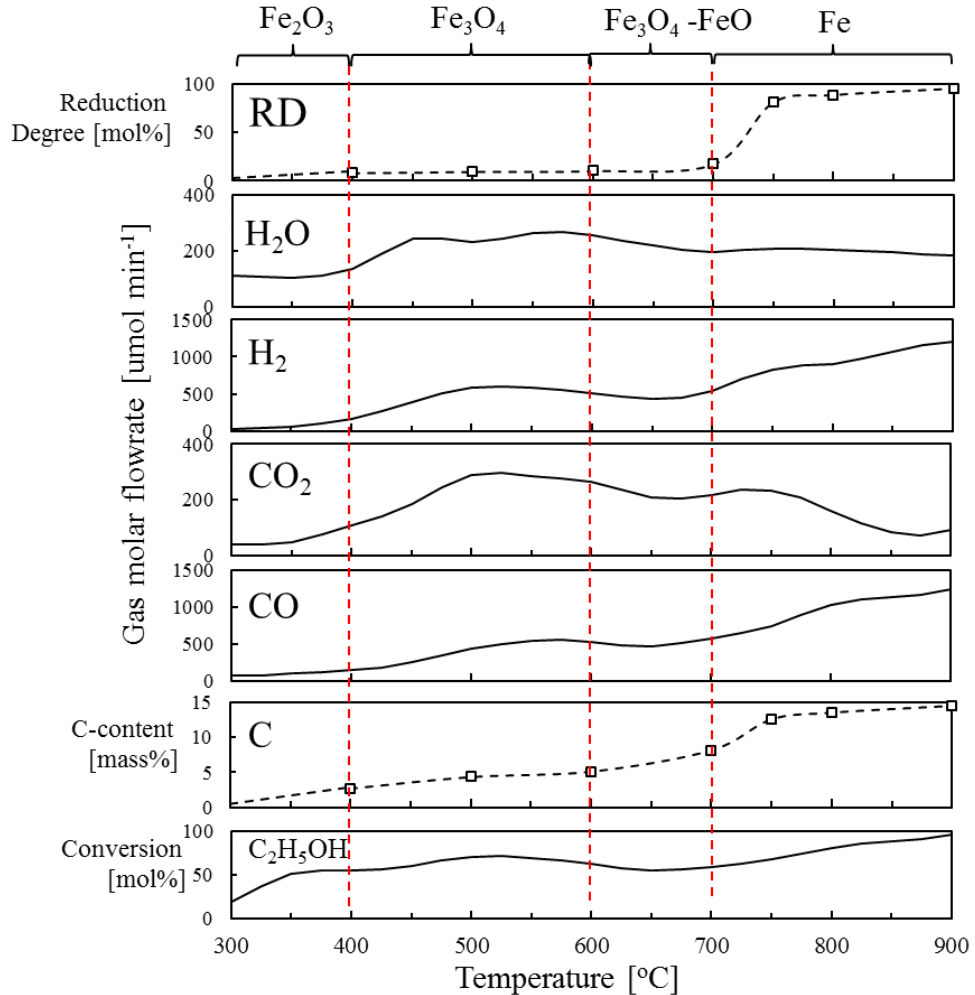


Figure 4.3.1 Simultaneous ethanol decomposition-iron reduction of dehydrated goethite ore in [1].

By calibrating them into gas concentration data and then multiplying them with total flowrate data using equation (4.1), the gas flowrate data were obtained in the expression of the mole amount per time unit (e.g., in a unit of mol min⁻¹). Meanwhile, RO and carbon contents in the ore are evaluated after the reactor reached the specific temperatures. The samples were taken out to be analyzed. The RO and carbon content are expressed as the accumulated amount (i.e., in a unit of mol). To have the same unit

order of all measured amount for curve fitting, the molar flowrate data of generated gases j were reformed into the accumulated molar amount of gas using the equation below

$$n_{j,T_i}^{acc} = n_{j,T_{i-1}}^{acc} + \sum_{i=2}^i \frac{T_i + T_{i-1}}{2\beta} (\dot{n}_{j,T_i} + \dot{n}_{j,T_{i-1}}) \quad \text{with } i = \text{index of data point} \quad (4.3-5)$$

The gas data were reformed into the accumulated amount. Fig. 4.3.2 shows the accumulated amount of ethanol and gas generated from ethanol decomposition over iron ore.

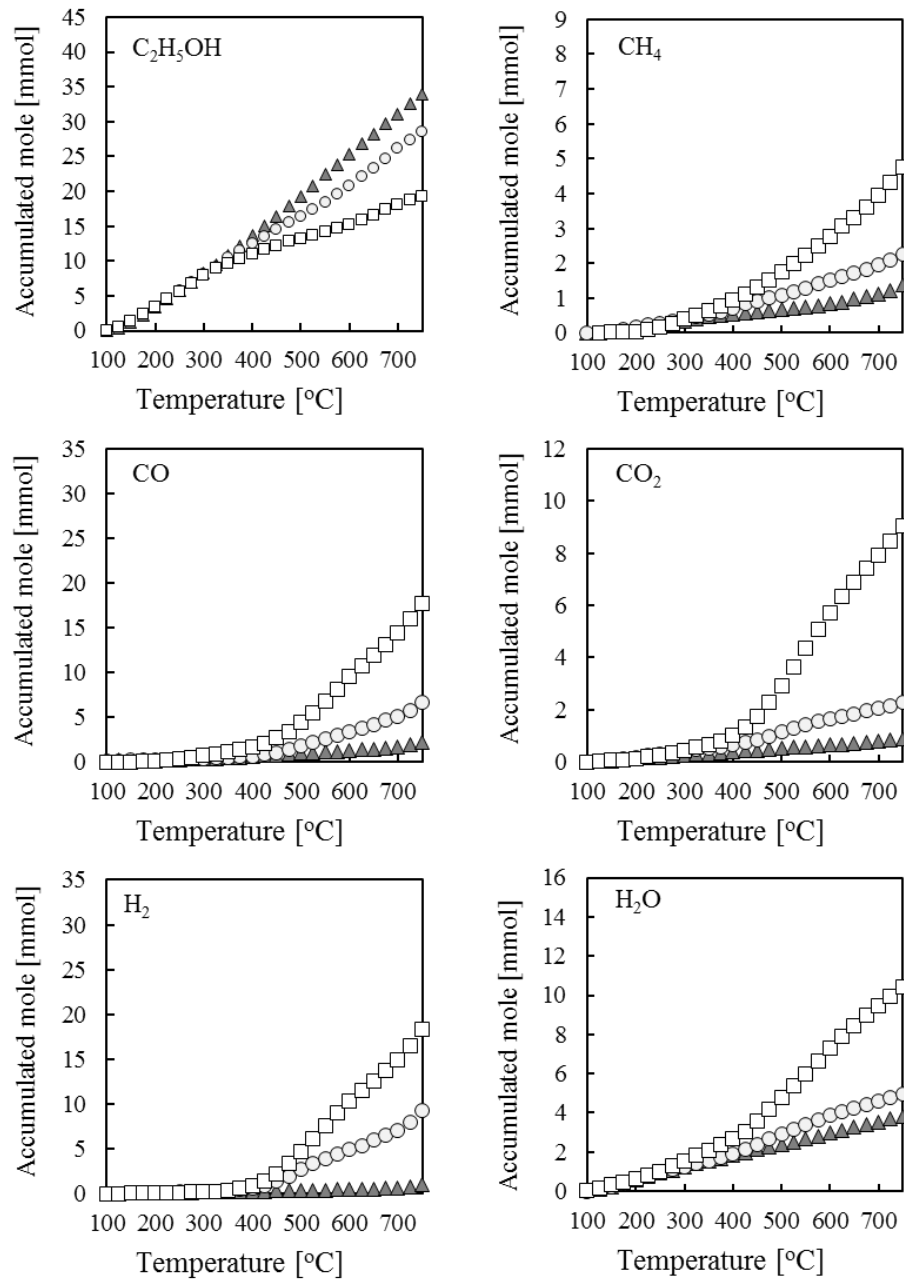


Figure 4.3.2 Accumulated gas data

4.3.1. Curve fitting results: k_0 , E_a , and C_d

Figure 4.3.3 shows the curve fitting result of each component with the goodness of fitting (R^2) also calculated.

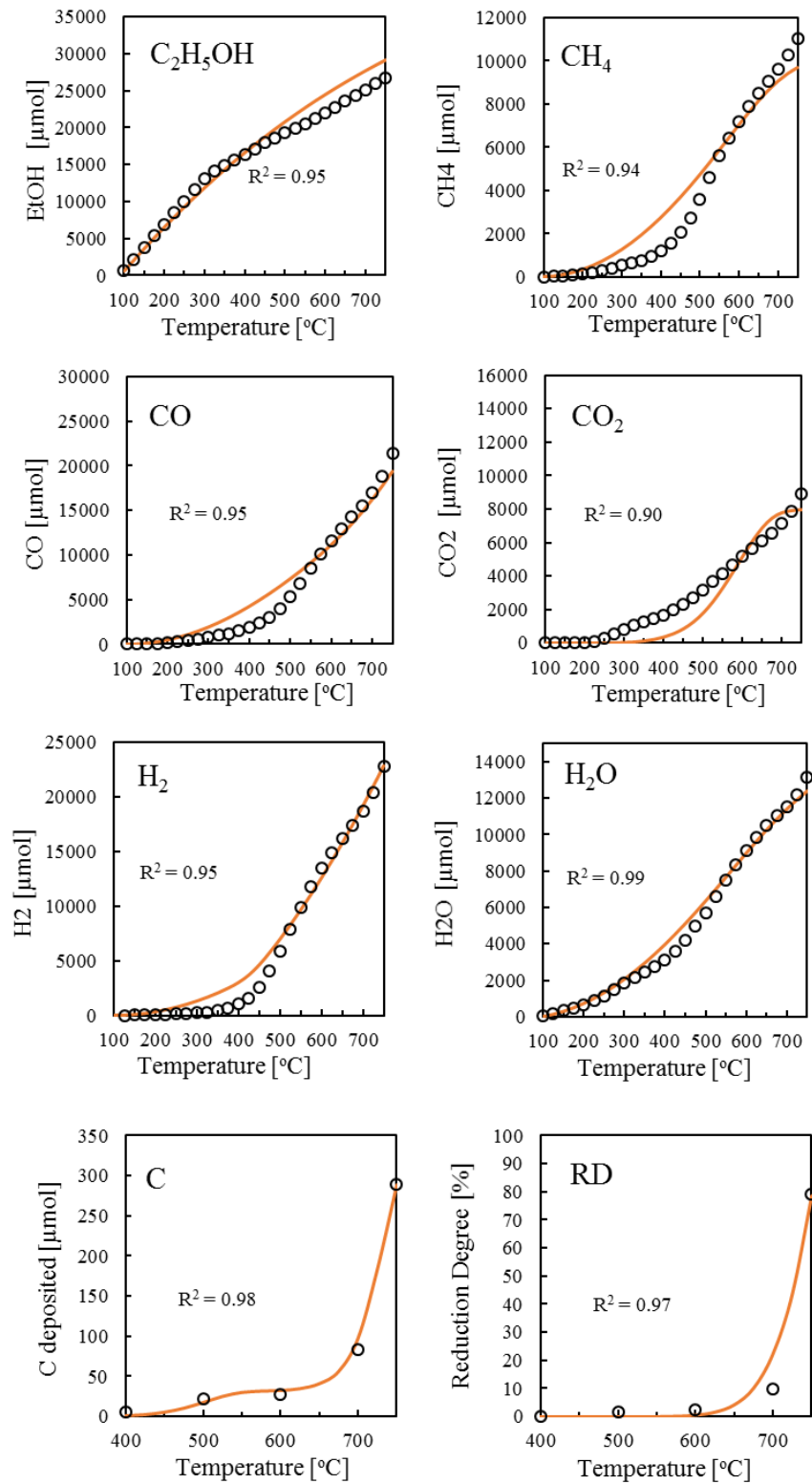


Figure 4.3.3 Curve fitting results. The R² closes to 1 means the model is almost perfectly fitted to experimental data. The model is satisfactorily fit to the data for H₂O, C, RD, CO, H₂, and C₂H₅OH. However, it was quite fit to CH₄ and CO₂.

Table 4.3.1 Obtained parameters of reaction kinetic from curve fittings

No	Reactions	Obtained parameters		Comparison to references	
		k_{froi} [1/min.mol]	E_{ai} [kJ/mol]	E_{ai} [kJ/mol]	References
1	Decomposition of ethanol: $C_2H_5OH_{(g)} \rightarrow CH_4_{(g)} + H_2O_{(g)}$ + C	0.346	1.77	1.87~16.8	[8]
2	Decomposition of methane: $CH_4_{(g)} \rightarrow C_{(s)} + 2H_2_{(g)}$	0.199	25.23	60	[9]
3	Steam reforming: $CH_4_{(g)} + H_2O_{(g)} \rightarrow CO_{(g)} + 3H_2_{(g)}$	0.747	127.05	169.5	[10]
4	Water gas shift reaction $CO_{(g)} + H_2O_{(g)} \rightarrow CO_2_{(g)} + H_2_{(g)}$	1.41	51.65	45	[11]
5	Boudouard reactions: $C_{(s)} + CO_2_{(g)} \rightarrow 2CO_{(g)}$	1.82E-09	123.02	120~310	[12]
6	Iron reduction by Carbon: $FeO_{x(s)} + xC_{(s)} \rightarrow Fe_{(s)} + xCO_{(g)}$; x=1.5	0.051	139.24	280	[13]
7	Iron reduction by CO: $FeO_{x(s)} + xCO_{(g)} \rightarrow Fe_{(s)} + xCO_2_{(g)}$; x=1.5	1.35×10^{-3}	118.91	116~151	[14]
8	Iron reduction by H ₂ : $FeO_{x(s)} + xH_2_{(g)} \rightarrow Fe_{(s)} + H_2O_{(g)}$; x=1.5	6.83×10^{-4}	99.68	61.5~71	[15]

4.3.2. Interpretation of parameter C_{dj}

Table 4.3.2 shows the obtained parameters of C_{dj} from the curve fittings. The parameter of C_{dj} was introduced to compensate for the unknown effect of particle size, surface area, etc. as well as mass transfer effect through simultaneous surface reaction occurs. C_{dj} in this term correlates with the mass transfer properties of each reacted component. C_{dj} could be also introduced as Thiele modulus describing the relationship between diffusion and reaction rate in porous ore with no mass transfer limitations. This value is generally used in determining the effectiveness factor for catalyst pellets. This approach is set according to some assumptions. (1) Diffusion through a surface film is

very fast compared to diffusion into the grain interior. This is usually a safe assumption since surface films are normally very thin. (2) The pores in the catalyst grain are interconnecting, and the diffusion of reacting gases and products takes place through these pores and not through the solid catalyst [16].

Table 4.3.2 Obtained parameters of C_{dj} from the curve fitting result

Components, j	Obtained C_{dj}	Thiele modulus, $\varphi \approx \frac{(1-C_{dj})}{C_{dj}}$	Interpretation: Overall generation of component j is controlled by
RO	0.8662	0.15	Diffusion
H ₂ O	0.6707	0.49	Diffusion
CO	0.6083	0.64	Diffusion
C	0.2046	3.89	Surface reaction
C ₂ H ₅ OH	0.0437	21.89	Surface reaction
CH ₄	0.0403	23.84	Surface reaction
H ₂	0.0236	41.43	Surface reaction
CO ₂	47.34	47.34	Surface reaction

Interpretation on obtained parameters of C_{dj} shows that the reaction of gases inside pore might be inhibited by carbon deposition on the surface of iron ore.

SEM-EDS cross-section analysis of porous iron ore reduced by ethanol show that the carbon was deposited inside ore (Figure 4.3.4) TEM images also show that amorphous deposited carbon covering the iron surface as depicted in Figure 4.3.5. This could be interpreted that ethanol is infiltrated into the iron ore pore and simultaneously decomposed to deposited carbon and reducing gas CO and H₂. The generated reducing agents then reduce the iron oxides to metallic-Fe. It was agreed that the nano-contact of reducing agent with iron ore promotes higher reaction rate of iron ore reduction as well reported in [6] for the case of carbon composite ore. However, the process might be different, since the reducing agent is not only carbon but also involving H₂ and CO

reduction as well. The reduction under ethanol only reaches 81% of RD at 1023 K is because of pore was already cover by carbon.

Dehydrated GE ore after reduction

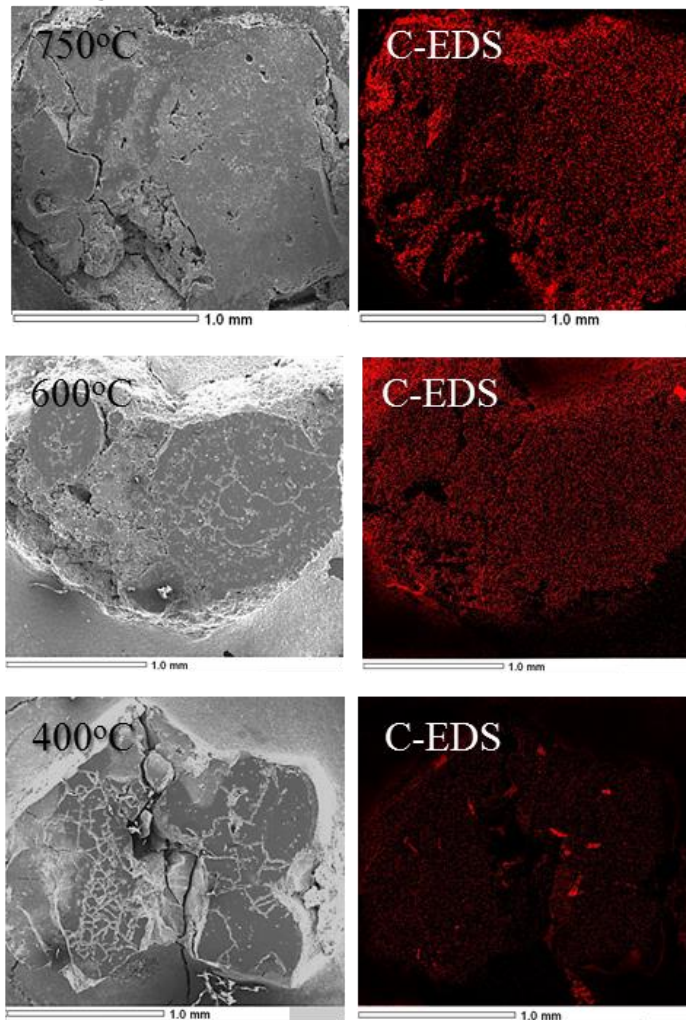


Figure 4.3.4 SEM-EDS cross-section analysis for carbon mapping of dehydrated iron ore reduced by ethanol. (Red means carbon)

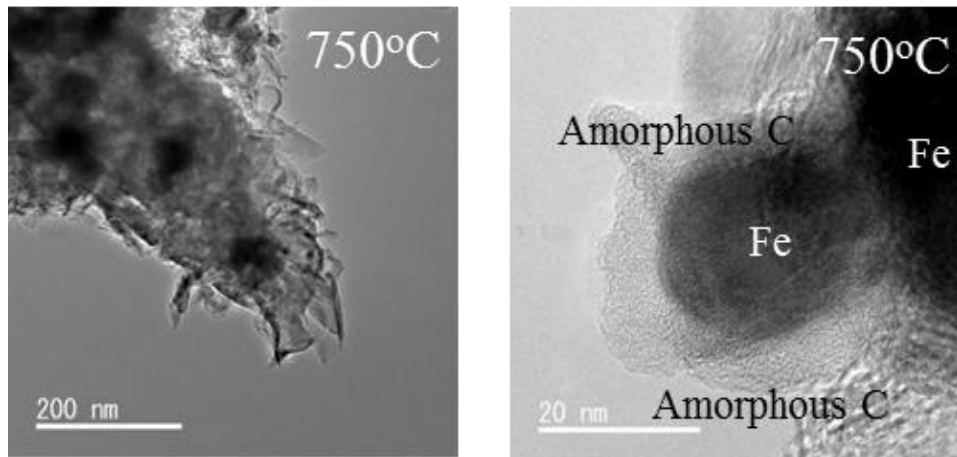


Figure 4.3.5 TEM images of dehydrated GE ore after reduced by ethanol.

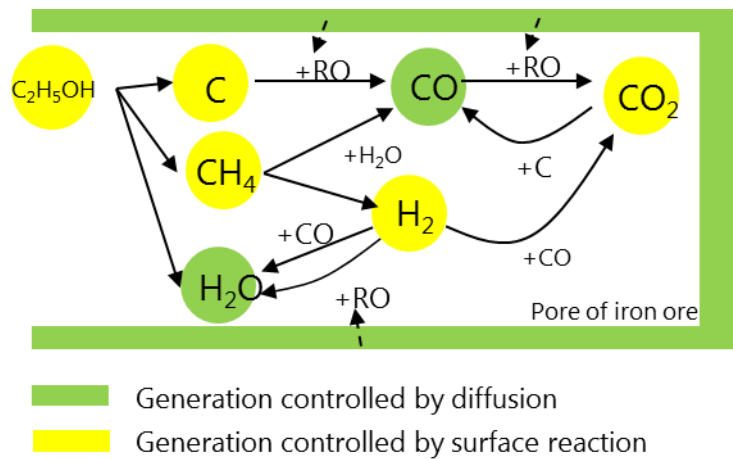


Figure 4.3.6 Schematic reaction mechanism of ethanol decomposition and iron reduction

4.4. Conclusions

1. The kinetic study is necessary for understanding the mechanism of the simultaneous ethanol decomposition – iron reduction process.
2. There were 8 main reactions involved: decomposition of ethanol, decomposition of methane, steam reforming of methane, water gas shift, Boudouard reactions, iron reduction by C, iron oxide reduction by CO and iron reduction by H₂

3. Curve fitting methods were conducted with satisfying results ($R^2 > 0.90$) calculating 24 parameters consisting k_{froi} , E_{ai} , and C_{dj} .
4. Interpretation on obtained parameters of C_{dj} shows that the reaction of gases inside pore might be inhibited by carbon deposition on the pore surface of iron ore.

References

- [1] Kurniawan, A., Abe, K., Ohashi, K., Nomura, T. and Akiyama, T., 2018. Reduction of mild-dehydrated, low-grade iron ore by ethanol. *Fuel Processing Technology*, 178, pp.156-165.
- [2] Balat, M. and Balat, H., 2009. Recent trends in global production and utilization of bio-ethanol fuel. *Applied energy*, 86(11), pp.2273-2282.
- [3] Chen, H. and Qiu, W., 2010. Key technologies for bioethanol production from lignocellulose. *Biotechnology Advances*, 28(5), pp.556-562.
- [4] Ou, X., Zhang, X., Zhang, Q. and Zhang, X., 2013. Life-cycle analysis of energy use and greenhouse gas emissions of gas-to-liquid fuel pathway from steel mill off-gas in China by the LanzaTech process. *Frontiers in Energy*, 7(3), pp.263-270.
- [5] Kashiwaya, Y. and Akiyama, T., 2010. Nanocrack formation in hematite through the dehydration of goethite and the carbon infiltration from biotar. *Journal of Nanomaterials*, 2010, p.18.
- [6] Hosokai, S., Matsui, K., Okinaka, N., Ohno, K.I., Shimizu, M. and Akiyama, T., 2012. Kinetic study on the reduction reaction of biomass-tar-infiltrated iron ore. *Energy & Fuels*, 26(12), pp.7274-7279.
- [7] Jones, A., 2014. *Temperature-Programmed Reduction for Solid Materials Characterization*. CRC Press.

- [8] Sun, J., Qiu, X.P., Wu, F. and Zhu, W.T., 2005. H₂ from steam reforming of ethanol at low temperature over Ni/Y₂O₃, Ni/La₂O₃ and Ni/Al₂O₃ catalysts for fuel-cell application. *International Journal of Hydrogen Energy*, 30(4), pp.437-445.
- [9] Sharif Zein, S.H., Mohamed, A.R. and Talpa Sai, P.S., 2004. Kinetic studies on catalytic decomposition of methane to hydrogen and carbon over Ni/TiO₂ catalyst. *Industrial & engineering chemistry research*, 43(16), pp.4864-4870.
- [10] Tonkovich, A.L., Qiu, D., Dritz, T.A., Neagle, P., Litt, R.D., Arora, R., Lamont, M.J. and Pagnotto, K.M., Velocys Inc, 2007. Process for separating nitrogen from methane using microchannel process technology. U.S. Patent 7,250,074.
- [11] Van der Laan, G.P. and Beenackers, A.A., 2000. Intrinsic kinetics of the gas–solid Fischer–Tropsch and water gas shift reactions over a precipitated iron catalyst. *Applied Catalysis A: General*, 193(1-2), pp.39-53.
- [12] Ye, D.P., Agnew, J.B. and Zhang, D.K., 1998. Gasification of a South Australian low-rank coal with carbon dioxide and steam: kinetics and reactivity studies. *Fuel*, 77(11), pp.1209-1219.
- [13] Iguchi, Y., Endo, S. and yokomoto, s., 2004. Direct and indirect reduction and carburization of reduced iron in iron ore-carbon composite pellets heated at elevated temperatures. In 2nd international meeting on ironmaking and the 1st international symposium on iron ore (pp. 531-540).
- [14] Trushenski, S.P., Li, K. and Philbrook, W.O., 1974. Non-topochemical reduction of iron oxides. *Metallurgical transactions*, 5(5), pp.1149-1158.
- [15] Sun, S. and Lu, W.K., 1999. A theoretical investigation of kinetics and mechanisms of iron ore reduction in an ore/coal composite. *ISIJ international*, 39(2), pp.123-129.
- [16] Thiele, E.W., 1939. Relation between catalytic activity and size of particle. *Industrial & Engineering Chemistry*, 31(7), pp.916-920.

CHAPTER V

SYSTEM EVALUATION OF ETHANOL-ASSISTED IRONMAKING:

EXERGY AND CO₂ EMISSION ANALYSIS

5.1. Introduction

World crude steel production reached 1,691 million tonnes (Mt) in 2017. By 2050, steel use is projected to increase by 1.5 times that of present levels, to meet the needs of our growing population [1]. The iron and steelmaking industry is one of the most energy-intensive industries in the world and consumes 19.5 EJ/year, which constitutes around 5% of the total global energy consumption [2]. The amount of energy consumed in the production of steel depends on the process used, and it constitutes a significant portion of the cost of steel production, from 20% to 40%. Thus, improvements in energy efficiency are necessary to reduce production costs and thereby improve competitiveness [3]. In the blast furnace process, iron ore is reduced (meaning that oxygen molecules in the ore bond with the carbon molecules), leaving pure molten iron and carbon dioxide. The molten iron is transferred to a basic oxygen furnace, where super-heated oxygen is used to remove any remaining impurities. Coal consumption and heat generation make the process highly energy intensive. In addition, the process requires metallurgical coal (coking coal), which is costlier than steam coal because of its lower ash and sulfur content [4].

The primary energy source is fossil fuels, and such ironmaking is one of the most significant contributors to CO₂ emissions, 6.7% of the total global emissions [5]. Several programs have been initiated worldwide to reduce fossil fuel utilization and CO₂ emissions, such as ULCOS in the EU, COURSE50 in Japan, and AISI in the USA [6]. In

addition, a simple way to resolve emission concerns is to use biomass resources in the ironmaking industry [7].

Ethanol, is counted as carbon-free fuel if it is derived from biomass, is attractive as ironmaking fuel [8]. Ethanol is one of promising fuel candidate to initiate hydrogen-based ironmaking. In Table 5.1.1, ethanol was placed as among the high exergetic fuel for ironmaking. Attribute to decomposition producing H₂ and CO; ethanol is attractive to minimize the exergy loses within ironmaking. However, the recent production of ethanol is only to accommodate transportation fuel. New business should be considered in utilizing ethanol for ironmaking purpose.

In the other hand, the effective utilization of low-grade ores such as goethite, FeOOH, in the modern ironmaking industry is highly required to solve the problems related to the depletion and shortages of high-grade iron ores. The drawback of low-grade ores containing goethite as a raw material is the presence of a large amount of combined water (CW) in the ores, which necessitates additional energy for the dehydration process. However, it has been reported that the dehydration of goethite at 623 K with a heating rate of 3 K/min in the air creates micropores ranging from 2 to 4 nm in size and a BET specific surface area as high as 70 m²/g [9]. Because of these, an iron ore/carbon composite (IOC) had been proposed by introducing carbonaceous material into the pores to enhance the reduction rate of iron ore [10]. The reduction rate of an iron ore composite sample prepared using FeOOH reagent, and thermoplastic carbon resin is dramatically enhanced and proceeds at temperatures as low as 973 K.

Table 5.1.1 Standard Chemical Exergy, ϵ^0 ($T = 298.15\text{ K}$, $p = 101.325\text{ kPa}$) of some material as ironmaking fuel.

Substance (phase)	Name	MW [kg/kmol]	H-density and {C-density}		Standard chemical exergy, ϵ^0	
			[mole%]	[mass%]	[MJ/kmol]	[MJ/kg]
H₂(g)	Hydrogen	2.02	100 {0}	100 {0}	236.1	118.1
CH₄(g)	Methane	16.04	80 {20}	25 {75}	831.2	52.0
C₄H₉OH(l)	Butanol	74.12	66.7{26.7}	13.4{64.8}	2712.8	36.6
C_(s)(graphite)	Coke, Graphite	12.01	0 {100}	0 {100}	409.9	34.2
C₂H₅OH(l)	Ethanol	46.07	66.7{22.2}	13 {52.2}	1356.9	29.5
CH₃OH(l)	Methanol	32.04	66.7{16.7}	12.5{37.5}	756.1	23.6
NH₃(g)	Ammonia	17.03	75 {0}	17.6 {0}	337.9	19.9
C₃H₈O₃(l)	Glycerin	92.09	57.1{21.4}	8.7{39.1}	1762.6	19.2
C₆H₁₂O₆(s)	Sugar (Glucose)	180.16	50 {25}	6.7 {40}	3091.6	17.2
CO(NH₂)₂(s)	Urea	60.06	80 {12.5}	6.7 {20}	688.6	11.5
CO(g)	Carbon Monoxide	28.01	0 {50}	0 {42.8}	274.7	9.8

Our proposed process for ethanol-assisted ironmaking can be seen in Fig 5.1.1., in which 4 processes are needed. Process 1 is goethite ore dehydration. This mild-dehydration is conducted in low-temperature heating. As Genki et al. suggested in [11], the dehydration temperature of 573 K is enough for dehydrating the CW producing nanoporous hematite ore. Process 2 is ethanol-assisted reduction furnace. Ethanol is charged into a reduction furnace, allowing the iron ore reduction in a lower temperature. Process 3 is the melting furnace, separation of slag and melting iron occurs in the furnace. And process 4 is the ethanol recovery from gas generated from process 2 and 3.

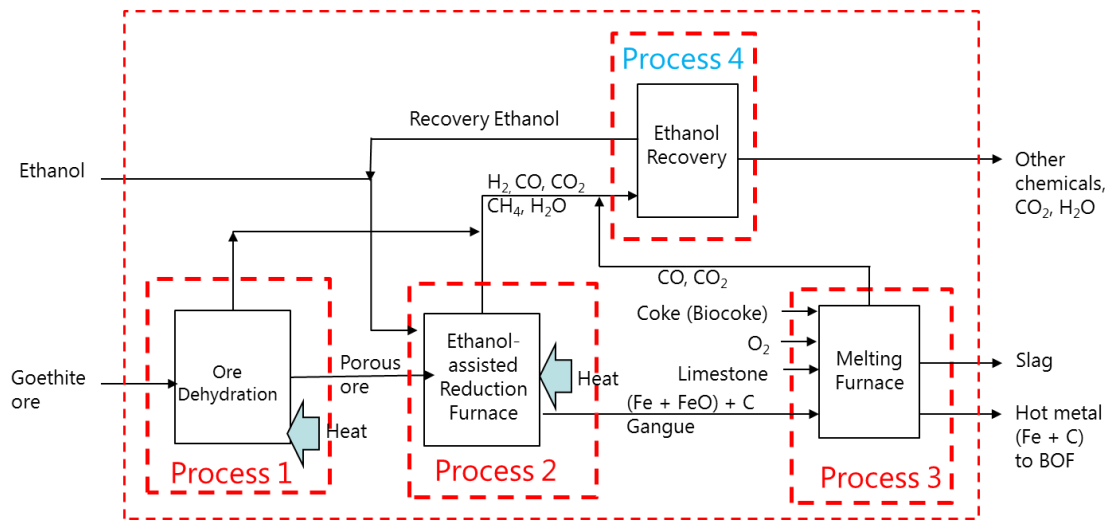


Figure 5.1.1 The proposed integrated system of ethanol-assisted ironmaking with ethanol recovery.

A specific analysis method was required to understand the energy efficiency and complexity of the proposed method. Exergy analysis based on the second law of thermodynamics is one best method to assess the energy efficiency of the proposed method and to compare it with existing systems [12]. The exergy analysis is better than an enthalpy balance or a heat balance because exergy can express the quality of energy and evaluate different forms of energy like chemical, thermal, pressure and mixing energy by a unified measure [13]. It is found to be the best tool of the cycle optimization for given input information [14].

Therefore, an exergy analysis was performed using the developed process system diagram to evaluate the advantages of the proposed method over conventional methods. In this chapter, two proposed systems of ethanol assisted ironmaking were compared to the conventional ironmaking blast furnace and direct reduction process.

5.2. Analysis method

5.2.1. Exergy analysis

The concept of exergy was developed by J. Willard Gibbs in 1878. It was further developed by Zoran Rant in 1957. In 1965, H. D. Baehr termed the part of the energy that is converted into all other forms of energy as exergy. Exergy is based on the second law of thermodynamics and the concept of irreversible production of entropy [15], [16], [17]. It is a useful work potential of energy. Exergy analysis helps in finding the losses taking place in a system. By this method, energy conversion at different points, various component efficiencies and points of most substantial losses are easily obtainable, and hence it helps in taking necessary action to decrease them [18].

As a similar calculation method that in [19], exergy evaluation describes the thermodynamic change from the available energy to the unusable one in the form of work. On the term related to the change of enthalpy and entropy, exergy, itself, is defined as follow:

$$\varepsilon = H - H_0 - T_0(S - S_0) \quad (5.2-1)$$

Exergy consists of chemical and physical exergy terms. On both terms, exergy can be expressed as follow:

$$\varepsilon = \varepsilon_C + \varepsilon_T + \varepsilon_P + \varepsilon_M \quad (5.2-2)$$

where ε_C is the standard chemical exergy equal to e_C . In contrast, ε_T , ε_P and ε_M are related to temperature, pressure and mixing exergies, respectively. They are expressed as:

$$\varepsilon_C = \sum n_i \varepsilon_{Ci}^0 \quad (5.2-3)$$

$$\varepsilon_T = (\sum n_i C_{Pi}) \left[T - T_0 - T_0 \ln \left(\frac{T}{T_0} \right) \right] \quad (5.2-4)$$

$$\varepsilon_P = (\sum n_i) RT_0 \sum \left[\ln \left(\frac{P}{P_0} \right) - \left(1 - \frac{P_0}{P} \right) \right] \quad (5.2-5)$$

$$\varepsilon_M = RT_0 \sum \left[n_i \ln \left(\frac{n_i}{\sum n_i} \right) \right] \quad (5.2-6)$$

The exergy loss (EXL) was calculated as the difference between the exergy of the input material (ε_{in}) and that of the output material (ε_{out}) in each unit of the system. The reference chemical exergy (ε_{Ci}^0) was described as the chemical exergy of each substance at 298 K and 1 atm calculated based on the Gibbs free energy.

The exergy can be calculated for all substances in various states. Many different forms of substances and types of energies are considered in the system. Therefore, the concept of exergy is beneficial for evaluating the energy efficiency of a system. The exergy loss (EXL) in a process can be calculated by the following equation:

$$EXL = \varepsilon_{in} - \varepsilon_{out} = \varepsilon_{diff} - \varepsilon_{diss} \quad (5.2-7)$$

where ε_{in} , ε_{out} , ε_{diff} , and ε_{diss} denote the exergy inflow of a system, exergy outflow of the system, diffusion exergy that is lost outside the system and dissipation exergy resulting from an irreversible reaction, respectively.

5.2.2. Process design and evaluation

There are two cases in the current study proposing the ethanol-assisted ironmaking: case one is without ethanol recovery and case two is coupled with ethanol recovery, as presented in Figure 5.2.1. The boundaries were set only for ironmaking

process only, in which the process includes from the dehydration of goethite ore, reduction by ethanol, until hot metal-slag separation.

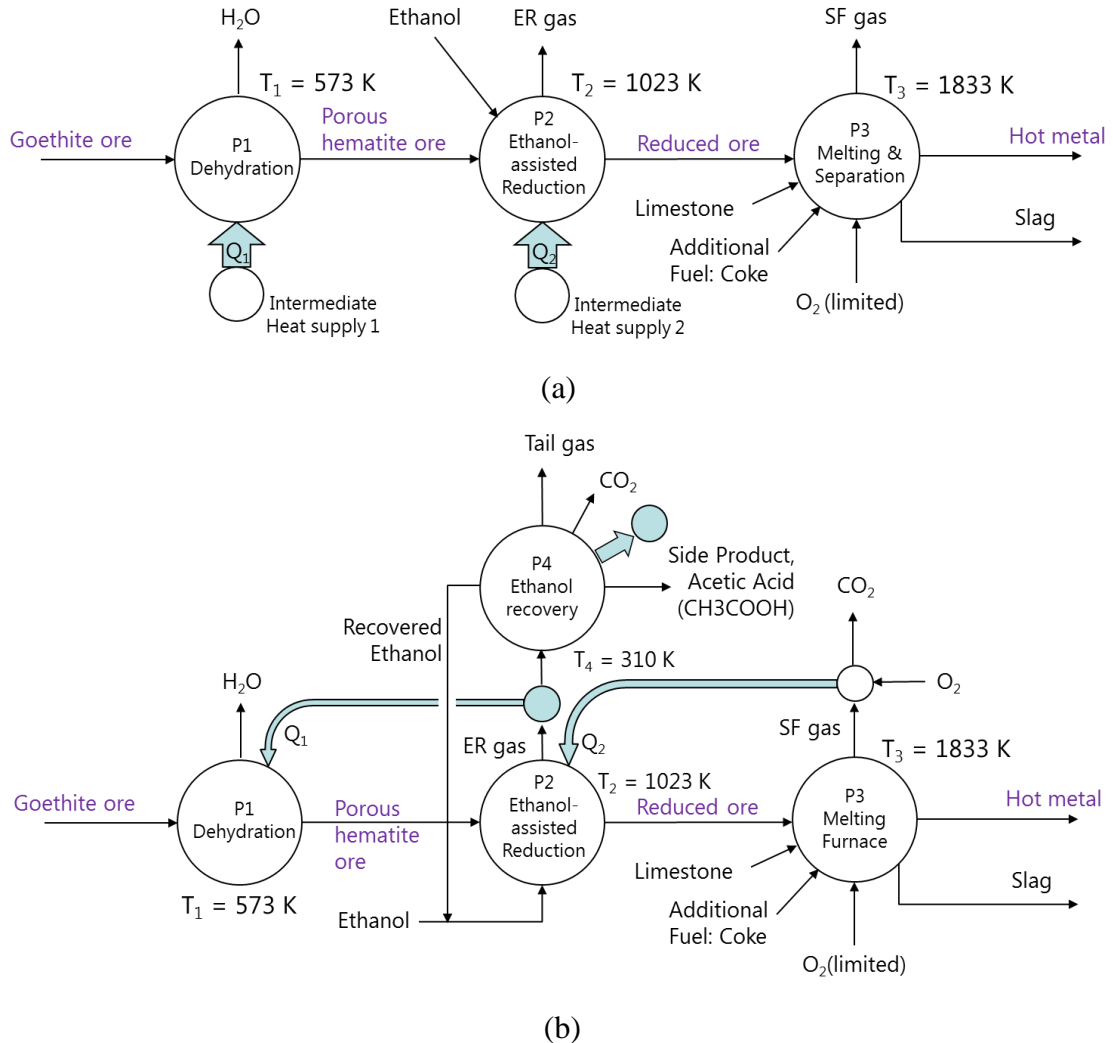


Figure 5.2.1 Process design schemes of ethanol-assisted ironmaking. (a) Case 1: without ethanol recovery, and (b) Case 2: coupled with ethanol recovery.

The exergy calculations were made based on the following steps and assumptions:

1. The overall process system of ethanol-assisted ironmaking to be analyzed were split into 4 sub-processes. Process 1: Goethite mild-dehydration is set at 573 K with intermediate heat, Q₁, is supplied additionally from another process. Process 2: Ethanol is introduced to perform primary reduction at 1023 K with the reduction degree (RD) up to 81%. The reduction degree was considered from the experimental

data of [8]. Intermediate heat supply, Q_2 , is also considered. Process 3: to extend the RD up to 100%, the additional furnace is needed as well as to separate hot metal and slag. Limestone is introduced as flux. Additional fuel as coke is required to increase the temperature up to 1833 K.

2. On the case two (Figure 5.2.1(b)), process 4 is introduced as ethanol recovery by utilizing the waste gas from process 2. The ethanol recovery process is considered through a gas fermentation process [20].
3. Assumptions:
 - Overall mass balance was developed based on 1000 kg-hot metal on the process 3.
 - Gangue material is taken into consideration as 30wt% of raw goethite ore input in the presence of SiO_2 and Al_2O_3 .
 - The adiabatic condition was approached, as an ideal fully isolated system with no heat loss.
 - Additional intermediate heats were calculated from heat balance on the corresponding sub-system.
 - All process was evaluated at atmospheric condition with no change in pressure condition. Thus, only chemical and thermal exergies were considered.
4. The thermodynamic calculation was conducted using a simulation through HSC 5.1 software. The output calculation are 1) heat and mass balance; 2) Enthalpy flowchart; and 3) Exergy flowchart of each process.

A comparison with an existing ironmaking system in case of a blast furnace was also made considering the boundary system limited to the sintering process, coke production, and blast furnace.

5.3. Result and Discussions

5.3.1. Exergy analysis of each process in the proposed ethanol-assisted ironmaking system

5.3.1.1. Goethite ore dehydration (Process 1)

Heat and material balance on process 1 is depicted in Figure 5.3.1. To produce 1000 kg-hot metal, 1419 kg FeOOH is required. Considering the presence of gangue materials like SiO₂ and Al₂O₃, goethite ore of 1741 kg is required as the raw material input in Process 1. Dehydration of FeOOH is an endothermic process with the reaction as follows:



The process becomes spontaneous at a temperature above 356 K, with $\Delta H_r = 54.49 \text{ kJ/mol}$. The simulation also shows that the heat required to supply the dehydration process is 0.813 GJ for 1741 kg of goethite ore at 573 K.

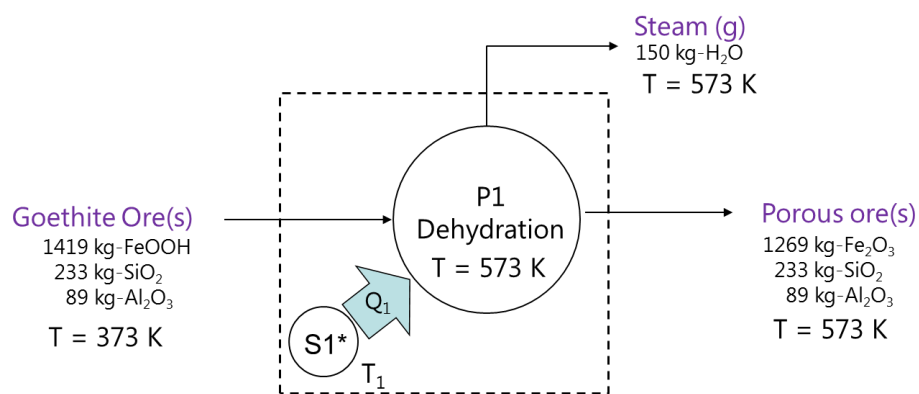


Figure 5.3.1 Heat and material balance on process 1.

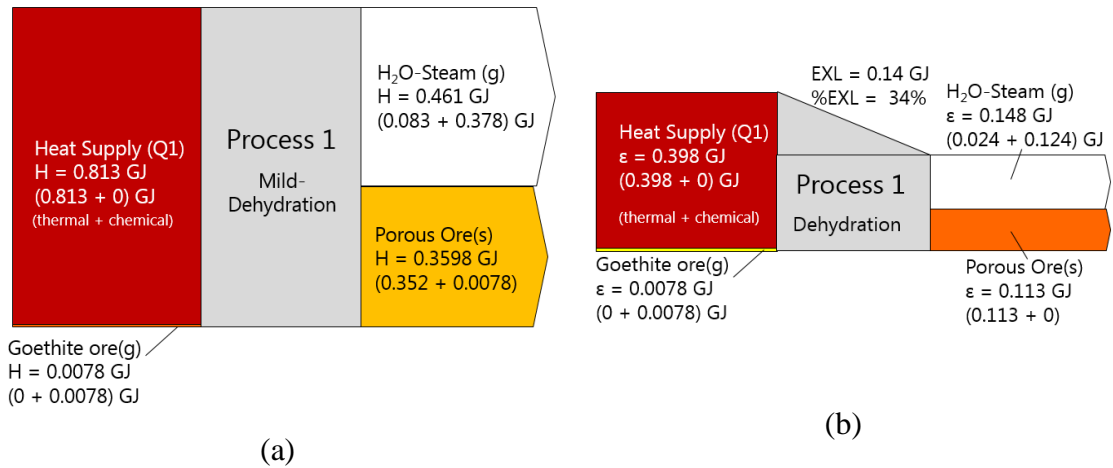


Figure 5.3.2 Enthalpy flow chart (a) and exergy flow chart (b) of the mild-dehydration process producing porous hematite ore from goethite ore.

Enthalpy flow on process 1 shows that the mild-dehydration of goethite ore need the heat supply (Q1) of 0.813 GJ per 1419 kg goethite ore. The heat supply (Q1) is consumed to overcome the endothermic heat for dehydrating the combined water in FeOOH, as well as the sensible heat for increasing the temperature from room temperature to 573 K. Exergy flow, shows if Q1 supplied as thermal heat at 573 K, it would have an exergy of 0.398 GJ per 1419 kg of goethite ore.

Table 5.3.1 shows the effect of temperatures on exergy loss (EXL) on ore dehydration process. In case of only providing the electricity as a heat source, exergy loss around 68% of exergy input. In contrast, providing the heat supply (Q1) instead of electricity, for instance like hot air at 873 K, the EXL drops to 52%. Interestingly, lowering the temperature of heat supply (Q1), the dehydration process will occur with 34% of EXL. It concluded that the dehydration process could be conducted more exergy efficiently at the lower temperature. The heat source at 573 K can be easily obtained by applying the low-temperature waste heat from other processes.

Table 5.3.1 Temperature selections for Q1 to minimize EXL

Case	Case 1	Case 2	Case 3	Case 4	Case 5
Heat Supply, Q1 [GJ]	0.813	0.813	0.813	0.813	0.813
Temp [K]	∞ (Electricity)	873	773	673	573
Exergy (Q1)	0.813	0.535	0.500	0.453	0.390
Exergy input [GJ]	0.821	0.543	0.507	0.461	0.398
Exergy output [GJ]	0.261	0.261	0.261	0.261	0.261
Exergy loss [GJ]	0.560	0.282	0.246	0.200	0.137
%EXL	68%	52%	49%	43%	34%

5.3.1.2. Ethanol-assisted reduction furnace (Process 2)

In this process, the porous ore of produced from process 1 is reduced by ethanol that is injected at 843 kg/ton hot metal in an ethanol-assisted reduction furnace. Ethanol is thermally decomposed to H₂, CO, and C that then reduce the iron ore and exhausting ER gas. Heat and mass balance of ore reduction process by ethanol is depicted in Figure 5.3.3. The ER gas composition was calculated as thermodynamic equilibrium by targeting the reduction degree in reduced ore of 81% at 1023 K.

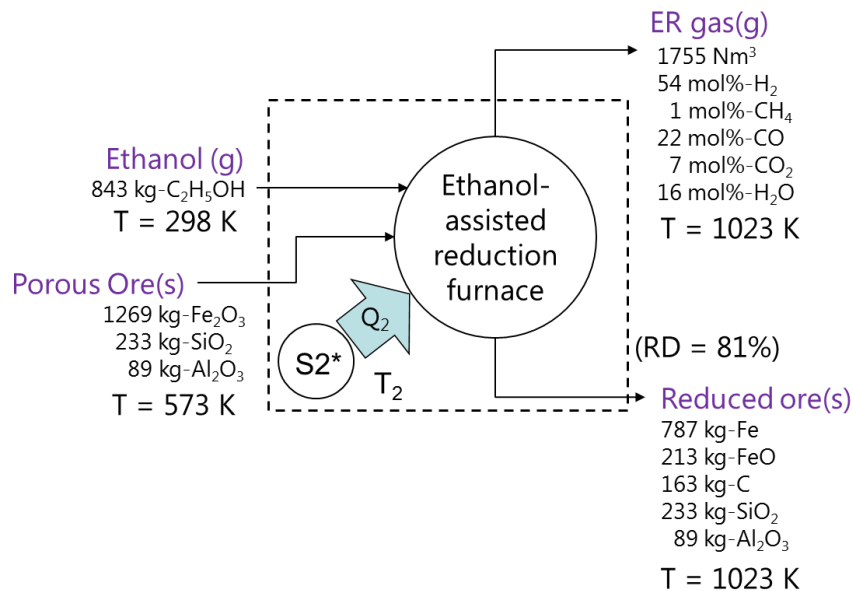


Figure 5.3.3 Mass and heat balance at the ethanol-assisted reduction furnace

The energy and exergy flowcharts of process 2 are shown in Figure 5.3.4. Ethanol has high enthalpy as well as exergy content contributes as a reducing agent for porous iron ore. However, an intermediate heat supply (Q_2) was still needed, calculated from heat balance to overcome the required heat for reducing Fe_2O_3 to Fe by ethanol as well as increasing temperature to 1023 K. The ER gas still contains a large enthalpy to be utilized due it still containing high amount of H_2 (54 mol%). The exergy of ER gas is also still high causing the exergy loss in process 2 is very low. Therefore, the decomposition of ethanol, which is producing a gas containing H_2 and CO, makes it become thermodynamically promising for ironmaking application in the exergy viewpoint.

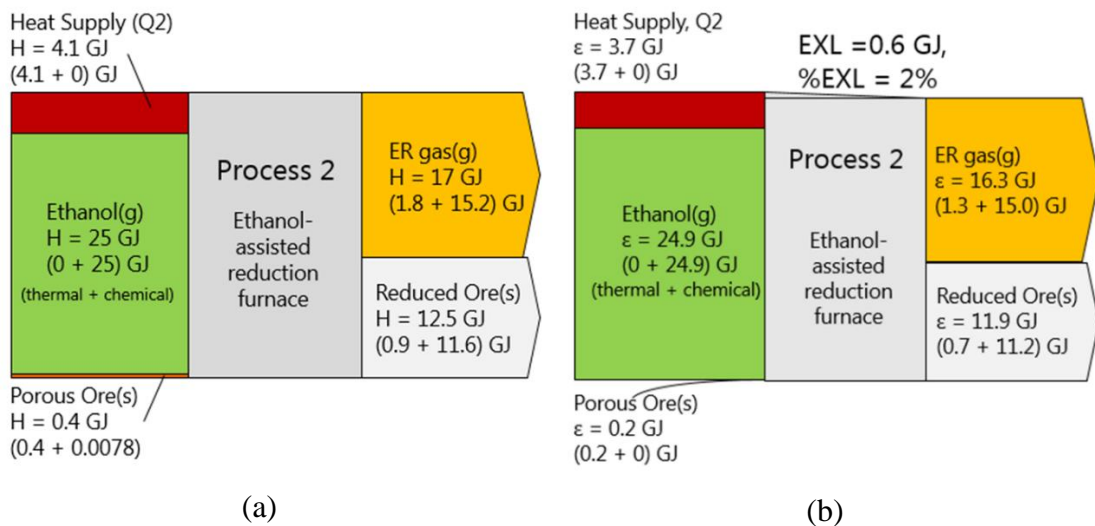


Figure 5.3.4 Enthalpy flowchart (a) and exergy flowchart (b) of the ethanol-assisted reduction (Process 2)

5.3.1.3. Melting and Separation of Hot Metal (Process 3)

Process 3, as is depicted in Figure 5.3.5, is designed for melting the reduced iron as hot metal as well as separating it from slag material. Hot metal - slag separation occurs at $T > 1809$ K, in this case, we assumed at 1833 K is sufficient to carry out the process. Since in process 2, the reduced ore only reaches the reduction degree of 81% and the carbon content of 14mass%. The reduction reaction will be continued in process 3 to

reach 99.9%, an assumption. However, additional fuel (i.e., coke) is still required as the heat source for melting. Required O_2 is calculated for coke combustion reaction: $C + O_{2(g)} \rightarrow CO_{2(g)}$. The oxygen is supplied stoichiometrically, in assumption, to avoid the excess oxygen re-oxidize the metallic iron in the hot metal.

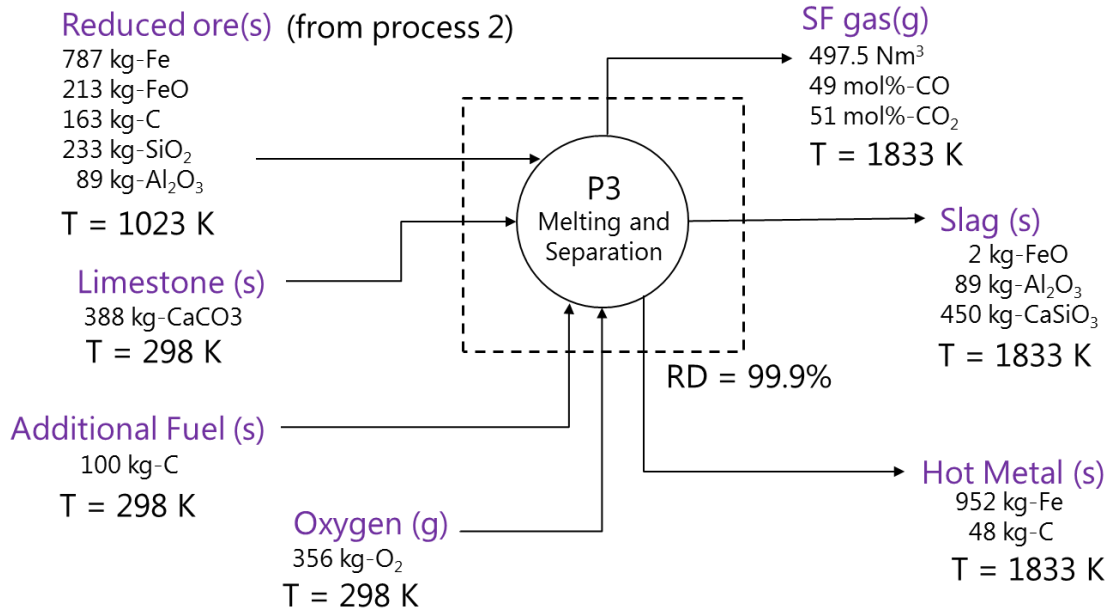


Figure 5.3.5 Heat and Mass balance of hot metal – slag separation (Process 3)

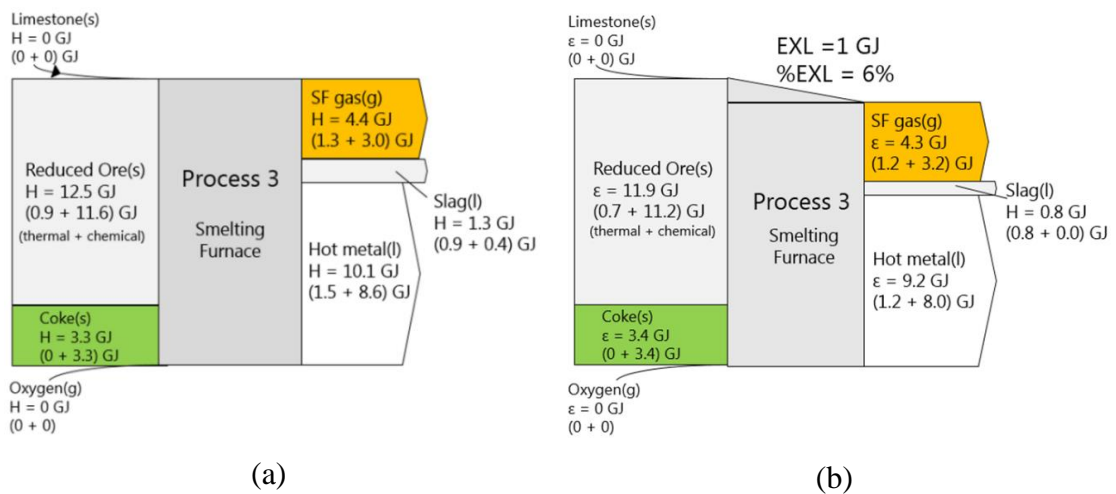


Figure 5.3.6 Enthalpy (a) and exergy (b) flow of hot metal – slag separation (Process 3)

5.3.1.4. Recovery ethanol from exhaust gas (Process 4)

Ethanol, conventionally, is produced from glucose fermentation by yeast, with CO₂ emitted as a by-product. This fermentation process is performed in the absence of oxygen, considering it as the anaerobic process [21]. Recently, Lanzatech technology offers breakthrough methods to produce ethanol from waste steel gas for transportation fuel purposed [20]. When gas fermentation is deployed in the steel mill, instead of sending a residual gas stream to a flare or power generation unit, it is cooled, cleaned and injected into a fermentation vessel containing proprietary microbes and liquid media. The microbes grow and increase their biomass by consuming CO/CO₂/H₂. As a byproduct of this growth, they make ethanol and chemicals that can be recovered from the fermentation broth, similar to the way that yeast make ethanol or other products[22]. Nevertheless, this process can be considered as one promising method to recover the ethanol for waste gas of the process 2, improving the ethanol fuel efficiency of the proposed ethanol-assisted ironmaking process.

The evaluation of ethanol recovery in this process 4 is based on the Lanzatech technology with a thermodynamic approach. Exhaust gas from process 2 (ER gas) is used as raw input for process 4. Process units involved are tail gas preconditioner and gas fermentation. The gas fermentation is performed in the room temperature. The simplification of the gas fermentation process to produce ethanol with by-product assumed as the mainly acetic acid can be evaluated as reaction below:



Heat and mass balance of recovery ethanol from SR gas is depicted in Figure 5.3.7. Ethanol of 354 kg can be recovered from SR gas of 1755 Nm³ that is generated

from 843 kg of ethanol supplied as fuel in the process 2. This process will emit 354 kg CO₂. However, this CO₂ emission will be counted as carbon neutral.

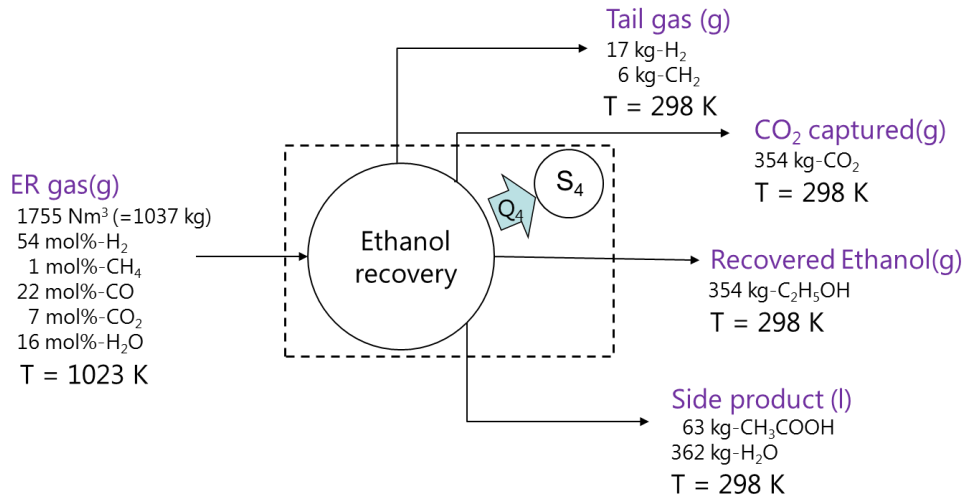


Figure 5.3.7 Heat and mass balance of ethanol recovery from ER gas.

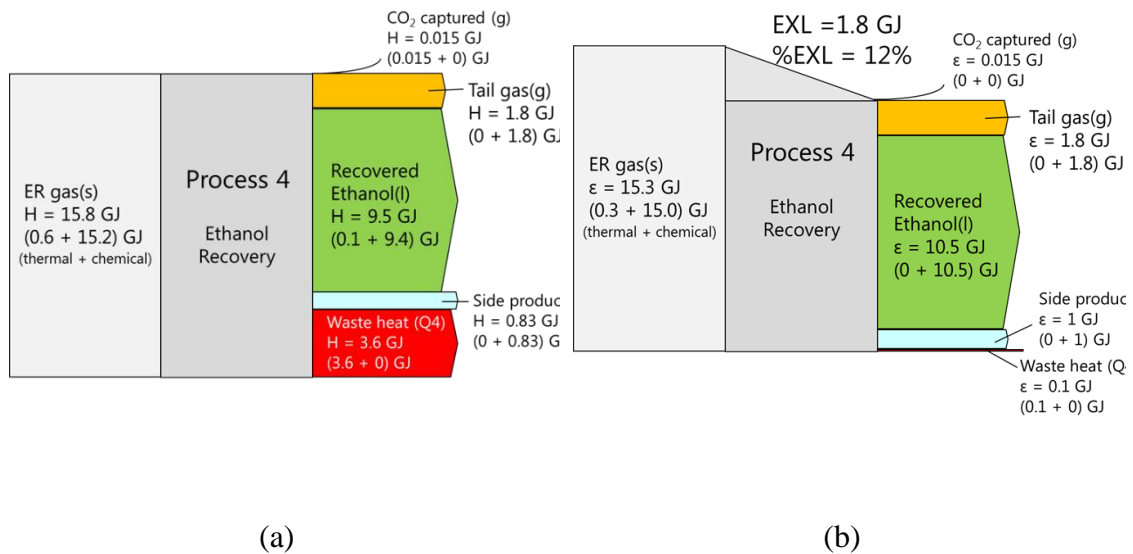


Figure 5.3.8 Enthalpy flow (a) and exergy flow (b) of ethanol recovery from ER gas.

5.3.2. Overall exergy evaluation on case 1 and 2

Figure 5.3.9 and 5.3.10 show the overall energy and exergy flow of the proposed ethanol-assisted ironmaking on case 1 (without ethanol recovery). The total inflowing energy of 33.2 GJ with 87% of it contributed for process 2 meaning the process 2 is the

most energy-intensive among the three processes. The inflowing energy in process 2 is dominated by ethanol as fuel. Nevertheless, the outflowing energy from process 2 also contributes 51% of the total overall outflowing energy.

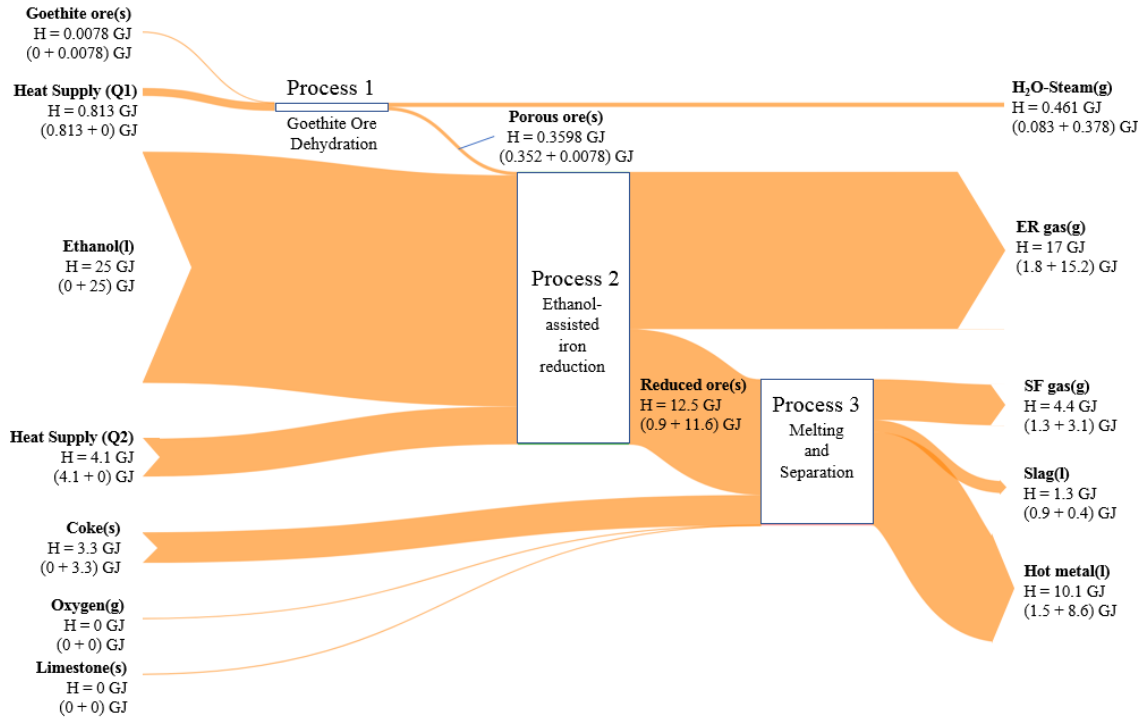


Figure 5.3.9 Overall enthalpy flow of ethanol-assisted ironmaking: case 1

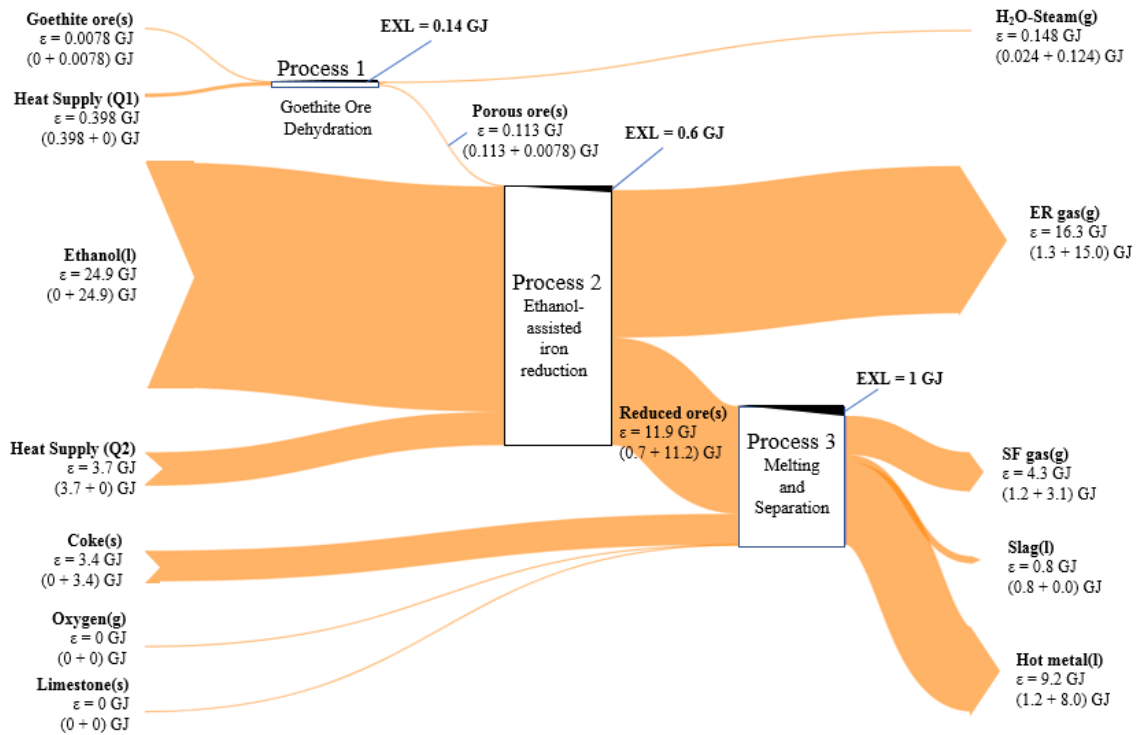


Figure 5.3.10 Overall exergy flow of ethanol-assisted ironmaking: case 1

Figure 5.3.11 and 5.3.12 describe the energy and exergy flow of ethanol-assisted ironmaking with ethanol recovery (case 2). In this case, ER gas in case 2 was treated in the ethanol recovery unit (process 4) to produce ethanol again. The recovered ethanol from ER gas is then recycled to process 2 to reduce the required amount of fresh ethanol. The sensible heat from ER gas was also utilized as heat supply (Q1) for the dehydration process (process 1). Meanwhile, SF gas from process 3 was utilized as heat supply (Q2) for ethanol-assisted reduction process (process 2). However, additional O₂ is needed to convert chemical energy to thermal energy through the combustion process.

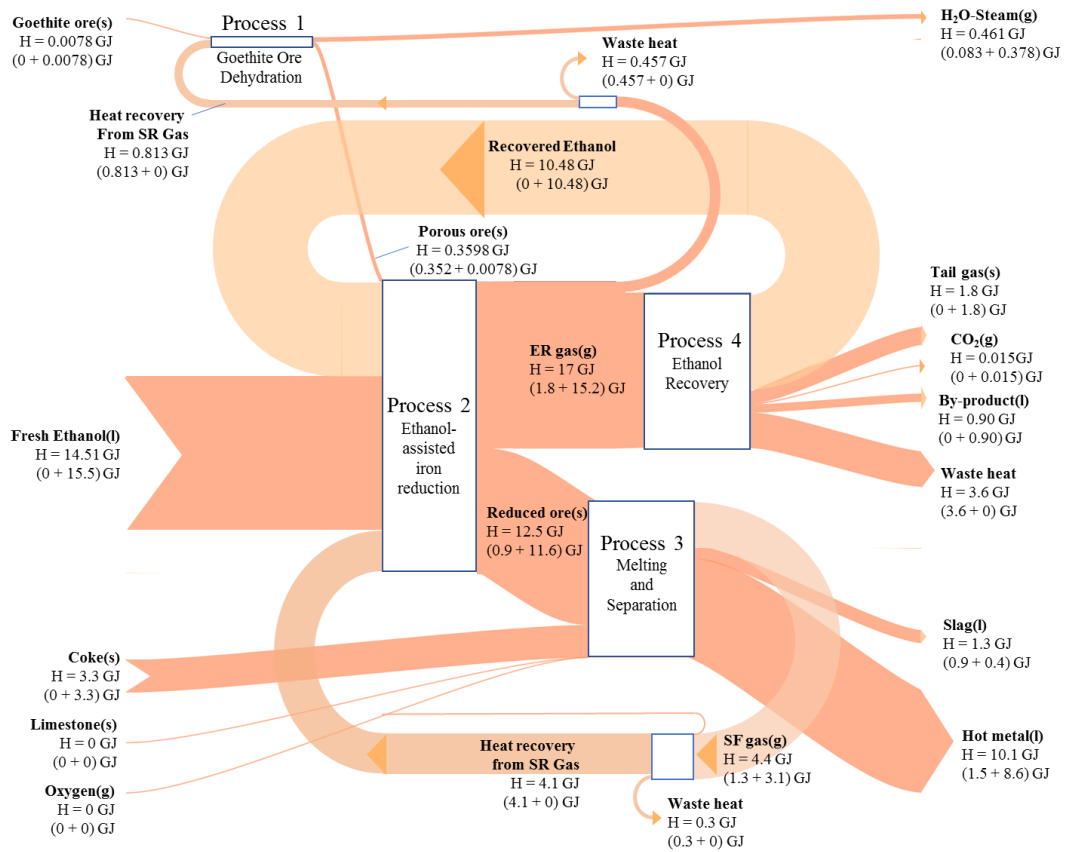


Figure 5.3.11 Overall enthalpy flow of ethanol-assisted ironmaking: case 2

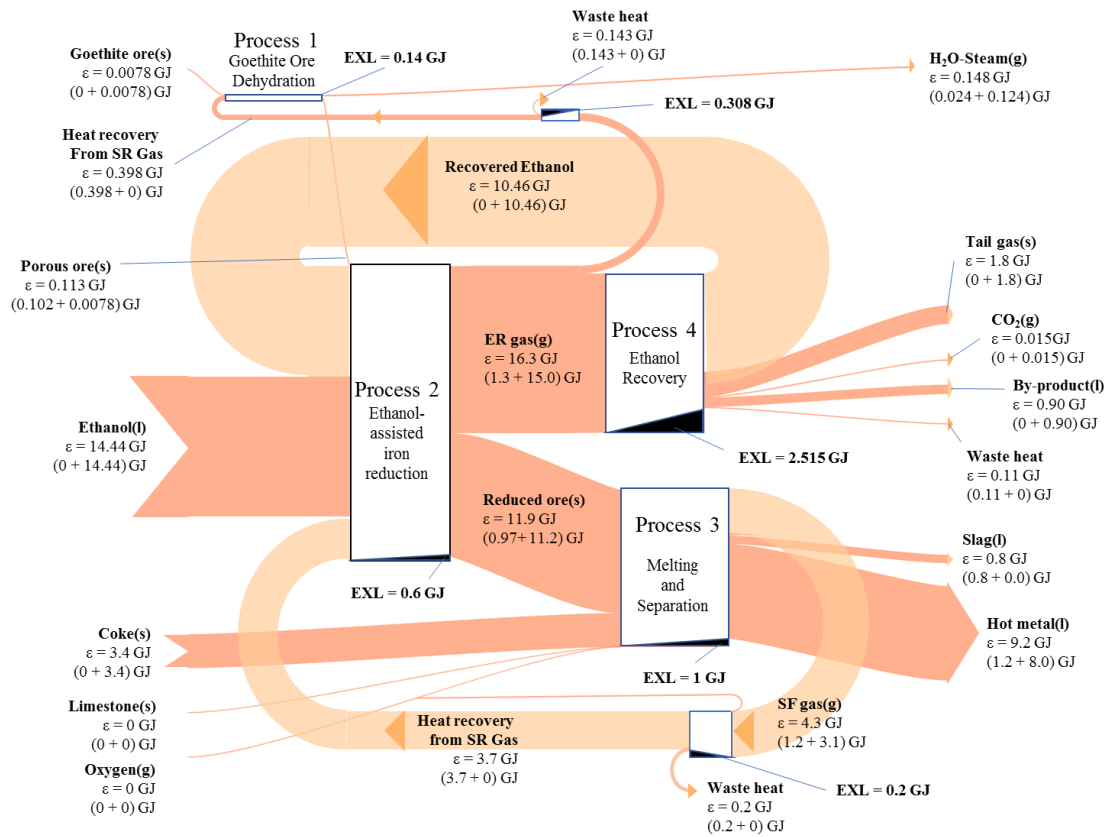


Figure 5.3.12 Overall exergy flow of ethanol-assisted ironmaking: case 2

Table 5.3.2 shows the comparative analysis of the proposed ethanol-assisted ironmaking versus conventional blast furnace operation. The aim of introducing an ethanol recovery in case 2 is to utilize the possible unused waste heat from case 1 such as ER gas and SF gas. ER gas containing much H₂ and CO is the most critical part that can be recovered as ethanol. The recovered ethanol then is recirculated back to reduce the fresh ethanol feed in Process 2. As applying the ethanol recovery system in ethanol assisted ironmaking (case 2), the exergy efficiency, in the term of the exergy of main product divided by the total exergy input, increase significantly to 52% from 29% of case 1. The significant increase in the exergy efficiency is due to the significant saving in the input ethanol exergy. Also, the significant increase in exergy efficiency was also obtained

in comparison with the conventional blast furnace using coke as a reducing agent (that of 38%), attributed to the simultaneous reduction by H₂, CO, and C-deposited from ethanol.

CO₂ emission in ethanol ironmaking would significantly lower than a blast furnace which is attributed from the hydrogen reduction process releasing water steam, counted as carbonless reduction. Also, CO₂ released from ethanol recovery can be counted as carbon-free, resulting in an additional benefit from an environmental aspect. As a comparison for producing 1 ton of hot metal, the ratio of carbon-free on CO₂ emission of ethanol ironmaking gives 73% and 70% from case 1 (no ethanol recovery) and case 2 (with ethanol recovery), respectively. The decrease in the carbon-free ratio in case 2 compared to case 1 is because of more combustion occurs in converting SF gas from process 3 as a recovered heat supply for process 2.

Table 5.3.2 Comparative analysis of ethanol-assisted ironmaking versus conventional blast furnace operation.

Parameter	Ethanol-assisted Ironmaking		Blast Furnace route*
	Case 1 (no recovery)	Case 2 (with heat and ethanol recovery)	
Fresh-Ethanol consumption [kg/t-HM]	843	489	-
Coke consumption [kg/t-HM]	100	100	450
O ₂ supply [kg/t-HM]	356	526	933
Intermediate Heat [GJ/t-HM]	Q1 = 0.8 Q2 = 4.1	-	-
Total Exergy in [GJ/t-HM]	32.82	17.84	22.37
Total Exergy out [GJ/t-HM] (Hot metal exergy [GJ/t-HM])	30.75 (9.2)	13.25 (9.2)	17.4 (8.6)
Exergy loss [GJ/t-HM]	2.07	4.76	4.96
Exergy efficiency [%] (= $\epsilon_{\text{hot metal}}/\Sigma\epsilon_{\text{in}} \times 100\%$)	29	52	38
CO ₂ emission [kg/t-HM]	537 (from ethanol) 200.7 (from coke)	837 (from ethanol) 362 (from coke)	1650 (from coke)
Ratio of carbon free emission [%]	73	70	0

*Parameters analysis on ironmaking of blast furnace route as in [23], excluding the coke oven operation.

Ethanol-assisted ironmaking using mild-dehydrated goethite ore is a novel process in ironmaking. This study already demonstrated the possibility of ethanol as a reducing agent for ironmaking on a laboratory scale and the thermodynamic system evaluation, given an interesting result. However, to ensure this idea become applicable in industrial scale, high effort would be needed to face the future challenges in ethanol-assisted ironmaking such as: to conduct scale-up experiments, to design the reactor for ethanol-assisted ironmaking in detail aspect, to apply an evaluation on rigorous system design, and to ensure the bioethanol security for ironmaking industry as well.

In my opinion, so far, the proper reactor for realizing the application of this idea is reduction shaft furnace like in MIDREX process. The MIDREX process typically uses natural gas as reductant and fuel using the reformer. It is possible to modify easily by substituting natural gas to ethanol. Fig. 5.3.13 shows the proposed process for ethanol-assisted ironmaking that equipped with the COREX's melting furnace and ethanol recovery of LANZATECH.

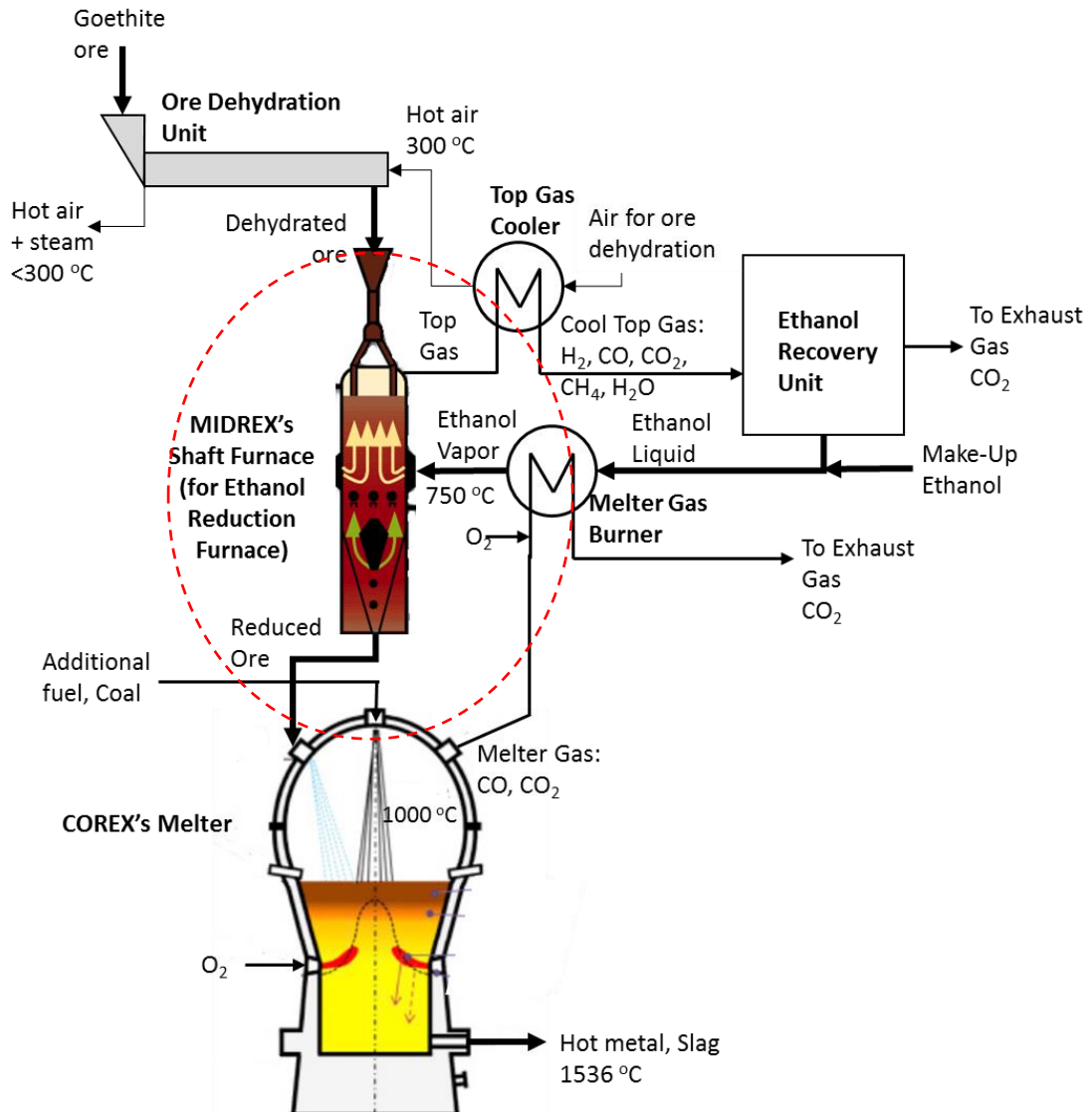


Figure 5.3.13 Proposed process for ethanol-assisted ironmaking using a shaft furnace like in MIDREX process combined with COREX's melting process and ethanol recovery of LANZATECH.

5.4. Conclusions

On a thermodynamic viewpoint, applying a high exergetic and renewable reducing agent like ethanol for ironmaking is attractive. The exergy analysis for the proposed process of ethanol-assisted ironmaking was successfully conducted with the conclusions:

1. There are four processes involved in ethanol-assisted ironmaking: (1) Ore mild-dehydration, (2) Porous ore reduction by ethanol, (3) Hot metal – slag separation, and (4) Ethanol recovery.
2. Upon enthalpy-exergy analysis, as the basis of 1000 kg-Fe (total product):
 - Process 1: Additional heat required for ore dehydration (Q_1) = 0.81 GJ with exergy efficiency=28%.
 - Process 2: Additional heat required for reduction by ethanol (Q_2) = 3.7 GJ with exergy efficiency= 42%
 - Process 3: Additional fuel (i.e., coke) is required to as heat source. Required O_2 is calculated as on reaction: $C + O_2(g) \rightarrow CO_2(g)$. In this case, the exergy efficiency= 60%
 - Process 4: 42% of ethanol can be recovered, with exergy efficiency=64%.
3. Overall evaluation: Benefits of bioethanol as a reducing agent for ironmaking are 52% of exergy efficiency and 70% of carbon-free emission
4. Future challenges are to apply a rigorous system design, to design the reactor/furnace for ethanol-assisted ironmaking, as well as to ensure the bioethanol security for ironmaking industry

References

- [1] World Steel Association, 2018, Fact Sheet, https://www.worldsteel.org/en/dam/jcr:f07b864c-908e-4229-9f92-669f1c3abf4c/fact_energy_2018_.pdf. accessed on November 21, 2018.
- [2] International Energy Agency, 2018, <https://www.iea.org/Sankey/index.html#c=World&s=Final%20consumption>

- [3] He, K. and Wang, L., 2017. A review of energy use and energy-efficient technologies for the iron and steel industry. *Renewable and Sustainable Energy Reviews*, 70, pp.1022-1039.
- [4] D. Paul, "Modeling the U.S. Iron and Steel Industry," U.S. Energy Information Administration Task Order DE-DT0001606, Subtask 1.2 (Leidos: November 15, 2013). in <https://www.eia.gov/outlooks/ieo/pdf/industrial.pdf>
- [5] World Steel Association. Crude steel statistics tables 2014, (<https://www.worldsteel.org>); 2015 (accessed 22.01.15)
- [6] Hanrot, F., Sert, D., Delinchant, J., Pietruck, R., Bürgler, T., Babich, A., Fernández López, M., Álvarez García, R. and Díez Díaz-Estébanez, M., 2009. CO₂ mitigation for steelmaking using charcoal and plastics wastes as reducing agents and secondary raw materials.
- [7] Brown T, Gambhir A, Florin N, Fennell P. Reducing CO₂ emissions from heavy industry: a review of technologies and considerations for policy makers. Grantham Institute for Climate Change, Briefing paper 7; 2012.
- [8] Kurniawan, A., Abe, K., Ohashi, K., Nomura, T. and Akiyama, T., 2018. Reduction of mild-dehydrated, low-grade iron ore by ethanol. *Fuel Processing Technology*, 178, pp.156-165.
- [9] Cahyono, R.B., Yasuda, N., Nomura, T. and Akiyama, T., 2015. Utilization of low grade iron ore (FeOOH) and biomass through integrated pyrolysis-tar decomposition (CVI Process) in ironmaking industry: Exergy analysis and its application. *ISIJ International*, 55(2), pp.428-435.
- [10] Miura, K., Miyabayashi, K., Kawanari, M. and Ashida, R., 2011. Enhancement of reduction rate of iron ore by utilizing low grade iron ore and brown coal derived carbonaceous materials. *ISIJ international*, 51(8), pp.1234-1239.
- [11] Saito, G., Nomura, T., Sakaguchi, N. and Akiyama, T., 2016. Optimization of the Dehydration Temperature of Goethite to Control Pore Morphology. *ISIJ International*, 56(9), pp.1598-1605.
- [12] Moran, M.J., 1982. *Availability analysis: a guide to efficient energy use*.
- [13] Akiyama, T. and Yagi, J.I., 1988. Exergy analysis of conventional ironmaking, direct reduction-electric furnace and smelting reduction systems. *Tetsu-to-Hagane*, 74(12), pp.2270-2277.
- [14] Rosen, M.A. and Dincer, I., 2001. Exergy as the confluence of energy, environment and sustainable development. *Exergy, an International journal*, 1(1), pp.3-13.
- [15] Szargut, J., Morris, D.R. and Steward, F.R., 1987. Exergy analysis of thermal, chemical, and metallurgical processes.

- [16] Brodyansky, V.M., Sorin, M.V. and Le Goff, P., 1994. The efficiency of industrial processes: exergy analysis and optimization (Vol. 9). Elsevier Science Limited.
- [17] Dincer, I. and Rosen, M.A., 1999. Energy, environment and sustainable development. *Applied energy*, 64(1-4), pp.427-440.
- [18] Dincer, I. and Cengel, Y.A., 2001. Energy, entropy and exergy concepts and their roles in thermal engineering. *Entropy*, 3(3), pp.116-149.
- [19] Hiraki, T. and Akiyama, T., 2009. Exergetic life cycle assessment of new waste aluminium treatment system with co-production of pressurized hydrogen and aluminium hydroxide. *International Journal of Hydrogen Energy*, 34(1), pp.153-161.
- [20] Ou, X., Zhang, X., Zhang, Q. and Zhang, X., 2013. Life-cycle analysis of energy use and greenhouse gas emissions of gas-to-liquid fuel pathway from steel mill off-gas in China by the LanzaTech process. *Frontiers in Energy*, 7(3), pp.263-270.
- [21] Cardona, C.A. and Sánchez, Ó.J., 2007. Fuel ethanol production: process design trends and integration opportunities. *Bioresource technology*, 98(12), pp.2415-2457.
- [22] Gaddy, J.L., Bioengineering Resources Inc, 2000. Biological production of ethanol from waste gases with *Clostridium ljungdahlii*. U.S. Patent 6,136,577.
- [23] Akiyama, T. and Yagi, J.I., 1988. Exergy analysis of conventional ironmaking, direct reduction-electric furnace and smelting reduction systems. *Tetsu-to-Hagane*, 74(12), pp.2270-2277.

CHAPTER VI

GENERAL CONCLUSIONS

Ironmaking industry faces serious problems related to the resources (depletion of high-grade ore), energy (high consumed energy) and environment (large emission of CO₂). The depletion of high-grade iron ore encourages us to utilize the low-grade ore (i.e., goethite) more effectively. In another hand, the shortage of coal, as well as the mitigation of high CO₂ emission, need more intensive utilization of an alternative carbon source. Bioethanol as derived from biomass, regarded as a renewable and carbon-neutral resource, is a promising candidate as a reducing agent for ironmaking. Introducing ethanol to reduce iron ore through the chemical vapor infiltration (CVI) process is attractive as aiming for low-temperature reduction. This study describes the process intensification of the previous proposed CVI process. The new process has been proposed named as ethanol-assisted ironmaking.

Chapter one describes the general introduction of this thesis.

Chapter two concludes several aspects to intensify in the previously proposed CVI ironmaking. As reported in the previous study, there are three processes involved in CVI ironmaking: (1) production of porous hematite ore, (2) production on carbon composite (CVI) ore through integrated pyrolysis-tar decomposition, and (3) reduction of the CVI ore. Production of nanoporous hematite from goethite is time-consuming due to the removal of combined water is slow under atmospheric air condition. Vacuum dehydration ($P = 1$ kPa) of goethite successfully removed the CW in 1 hour at 300 °C generating similar porous hematite with 2-4 nm pore-sized, surface area, and total pore

volume as found in the previous 24 h under atmospheric air condition. Vacuum dehydration is attractive to make it faster and suitable in an actual application. In addition, combining fuel like low-grade coal with woody biomass or waste plastic (i.e., polyethylene) utilizing the synergetic effect seems attractive to enhance overall pyrolysis efficiency. However, the deposited carbon content was not enough for the perfect reduction of iron ore.

Chapter three concludes that ethanol, a renewable source and considered carbon neutral when it is derived from biomass, is a promising candidate as a reducing agent for ironmaking. Ethanol is decomposed to H_2 , CO , and deposited C that then reduce the iron oxide. The reduction temperature of $750\text{ }^\circ\text{C}$ is significantly lower than that of the coke-iron oxide reaction in recent blast furnace operations, reaching an RD of 81%. A longer time of ethanol charging in the porous iron ore promotes a more significant reduction degree, and the compositions of the reducing gas (H_2 and CO) are sufficient for the reduction process. A significant reduction degree can be reached by ethanol decomposition with the porous ore from mild-dehydrating the high-CW ore. Porous iron ore acts as a suitable catalyst for ethanol decompositions as it simultaneously reduces to metallic iron. The higher CW in ore might provide the larger surface area in the iron ore, resulting in higher reactivity in the reduction process. The result of the proposed process intensification in the CVI ironmaking process reduces one step from the previous approach. Low-temperature iron reduction by ethanol may be attractive for future ironmaking processes.

Chapter four describes the kinetic analysis of simultaneous ethanol decomposition and iron reduction. The kinetic study is necessary for understanding the mechanism of the simultaneous ethanol decomposition – iron reduction process. There

were 8 main reactions involved: (1) decomposition of ethanol, (2) decomposition of methane, (3) steam reforming of methane, (4) water gas shift, (5) Boudouard reactions, (6) iron reduction by C, (7) iron oxide reduction by CO, and (8) iron reduction by H₂. Curve fitting methods were conducted with satisfying results ($R^2 > 0.90$) calculating 24 parameters consisting k_{froi} , E_{ai} , and C_{dj} . Interpretation on obtained parameters of C_{dj} shows that the reaction of gases inside pore might be inhibited by carbon deposition on the pore surface of iron ore.

Chapter five describes the exergy analysis and presents a feasibility study on the proposed ethanol-assisted ironmaking process. Applying a high exergetic and renewable reducing agent like ethanol for ironmaking would be attractive. There are four processes involved in the proposed ethanol-assisted ironmaking: (1) Goethite ore mild-dehydration, (2) Porous ore reduction by ethanol, (3) Hot metal – slag separation, and (4) Ethanol recovery. On the overall evaluation, the benefits of bioethanol as a reducing agent for ironmaking are 52% of exergy efficiency and 70% of carbon-free emission. This value is significant higher than the case of using coke as reducing agent as in the conventional blast furnace ironmaking. From the viewpoints above, ethanol-assisted ironmaking is an attractive method offering solution for problem-related resource, environment, and energy in future ironmaking industry.

APPENDIX

List of Publications

Ade Kurniawan

A. International Journals:

- 1) Ade Kurniawan, Keisuke Abe, Takahiro Nomura, and Tomohiro Akiyama. "Integrated Pyrolysis–Tar Decomposition over Low-Grade Iron Ore for Ironmaking Applications: Effects of Coal–Biomass Fuel Blending." *Energy & Fuels* 32 (2018): 396-405.
- 2) Ade Kurniawan, Keisuke Abe, Kouichi Ohashi, Takahiro Nomura, and Tomohiro Akiyama. "Reduction of mild-dehydrated, low-grade iron ore by ethanol." *Fuel Processing Technology* 178 (2018): 156-165.
- 3) Ade Kurniawan, Keisuke Abe, Takahiro Nomura, and Tomohiro Akiyama. "Integrated Pyrolysis-Tar Decomposition of Polyethylene-Coal Blends over Low-Grade Iron Ores" *Open Chemistry* (2018): (manuscript ID: OPENCHEM-D-18-00290). *Under review*
- 4) Keisuke Abe, Ade Kurniawan, Kouichi Ohashi, Takahiro Nomura, and Tomohiro Akiyama. "Ultrafast Iron-Making Method: Carbon Combustion Synthesis from Carbon-Infiltrated Goethite Ore." *ACS Omega* 3, no. 6 (2018): 6151-6157.
- 5) Keisuke Abe, Ade Kurniawan, Takahiro Nomura, and Tomohiro Akiyama. "Effects of reduction on the catalytic performance of limonite ore." *Journal of energy chemistry*, 27-5, (2017): 1489-1495.

B. International Conferences:

- 1) Ade Kurniawan, Keisuke Abe, Takahiro Nomura, Tomohiro Akiyama. Ethanol-Assisted Ironmaking of Mild-Dehydrated Goethite-Contained Ore. 10th Japan-Brazil Symposium on Dust Processing-Energy-Environment in Metallurgical Industries. Japan-Brazil Symposium – ISIJ International Session. Japan. Sendai, September 17-19, 2018
- 2) Ade Kurniawan, Keisuke Abe, Takahiro Nomura, Tomohiro Akiyama. Integrated Pyrolysis-Tar Decomposition of Polyethylene-Coal Blends over Low-Grade Iron Ores. International Conference on Chemistry, Chemical Process and Engineering (IC3PE). Indonesia, Yogyakarta, August 14-15, 2018.
- 3) Ade Kurniawan, Keisuke Abe, Kouichi Ohashi, Takahiro Nomura, Tomohiro Akiyama. "Glycerin-Ethanol Blending on Temperature Programmed Decomposition over Low-Grade Iron Ores", The 1st International Conference on Energy and Material Efficiency and CO₂ Reduction in the Steel Industry (EMECCR 2017), JAPAN, Kobe, International Conference Center, October 11-13, 2017.

C. Domestic Conferences:

- 1) Ade Kurniawan, Keisuke Abe, Takahiro Nomura, Tomohiro Akiyama. Vacuum dehydration of goethite-based ore for faster nanoporous ore production. The 176th Iron and Steel Institute of Japan (ISIJ) Meeting. Tohoku University. 2018.3.19-21 (Student Poster Session)
- 2) Ade Kurniawan, Keisuke Abe, Kouichi Ohashi, Takahiro Nomura, Tomohiro Akiyama. Polyethylene-Coal Blend Decomposition via Integrated Pyrolysis-Tar Decomposition over Low-Grade Iron Ores. The 175th Iron and Steel Institute of

Japan (ISIJ) Meeting. Chiba Institute of Technology, 2018.3.19-21 (Student Poster Session)

- 3) Ade Kurniawan, Keisuke Abe, Kouichi Ohashi, Takahiro Nomura, Tomohiro Akiyama. Effect of Steam Addition on Integrated Polyethylene-Coal Pyrolysis-Tar Decomposition over Goethite Ore. The 174th Iron and Steel Institute of Japan (ISIJ) Meeting. Hokkaido University, 2017.9.7. (Oral presentation)
- 4) Ade Kurniawan, Keisuke Abe, Takahiro Nomura, Tomohiro Akiyama. Synergetic effects of coal-biomass fuel blending on integrated pyrolysis-tar decomposition over goethite ore for ironmaking applications. The 172nd Iron and Steel Institute of Japan (ISIJ) Meeting. Osaka University. 2016.9.21-22 (Student Poster Session)

D. Awards:

- 1) *Effort Award*: Ade Kurniawan, Keisuke Abe, Kouichi Ohashi, Takahiro Nomura, Tomohiro Akiyama. Polyethylene-Coal Blend Decomposition via Integrated Pyrolysis-Tar Decomposition over Low-Grade Iron Ores. The 175th Iron and Steel Institute of Japan (ISIJ) Meeting. Chiba Institute of Technology, 2018.3.19-21 (Student Poster Session)
- 2) *Second Best Poster Award*: Ade Kurniawan, Keisuke Abe, Takahiro Nomura, Tomohiro Akiyama. Synergetic effects of coal-biomass fuel blending on integrated pyrolysis-tar decomposition over goethite ore for ironmaking applications. The 172nd Iron and Steel Institute of Japan (ISIJ) Meeting. Osaka University. 2016.9.21-22 (Student Poster Session)

ACKNOWLEDGMENTS

This research had been carried out under the supervision of Prof. Tomohiro Akiyama, Head of Energy Media Laboratory, Center for Advanced Research of Energy and Materials, Faculty of Engineering, Hokkaido University. I am profoundly indebted to him for all guidance and positive encouragements during this research. I really appreciate that he has always provided great opportunities for me to make a contribution to professional progress.

I also would like to express my sincere thanks and gratitude towards committee, Prof. Naoyuki Hashimoto and Prof. Seiichi Watanabe, Associate Prof. Yoshiaki Kashiwaya, and Associate Prof. Takahiro Nomura who reviewed this doctoral thesis, for their valuable comments and helpful advice.

I appreciate Gadjah Mada University (UGM) as my sending institution and ASEAN University Network (AUN) - JICA for providing the chance and scholarship for my study at Hokkaido University, Japan.

I am very grateful to my co-researchers: Dr. Keisuke Abe, Dr. Genki Saito, Mr. Kouichi Ohashi, and Mr. Masafumi Sanada. I would never have carried out all this study without their kind help and valuable discussion supported behind this study. I take this privilege to thank all members in the laboratory for kind help and encouragement. Special thank to Ms. Chiba for the administrative help and support during my study.

Finally, I would like to express my sincere thanks to my wife, Inaratul Rizkhy Hanifah and beloved sons, Danesh Idris Kurniawan, and Naoki Isa Kurniawan as well as members of my family who have always provided spiritual support to me.